



# **FIFI-LS**

## Handbook for Archive Users



J. Chu, D. Fadda, C. Fischer

Rev. 1.0

Date: 2023 Sep 28



# FIFI-LS Handbook for Archive Users

## Table of Contents

<b>1.</b>	<b>ESSENTIAL INFORMATION .....</b>	<b>1</b>
<b>2.</b>	<b>INSTRUMENT DESCRIPTION.....</b>	<b>4</b>
2.1	FIFI-LS OVERVIEW .....	4
2.2	INTEGRAL FIELD CONCEPT .....	4
2.3	INSTRUMENT DESIGN .....	5
2.3.1	<i>Dichroic Selection</i> .....	7
2.3.2	<i>Beam Rotator (K-Mirror)</i> .....	7
2.3.3	<i>Internal Calibrator</i> .....	8
2.4	OBSERVING MODES.....	9
2.4.1	<i>Symmetric Chop and Nod</i> .....	9
2.4.2	<i>Asymmetric Chop and Nod</i> .....	11
2.4.3	<i>Total Power</i> .....	11
2.4.4	<i>On-the-Fly Mapping</i> .....	11
2.4.5	<i>Raster Mapping</i> .....	12
2.4.6	<i>Spectral Dithering</i> .....	13
<b>3.</b>	<b>INSTRUMENT PERFORMANCE .....</b>	<b>14</b>
3.1	LINEARITY .....	14
3.2	LINE PROFILE AND SPECTRAL RESOLUTION.....	16
3.3	SPATIAL RESOLUTION .....	20
3.4	WAVELENGTH CALIBRATION AND ACCURACY .....	21
3.1	FLAT FIELDS .....	21
3.2	ABSOLUTE FLUX CALIBRATION .....	26
3.3	CROSS-CORRELATION OF PACS AND FIFI-LS FLUXES .....	30
3.4	SENSITIVITY .....	35
3.5	COMPARISON WITH PACS SPECTROSCOPY .....	38
3.5.1	<i>FIFI-LS and PACS Observation Modes</i> .....	38
3.5.2	<i>Flux Fraction in the Central Spaxel</i> .....	39
<b>4.</b>	<b>DATA .....</b>	<b>41</b>
4.1	PIPELINE SOFTWARE .....	41
4.1.1	<i>External Requirements</i> .....	41
4.1.2	<i>Source Code Installation</i> .....	41
4.1.3	<i>Configuration</i> .....	42
4.2	INPUT DATA .....	42
4.2.1	<i>Auxiliary Files</i> .....	43
4.3	DATA FORMAT.....	43
4.4	REDUCTION PROCEDURE.....	44
4.4.1	<i>Split Grating Chop</i> .....	44
4.4.2	<i>Fit Ramps</i> .....	48
4.4.3	<i>Subtract Chops</i> .....	49
4.4.4	<i>Combine Nods</i> .....	49
4.4.5	<i>Wavelength Calibration</i> .....	50
4.4.6	<i>Spatial Calibrate</i> .....	53
4.4.7	<i>Apply Flat</i> .....	54

4.4.8	<i>Combine Grating Scans</i> .....	55
4.4.9	<i>Telluric Correction</i> .....	56
4.4.10	<i>Flux Calibrate</i> .....	57
4.4.11	<i>Correct Wave Shift</i> .....	59
4.4.12	<i>Resample</i> .....	59
4.4.12.1	<i>Grid Size</i> .....	60
4.4.12.2	<i>Algorithm</i> .....	62
4.4.12.3	<i>Uncorrected Flux Cube</i> .....	62
4.4.12.4	<i>Detector Coordinates</i> .....	62
4.4.12.5	<i>Additional Scan Processing</i> .....	63
4.4.12.6	<i>Output Data</i> .....	63
4.5	<b>AUTOMATIC REDUCTION</b> .....	65
4.6	<b>MANUAL REDUCTION</b> .....	66
4.6.1	<i>Basic Workflow</i> .....	66
4.6.2	<i>Display Features</i> .....	69
4.6.3	<i>Descriptions of Key Parameters</i> .....	72
4.6.4	<i>Data Quality Assessment</i> .....	77
4.7	<b>PRODUCTS</b> .....	78
4.7.1	<i>Grouping LEVEL_1 Files for Processing</i> .....	78
4.7.2	<i>Pipeline Files</i> .....	79
4.8	<b>TELLURIC CORRECTIONS</b> .....	81
4.9	<b>ARTIFACTS</b> .....	87
4.9.1	<i>Vignetting</i> .....	87
4.9.2	<i>Telluric Line Residuals</i> .....	87
4.9.3	<i>Optical Ghosts</i> .....	87
4.9.4	<i>Corrupted Scan Files</i> .....	88
4.10	<b>SPECIAL CASES</b> .....	88
<b>5.</b>	<b>SCIENTIFIC RESULTS</b> .....	<b>89</b>
5.1	<b>THE STRUCTURE OF A PDR: M17-SW</b> .....	<b>89</b>
5.2	<b>A COMPLETE VELOCITY RESOLVED 3-D [CII] MAP OF THE M51 GRAND-DESIGN SPIRAL GALAXY</b> .....	<b>91</b>
5.3	<b>CHARTING C+ IN A MILKY WAY ANALOG: NGC 7331</b> .....	<b>92</b>
<b>6.</b>	<b>REFERENCES</b> .....	<b>94</b>
	<b>APPENDIX</b> .....	<b>95</b>
A.	<b>FIFI-LS FLIGHTS</b> .....	<b>95</b>
B.	<b>ANALYSIS TOOLS IN PYTHON: SOSPEX</b> .....	<b>101</b>
C.	<b>ANALYSIS TOOLS IN IDL: FLUXER</b> .....	<b>101</b>
D.	<b>FIFI-LS REDUX</b> .....	<b>101</b>



## 1. ESSENTIAL INFORMATION

**Table 1: General Information**

<b>Instrument wavelength total range</b>	50 $\mu$ m < $\lambda$ < 203 $\mu$ m
<b>Red array</b>	115-203 $\mu$ m
<b>Blue array</b>	50-125 $\mu$ m
<b>Array manufacturer</b>	MPE Munich
<b>Pixel size</b>	6" (Blue), 12" (Red)
<b>Array size</b>	5 $\times$ 5 pixels
<b>Field of view</b>	0.5' $\times$ 0.5' (Blue) and 1' $\times$ 1' (Red)
<b>Observing modes</b>	Chop/nod (symmetric and asymmetric), Total power, On-the-fly
<b>Years in service</b>	2014 to 2022
<b>P.I.</b>	A. Poglitsch, A. Krabbe
<b>Built by</b>	MPE Munich, IRS Stuttgart

**Table 1: Typical Lines Observed by FIFI-LS**

Line	Rest wav	Array	Spat FWHM	Central pixel	R	Spec FWHM	Inst cov	
Name	[ $\mu$ m]	Order	[arcsec]	flux fraction		[km/s]	[km/s]	[ $\mu$ m]
[OIII]	51.8145	B2	6.6	51%	792	378	1838	0.32
[NIII]	57.3170	B2	6.7	47%	1004	299	1526	0.29
[OI]	63.1837	B2	7.4	43%	1326	226	1242	0.26
[OIII]	88.3560	B1	8.6	35%	621	482	2341	0.69
[NII]	121.8976	B1	11.8	20%	1016	295	1351	0.55
[NII]	121.8976	R	11.8	59%	808	371	2343	0.95
[OI]	145.5254	R	14.1	47%	1071	280	1797	0.87
[CII]	157.7409	R	15.3	42%	1207	248	1561	0.82

*The array red or blue (R, B) and the order used to observe them is shown. Spatial and spectral resolution (R, and FWHM in km/s) and instantaneous coverage of the spectral array (in km/s and  $\mu$ m) is reported for each wavelength.*

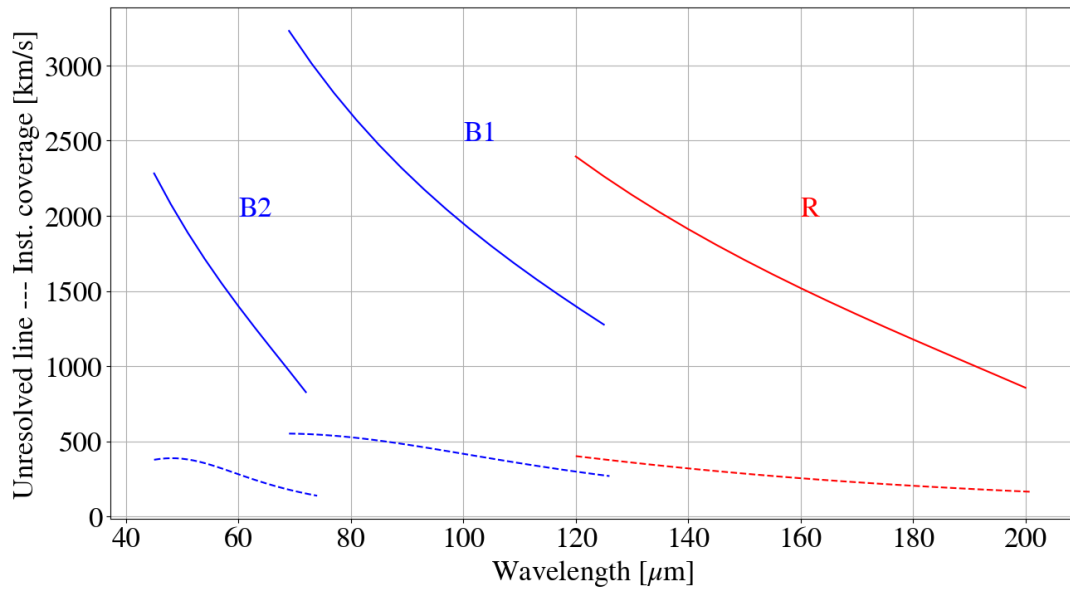


**Figure 1** Instantaneous coverage (solid lines) and width of the unresolved line (dashed lines) for the three possible combinations of array/order of FIFI-LS: R, B1, and B2.

**Table 2: A List of Far-IR Lines Accessible with FIFI-LS**

Line	$\lambda$ [ $\mu\text{m}$ ]	R	Line	$\lambda$ [ $\mu\text{m}$ ]	R
[O III]	51.8	970	CO	96.8	700
OH	55.9	1050	CO 25-24	104.4	780
[N III]	57.3	1090	CO 22-21	118.6	990
[O I]	63.2	1350	[N II]	121.9	770
C <sub>2</sub> H <sub>2</sub>	68.6	1710	CO 21-20	124.2	790
CO 38-37	69.1	1750	CO 20-19	130.4	840
C <sub>2</sub> H <sub>2</sub>	69.7	1790	[O I]	145.5	1000
CO 37-36	70.9	550	CO <sub>2</sub> (ice)	146.0	1010
CO 34-33	77.1	570	CO 17-16	153.3	1100
CH <sub>4</sub>	80.1	580	[C II]	157.7	1150
CO 31-30	84.4	600	CO 16-15	162.8	1220
OH	84.5	600	OH	164.3	1240
CO <sub>2</sub> (ice)	86.0	610	HCN	169.4	1310
CO 30-29	87.2	620	CO 15-14	174.0	1380
CH <sub>4</sub>	87.3	620	CO 14-13	186.0	1570
[O III]	88.3	620	CO 13-12	200.3	1820
OH	96.3	690			

**Table 3: Overview of FIFI-LS Flight Series\***

Flight Series	Flight Numbers	Deployment Location	Start Date	End Date
OC2C	F160 ~ F164	Palmdale, CA	04/17/2014	04/26/2014
OC3B	F199 ~ F206	Palmdale, CA	03/12/2015	03/27/2015
OC3K	F246 ~ F253	Palmdale, CA	10/14/2015	10/29/2015
OC4B	F280 ~ F287	Palmdale, CA	02/25/2016	03/10/2016
OC4F	F310 ~ F317	Christchurch, NZ	06/28/2016	07/06/2016
OC5B	F378 ~ F385	Palmdale, CA	02/25/2017	03/09/2017
OC5I	F422 ~ F424	Christchurch, NZ	07/26/2017	07/28/2017
OC6M	F524 ~ F527	Palmdale, CA	11/06/2018	11/09/2018
OC6U	F548 ~ F551	Palmdale, CA	02/27/2019	03/02/2019
OC7A	F562 ~ F573	Palmdale, CA	05/01/2019	05/17/2019
OC7H	F635 ~ F640	Palmdale, CA	10/30/2019	11/14/2019
OC7L	F662 ~ F665	Palmdale, CA	02/25/2020	02/28/2020
OC8B	F676 ~ F682	Palmdale, CA	08/18/2020	09/04/2020
OC8J	F716 ~ F723	Palmdale, CA	04/13/2021	04/23/2021
OC8M	F737 ~ F742	Palmdale, CA	05/25/2021	06/05/2021
OC9I	F803 ~ F813	Palmdale, CA	12/22/2021	01/21/2022
OC9L	F839 ~ F840	Palmdale, CA	03/15/2022	03/16/2022
OC9M	F842 ~ F848	Santiago, Chile	03/22/2022	03/30/2022
OC9T	F905 ~ F909	Palmdale, CA	08/24/2022	09/01/2022

\* See also [Table 15](#) in Appendix for list of all individual FIFI-LS flights.

**2. INSTRUMENT DESCRIPTION**

**2.1 FIFI-LS OVERVIEW**

The Far Infrared Field-Imaging Line Spectrometer (FIFI-LS) was an integral field, far infrared spectrometer. The instrument included two independent, simultaneously operating grating spectrometers sharing one common field-of-view (FOV). Each spectrometer had a detector consisting of 400 pixels of Germanium Gallium-doped photoconductors. The short wavelength spectrometer (blue channel) operated at wavelengths between 51  $\mu\text{m}$  and 125  $\mu\text{m}$ , while the long wavelength spectrometer (red channel) covered the range from 115  $\mu\text{m}$  up to 200  $\mu\text{m}$ . One of the two dichroics had to be selected for an observation affecting the wavelength range of both channels in the overlap region.

The projection onto the sky of the 5 $\times$ 5 pixel FOVs of both channels was concentric with an offset in the blue array by 10 arcsec. The red channel had an average pixel size of 12 $\times$ 12 arcsec yielding an instantaneous 1 arcmin square FOV, and the blue channel had a pixel size of 6 $\times$ 6 arcsec and a 30 arcsec square FOV. The resolving power of both channels varied between 500 and 2000 depending on the observed wavelength. Spatial and spectral dithering were employed in most observations to extend coverage beyond the instrument’s instantaneous coverage.

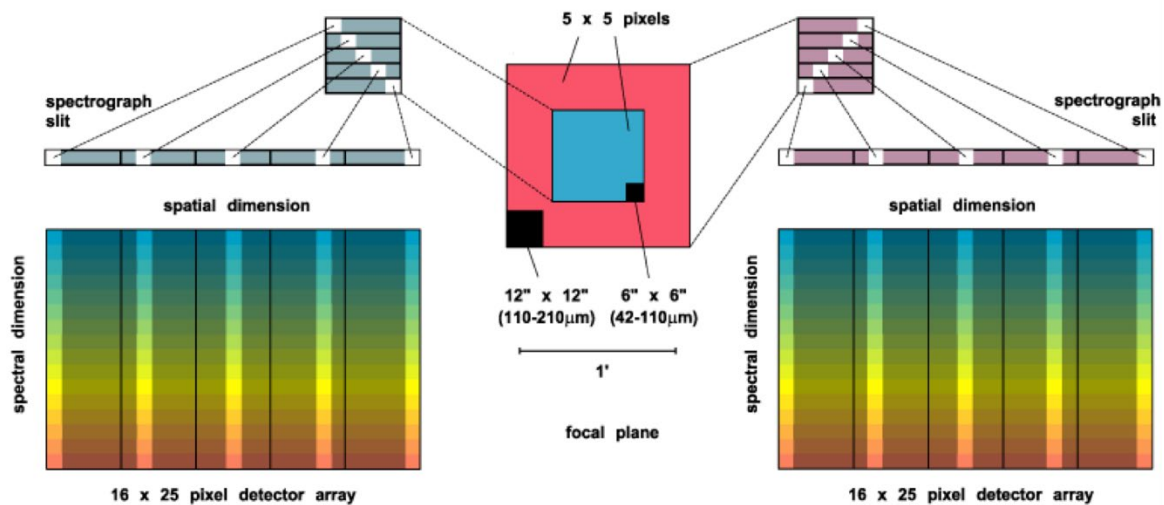


*Figure 2 Illustration of the field imaging concept in FIFI-LS. The optics sliced the rows of the 5 $\times$ 5 pixel field of view into a 25 $\times$ 1 pixel pseudo slit.*

**2.2 INTEGRAL FIELD CONCEPT**

The integral field unit (IFU) allowed FIFI-LS to obtain spectra at each point in its FOV; this contrasts with a spectrometer with a slit, which only provides spectra along the slit. Both channels in FIFI-LS had an IFU, which consisted of 15 specialized mirrors to separate the two-dimensional 5 $\times$ 5 pixel FOV into five slices (of five pixels length each) which were then reorganized along a (one dimensional) line (25 $\times$ 1 pixel). This line formed the entrance slit of the actual spectrometer. The diffraction grating dispersed the incoming light in the spectral dimension. Finally, the dispersed light reached the 25 $\times$ 16 pixel detector array. The result was a data cube with 5 $\times$ 5 spatial

pixels (spaxels) and 16 spectral pixels in the spectral dimension. One spaxel contained a spectrum for a particular pixel on the sky. [Figure 2](#) shows the concept.

### 2.3 INSTRUMENT DESIGN

A photo of the instrument installed on the SOFIA telescope and a diagram of the cryostat installed at the telescope flange are provided in [Figure 3](#). The cryostat (gray) sat on top of a cradle (also gray). A pressure coupler (orange) operated as a pressure barrier for the aircraft cabin since stratospheric pressure prevailed inside the telescope tube during flight. The instrument operated at four temperature levels: The boresight box housed the warm dichroic at room temperature and stratospheric pressure. Inside the vacuum vessel there were three temperature levels: Nitrogen (red), Helium (blue), and superfluid Helium (magenta), kept cool with three cryogen tanks.

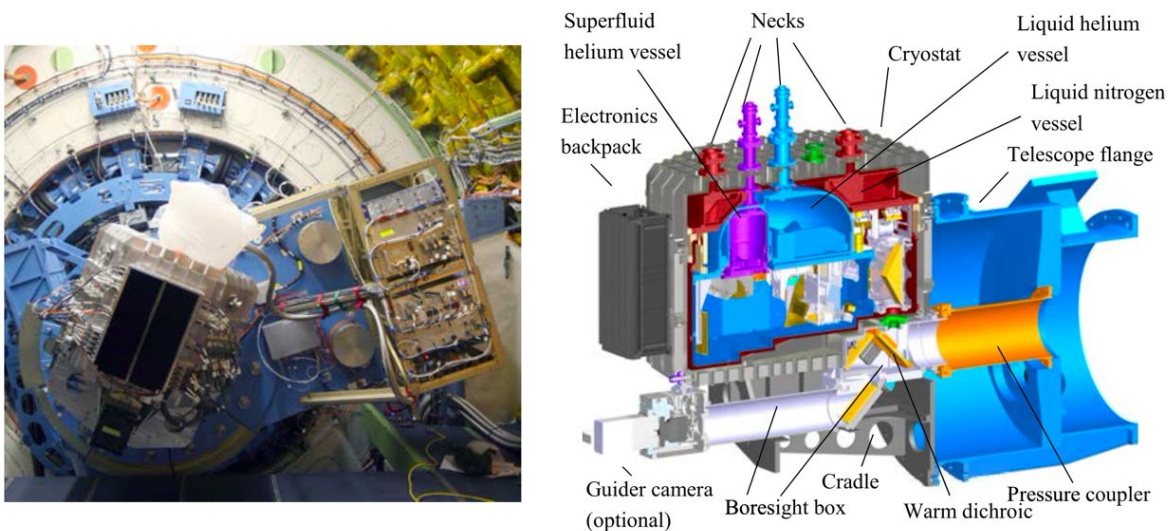


**Figure 3** (Left) *FIFI-LS and its counterweight rack (CWR) installed at the SOFIA telescope. The telescope is at the lower end of its 20–60 elevation range. (Right) A drawing of FIFI-LS with some main components labeled.*

A schematic overview of the complete optical path of FIFI-LS is presented in [Figure 4](#). A detailed overview of the optical design of the instrument is available in [Looney et al. \(2003\)](#) and [Raab et al. \(2003\)](#). The light coming from the telescope through the Nasmyth tube was reflected into the FIFI-LS cryostat at the “warm dichroic” which has always been a fully reflective mirror. The incoming light was then transmitted through the entrance window that formed the pressure boundary of the cryostat. A K-mirror rotated the sky footprint to optimize coverage for sources and keep the field orientation fixed on the detectors (see Section 2.3.2). More details are found in [Colditz et al. \(2014\)](#). A flip mirror switched the optical path between the sky and a calibration source used to generate spectral and spatial flat fields.

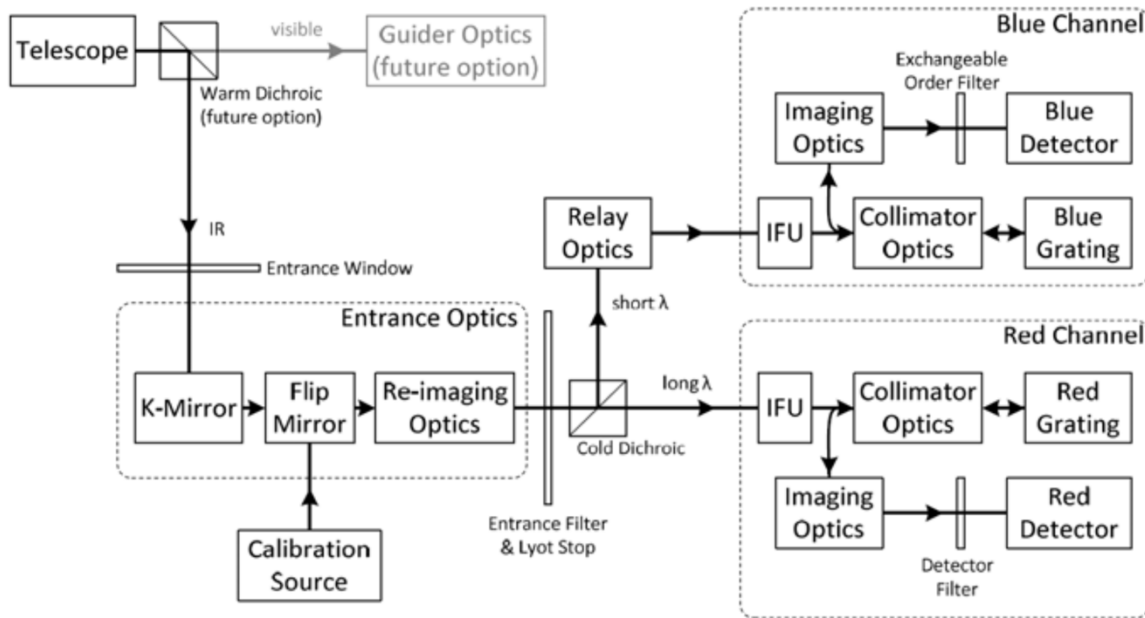


**Figure 4** Schematic of the FIFI-LS optical path from the telescope to the detectors of both channels (Fischer et al. 2018)

The light entered the helium cooled optical plate through the Lyot stop and the entrance filter assembly, which had a short wavelength cutoff at  $40\ \mu\text{m}$ . Past the entrance filter the light was split up into the blue and red channels by the cold dichroic, which transmitted the longer wavelength for the red channel and reflected the light for the blue channel. Since the transition between transmission and reflection was not a perfect step function at a single wavelength but extended over several microns, two interchangeable dichroics were available to keep full wavelength coverage in both channels (see Section 2.3.1). The dichroics also provided some flexibility in the channel in which a specific wavelength was to be observed. For example, the CO line at  $119\ \mu\text{m}$  could be observed in either the blue or the red channel. The integral field units (IFU) rearranged the  $5\times 5$  spaxel FOV into the 25 spaxel pseudo-slit that was projected onto the diffraction gratings via the collimator optics. The instantaneous wavelength range covered by the detector was set by rotating the grating, defined in “inductosyn” units (see Section 3.4). More details on the grating systems can be found in Rebell et al. (2014) and Rebell (2016). The beam returned through the collimator optics a second time on its way to the detectors. In the blue channel observations could be performed in both first and second order via an inflight interchangeable order-sorting filter located before the light entered the blue detector assembly.

The detector assembly was cooled by helium pumped down to about 20 mbar to operate at a temperature of about 1.8 K. FIFI-LS used gallium-doped germanium pixels in both channels. The spectral sensitivity of gallium-doped germanium pixels is high between  $40\text{-}120\ \mu\text{m}$ , ideal for the blue channel. For the red channel, the detector elements were stressed in their mounting structures to shift their spectral sensitivity into the  $120\text{-}210\ \mu\text{m}$  range (Rosenthal et al. 2000). The pixels in the blue channel had a size of approximately  $6\times 6$  arcsec on the sky while the red channel had a



projected size of  $12 \times 12$  arcsec. These plate scales were chosen to roughly match the diffraction-limited point spread functions at the mean wavelengths of the two channels.

### 2.3.1 Dichroic Selection

One of the main advantages of FIFI-LS was its uninterrupted coverage of two wavelength ranges between  $51\text{--}200\ \mu\text{m}$ , while having the same field of view. From an instrument design perspective this means the blue and red channels had to overlap in their wavelength range, and a dichroic had to be used to split the light between the two channels, allowing both sides to have a common field of view. The drawback was that a dichroic has a transition region where neither the transmission nor the reflection is good. Thus, FIFI-LS had two dichroics with different transition wavelengths. The D105 dichroic cut off the blue channel at about  $100\ \mu\text{m}$  and opened the red at about  $115\ \mu\text{m}$ , while the D130 cut off the blue channel at  $120\ \mu\text{m}$  and opened the red at  $130\ \mu\text{m}$ . [Figure 5](#) shows the optical throughput for all combinations of the dichroic, channel, and order (blue side only). Typically, the D105 was used unless a wavelength between  $100$  and  $115\ \mu\text{m}$  was observed, since on average it had a better throughput in the red channel, and comparable throughput up to  $\sim 90\ \mu\text{m}$  on the blue side.

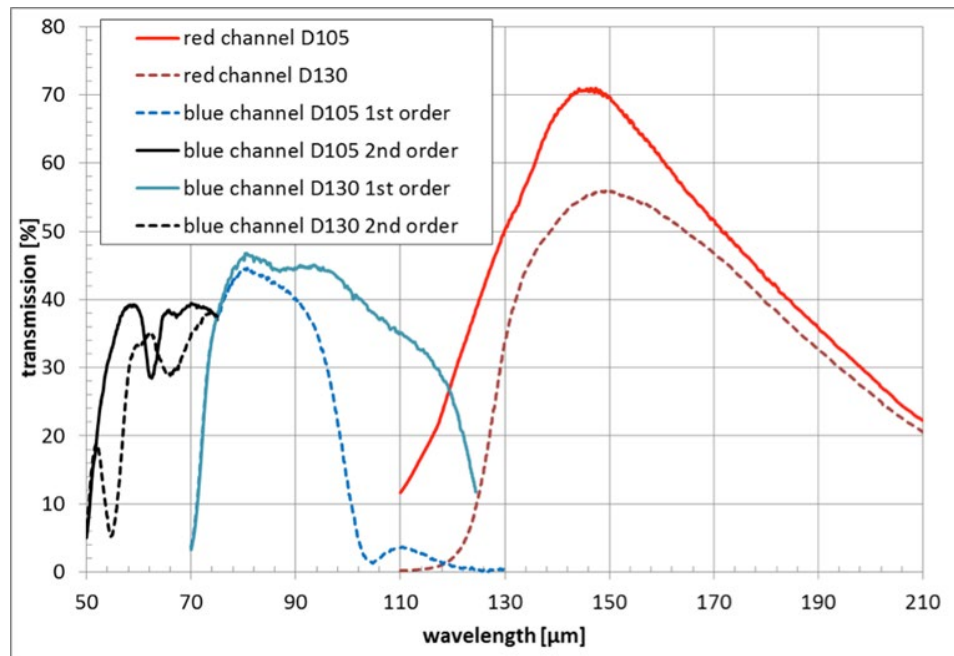


**Figure 5** Throughput of the optical system. Here the transmission of the overall optical system is shown for the six possible optical configurations using two dichroic beam splitters (D105 and D130) and both grating orders (blue channel only).

### 2.3.2 Beam Rotator (K-Mirror)

The SOFIA telescope was essentially an alt-azimuth mounted telescope and could rotate around all three axes by virtue of a spherical bearing, but the amount it could rotate about the cross-elevation (i.e., “azimuth”) and line-of-sight (i.e., “position angle”) axes was limited. During observations, the telescope was inertially stabilized, and the telescope could track the sky rotation

for a limited amount of time. The length of time depended on the target's declination, aircraft heading, and other factors. However, when the telescope reached its limit in line-of-sight rotation, it needed to rewind, which resulted in a rotated FOV of the telescope.

To counteract this, FIFI-LS had a beam rotator (K-mirror) that rotated the instrument's FOV and compensated for the sky rotation that occurred due to a rewind. When a rewind happened, the FIFI-LS beam rotator would automatically rotate the FOV of the instrument, so that the position angle of the instrument's FOV on the sky was kept. The beam rotator also enabled the observer to choose the best on-sky position angle.

### 2.3.3 Internal Calibrator

To measure and monitor the relative spectral responsivity of the different pixels of the detectors, an internal calibrator was built into the FIFI-LS instrument. This used a grey body source that could be set at a given temperature and was thermally connected to the helium optical bench, but it was located outside of the helium shield. The parameters of the continuum source were selected to mimic the typical radiation emitted by the warm telescope. For flat field measurements, the source was kept at a temperature of 150K.

A modified integrating sphere was used as the internal calibration source. The integrating sphere was a hollow sphere with a spark eroded, galvanically gold coated inner surface, which was thermally coupled to the liquid helium reservoir (see [Figure 6](#)). The rough inner surface produced diffuse scattering of the infrared light which was necessary to achieve a uniform illumination of the pupil of FIFI-LS.

A flip mirror was used to switch the optical path between the sky and the internal calibration source.

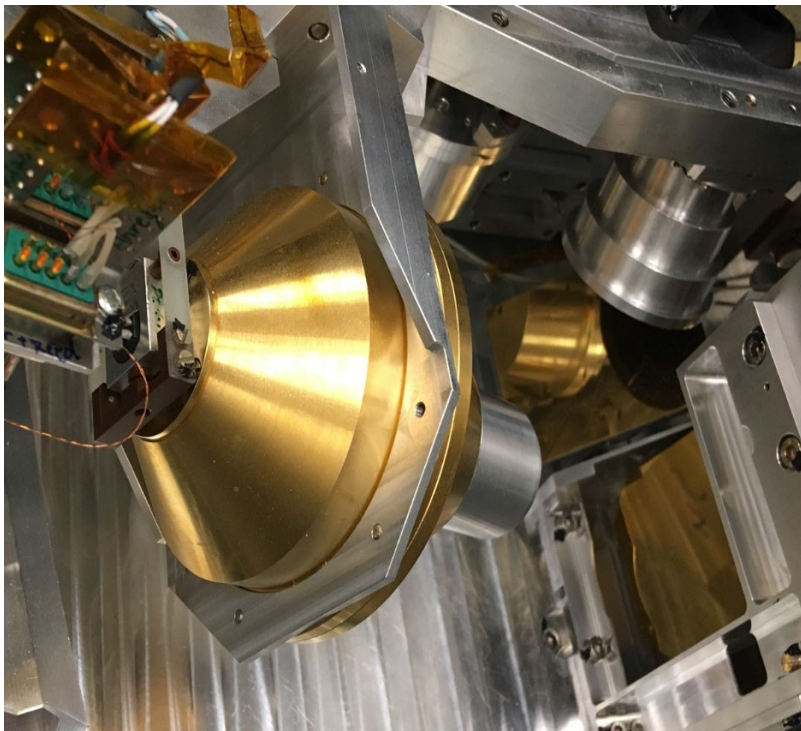


**Figure 6** *Image of the integrating sphere and the flip mirror used to direct the internal calibrator light to the detectors.*



Finally, a system chopped between the black body signal and the diffuse emission inside the instrument.

A more detailed description of the system can be found in the 2008 PhD thesis of Mario Schweitzer ([https://edoc.ub.uni-muenchen.de/8754/1/Schweitzer\\_Mario.pdf](https://edoc.ub.uni-muenchen.de/8754/1/Schweitzer_Mario.pdf)).

### 2.4 OBSERVING MODES

Observations with FIFI-LS required careful background subtraction because the signal from the target was miniscule compared to the stratosphere's high far-infrared background levels and the thermal emission from the telescope's mirrors itself. This was mainly achieved by chopping with SOFIA's secondary mirror and/or by nodding the telescope.

In the chopped modes (symmetric and asymmetric chop) the secondary chopped by tilting the mirror at 2 Hz to efficiently remove the sky emission. To remove the residual background from the telescope not eliminated by chopping, the entire telescope was nodded typically every 30s either to move the source to the other chop-beam or to an off-position. Since the instrument telescope communications and the telescope move took 8s, a whole nod-cycle for a symmetrically chopped observation typically took 76s. In the unchopped modes (OTF and total power) the telescope was only nodded, with integration times varying between 10 and 30s to ensure a sufficiently short nod interval.

Symmetric chopping was the most used observing mode with FIFI-LS since it combined the best background subtraction offered by chopping with good observing efficiency. Asymmetric chopping became necessary for extended sources but also allowed for shorter on source integration times for bright sources. Total power observations were used for even larger and more extended sources where the required chop throw was too far. This mode dispensed with the secondary chopping, and only used telescope nods to alternate between observing the target and a blank field for background subtraction. On-the-fly mapping (OTF) was a mode that enabled good spatial sampling and observing efficiencies for very large maps. This mode worked essentially the same way as the Herschel/PACS spectrometer by scanning over the field of interest and reading out the detector array at a fixed frequency.

The following sections describe in more depth each of the observing modes. In the discussion of the overheads,  $N$  is the number of map positions and  $t_{\text{on}}$  is the exposure time per map position. The chop throw is the on-sky angular distance between the two chop positions, and the chop angle is specified relative to equatorial coordinates or telescope coordinates (e.g., horizontal).

#### 2.4.1 Symmetric Chop and Nod

This mode combined chopping symmetrically around the telescope's optical axis to remove the sky background and most of the telescope background, with a matched telescope nod to remove the residual telescope background. This mode is also known as nod match-chop (NMC) or double beam switch (DBS).

When observing using a symmetric chop, the target was placed on one side of the optical axis, by a certain on-sky angular distance called the chop amplitude. In the FITS header this value is recorded as CHPAMP1. The chop amplitude was chosen so that empty sky free of infrared emission could be observed diametrically across the optical axis from the target by the same chop amplitude length, hence its name symmetric chop. When the telescope was nodded, the optical

axis was moved to the other side of the source and the source got observed in the other chop position. The chop position, which observed the source previously, now observed a sky position, which should also have been free of infrared emission, symmetrically on the other side of the source. Put another way, the telescope was nod-matched to the chop such that it created two off-positions symmetric to the on-source position (Figure 7, left). Note that in some contexts the chop throw value was used instead, which was twice the chop amplitude. Because the target was placed off the optical axis the entire time, large chop amplitudes degraded the image quality due to the introduction of coma. This effect caused asymmetric smearing of the Point Spread Function (PSF) in the direction of the chop. However, the effect was small, affecting the SNR by less than 10% in the red channel for all permitted chop throws, and in the blue channel for total chop throws less than 6 arcmin and wavelengths longer than 63  $\mu\text{m}$ . At shorter wavelengths, a total chop throw of less than 4 arcmin was acceptable, although observations were made successfully with larger throws. Generally, most observations used a chop throw as small as possible while keeping the FOV in the off positions outside of any detectable emission.

The position angle of the chop could be specified relative to equatorial coordinates or telescope coordinates (e.g., horizontal). Horizontal chopping was preferred when it was possible, i.e., for relatively small sources without any other sources of emission in the surrounding field and for which the position angle of the chop was unimportant. This is because it ensured the telescope was observing the same zenith angle and hence the same airmass, keeping the background subtraction as accurate as possible.

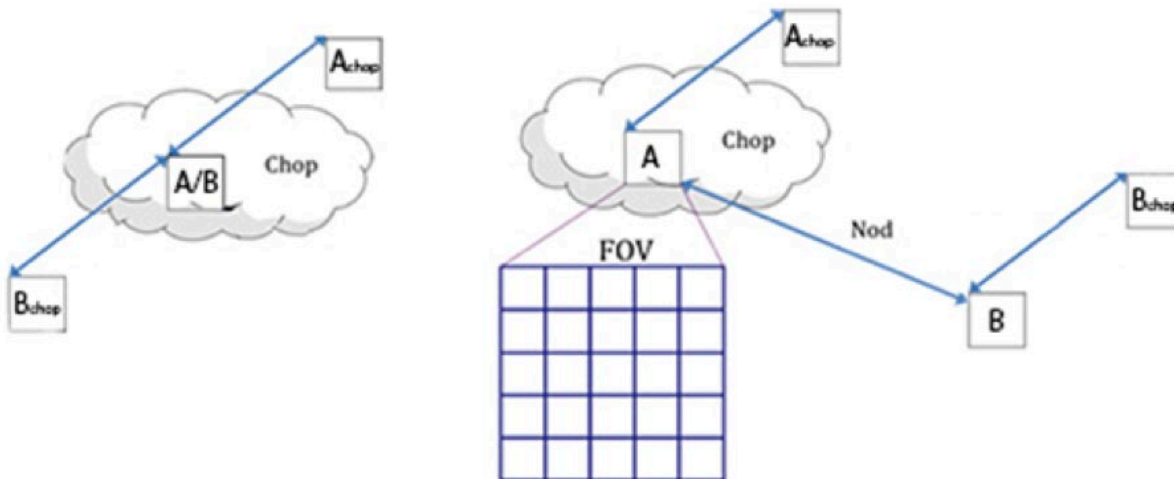


**Figure 7** Illustration of symmetric chop and nod (Left) and asymmetric chop and nod (Right). In the case of symmetric chop and nod, the telescope secondary was chopped between A and A<sub>chop</sub> for 30 sec., then the telescope executed a nod and then chops between B and B<sub>chop</sub> for another 30 sec. A and B in this case are on the target, while A<sub>chop</sub> and B<sub>chop</sub> are used for background subtraction. In asymmetric chop and nod, the A and A<sub>chop</sub> positions are the same as symmetric chop and nod, but both B and B<sub>chop</sub> are on blank sky.

Generally, the total overhead in this mode was about  $1.6Nt_{on}$ , since the source was only observed 50% of the time due to chopping, and additional time was required for telescope moves. This overhead estimate assumed that the time spent on each map position  $t_{on}$  was 30s.

### 2.4.2 Asymmetric Chop and Nod

If the target's size or environment did not allow the Symmetric Chop mode to be used, for example if it was not possible to find clean symmetric chop positions on opposite sides of the source, the Asymmetric Chop mode allowed larger chop throws and needed an emission free field only in one direction from the source. The largest chop throw was  $\sim 10$  arcmin for all wavelengths. It also allowed for faster mapping of extended sources. The asymmetric chop kept the target on the optical axis in most cases, resulting in an image unaffected by coma. Consequently, the off-beam was off-center by twice the amount of a symmetric chop with the same chop throw, resulting in twice as much coma in the off-beam – but as the off-beam should only see empty sky this did not affect the observations. The telescope was nodded to an off position where the same chopped observation was executed to provide the residual background subtraction. [Figure 7](#) (right) illustrates this geometry.

The ‘classical’ asymmetric chop used an ABBA nod pattern, but for most cases a modified ABA nod pattern, which was the default in this mode, was recommended. For the fastest mapping an AABAA nod pattern was available. In both modified nod patterns, the B (off) nod was longer than the individual A (on) nods. For the ABA pattern, the B was 1.5 times the length of the A and for the AABAA pattern the B was 2 times the length of the A. These modified nod patterns were beneficial on very bright objects, where the estimated on-source exposure time per map position was 15s or less so that the total observing time was dominated by telescope movements. The actual patterns were thus ABA' and AA'BA''A''', i.e., the A positions were all different. In this mode, the total overhead was  $3.3Nt_{on}$  assuming an on-source exposure time per map position of 15s for the ABA pattern, and  $3Nt_{on}$ , assuming an on-source exposure per map position of 10s for the AABAA pattern. Note that these overheads increased with shorter integration times. These modified nod patterns were usually used for any source with asymmetric chop if the line was narrow enough to fit within the instrument's instantaneous spectral coverage.

If the line was very wide the ‘classical’ mode had to be used. Here the total overhead in this mode was about  $4.1Nt_{on}$ , since the source was observed during 25% of the observation plus additional time for telescope moves. This overhead estimate assumed that the on-source exposure time per map position  $t_{on}$  was at least 15s.

### 2.4.3 Total Power

In some cases, the target's environment did not allow even a single chop position to be used, such as very extended and/or diffuse objects. In these situations, observations were usually executed using the un-chopped Total Power mode. This used the same ABA pattern for the asymmetric chop mode but without any chopping by the secondary mirror. This could lead to potentially poorer background subtraction, as the only off-source position was the B nod, so there was some additional risk. In stable atmospheric conditions it could give results as good as the symmetric chop mode. In this mode, the total overhead was  $1.9Nt_{on}$ , assuming an on-source exposure time per map position of 10s.

### 2.4.4 On-the-Fly Mapping

The On-The-Fly Mapping (OTF) Mode was introduced within the last two cycles of FIFI-LS observations and was ideal for mapping large areas of bright emission efficiently. In this mode, the telescope was scanned across the source at a constant angular speed, while the detector was read out ‘on the fly’ at a set frequency. Like Total Power, no chopping was done in OTF, so the

same caveats apply here as well. An ‘off’ nod position was taken at the end of each scan through the source, with a time of  $\sqrt{N}t_{\text{samp}}$ , where  $N$  is the number of independent samples (i.e., the total number of readouts) in the scan, and  $t_{\text{samp}}$  is the integration time of a ramp. Furthermore, the same off position was used for each of the scans taken. Each scan took 30s and the on-sky length was determined by the scan speed. The map was built up by scans spaced by the width of the array being used (30" for blue, 60" for red), and (if desired) by crossing scans at right angles.

During an OTF scan the FIFI-LS field of view was rotated at 11.3 degrees to the direction at which the telescope was being driven, giving an equal spacing of the spaxels in the cross-scan direction (Figure 8). Combined with integrations of 1/8th of a second as the telescope moves, this built up a dense array of points at which data were taken giving a good sampling of the spatial PSF.

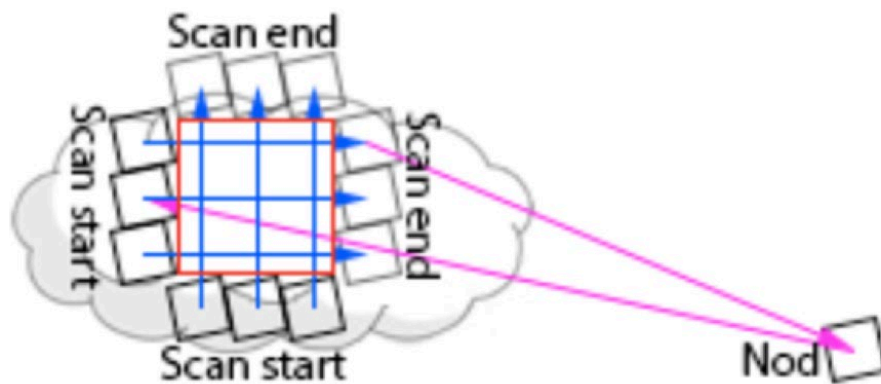


**Figure 8** A schematic of how the OTF mapping mode was executed.

### 2.4.5 Raster Mapping

Raster Mapping was supported by the Symmetric Chop, Asymmetric Chop, and Total Power observing modes, and could be executed on a rectangular grid with a user-defined spacing and extent. It was also possible to supply a list of mapping positions to achieve a map with a custom shape optimized to the source geometry.

For chopped observations, if the source geometry allowed the chopped beams to be positioned symmetrically on both sides of the source, the more efficient Symmetric Chop mode could be used for mapping. If that was not possible, the Asymmetric Chop mode had to be used; for short integrations, one of the modified nod patterns (ABA or AABAA) was preferred.

Figure 9 illustrates mapping with an asymmetric chop. The chopped map (positions A1chop to A3chop in the example) covered an area with the same form as the on-source map, offset by the chop throw. If this was undesirable (e.g., if part of the chopped map would overlap with a region of possible emission), the map needed to be broken up into sub-maps with varying chop parameters. Breaking the map up into individual sub-maps required a separate AOR for each map.

When the on-source integration time was estimated, the differing overlap of the red and blue FOV at the desired raster map spacing had to be considered. The SNR entering the calculation of  $t_{\text{on}}$  was the SNR for a single raster map point. The final SNR for a point in the map should reach  $\sqrt{n} * \text{SNR}$

with  $n$  being the number of raster points from which a point was covered by the respective FOV. For example, in [Figure 9](#), the area of the spaxel in the middle (dark orange) is covered by 3 FOVs while 16 spaxels (light orange) are covered by 2 FOVs and the outer parts of the map (yellow) are covered by 1 FOV. The noise level in the area covered by the central spaxel should thus be  $\sqrt{3}$  lower than in the outer parts and the SNR (for the same signal) thus  $\sqrt{3}$  times higher. (Note that this was an example map, not a suggested mapping strategy.)

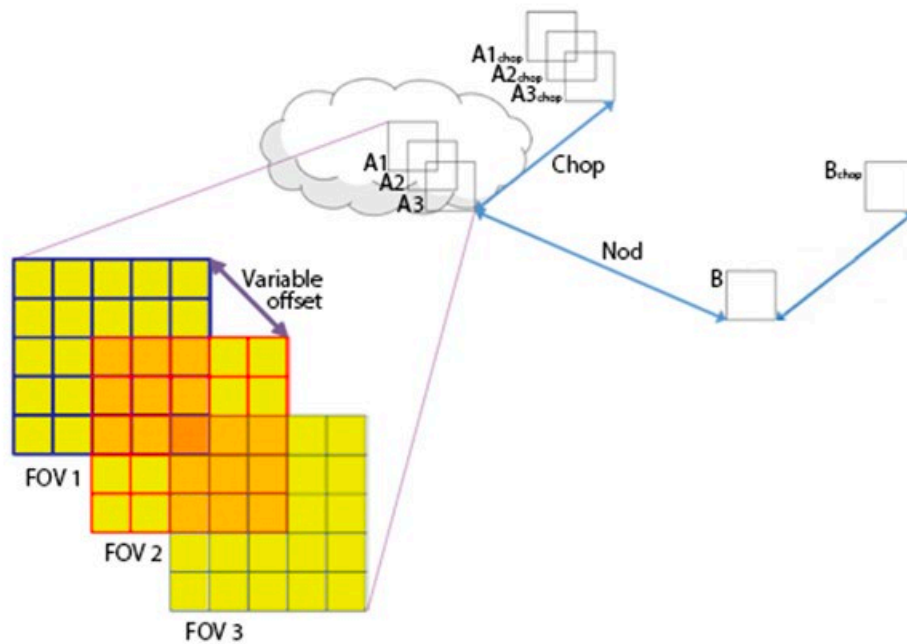


**Figure 9** *The geometry of chopping and nodding while mapping using the asymmetric chop mode.*

### 2.4.6 Spectral Dithering

Spectral dithering was always employed for auto flat-fielding and increased redundancy. It was implemented via a grating scan. The grating was moved in small steps, so that the spectrum moved over different pixels in the spectral dimension of the detector array. The default pattern to cover the instantaneous bandwidth (i.e., what the 16 pixels see centered on the line of interest) was to move the grating 12 steps, each corresponding to half a spectral pixel width. This pattern resulted in a spectrum about 30% wider than the bandwidth. The central 70% of the bandwidth was observed during the whole observing time reaching the full SNR, while the remaining 15% on each side of the bandwidth reached on average approximately 86% of the full SNR. The SNR reached at either extreme of the wavelength range were still 46% on average based on the observing time for each part of the spectrum. For wider spectral coverage, the step size and number of steps of the grating scan were adjusted to achieve the desired spectral coverage and depth. These grating steps were evenly distributed over the nod-cycles.

**3. INSTRUMENT PERFORMANCE**

**3.1 LINEARITY**

In an ideal detector the relationship between the incident flux and the measured voltage is linear along a ramp. The behavior of a linear detector is linear in a limited flux range. After that it becomes non-linear until saturation when it reaches the maximum amount of charge that it can collect, and the measured voltage is no longer related to the incident flux.

To estimate the linearity of the FIFI-LS detectors a quadratic term was considered in the ramps as a first approximation to the observed ramps. By assuming a single non-linearity term, in principle the ramps can be linearized once the coefficient of non-linearity is known. Assume, as was done for the Spitzer IRS<sup>1</sup>, that the observed signal can be written as the sum of the ideal linear signal and a quadratic term that considers the non-linearity of the detector:

$$S_{obs} = S_{lin} + \alpha S_{lin}^2$$

where  $\alpha$  is the non-linearity coefficient.

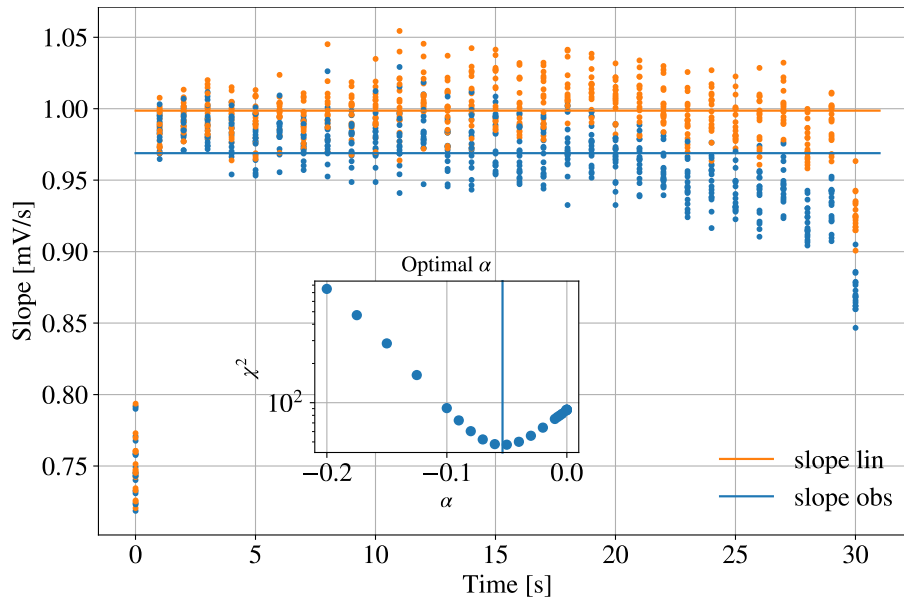


**Figure 10** *Finding the linearity correction.*

Once  $\alpha$  is estimated for each pixel, the equation can be easily inverted to linearize the ramps:

$$S_{lin} = \frac{2S_{obs}}{1 + \sqrt{1 + 4\alpha S_{obs}}}$$

Figure 10 shows the technique used to estimate the optimal value of the quadratic term  $\alpha$  for a particular pixel. The slope between consecutive readout for several ramps is plotted in blue. To evaluate the optimal  $\alpha$  needed for the linearity correction, the  $\chi^2$  of the residuals of the corrected

<sup>1</sup> <https://irsa.ipac.caltech.edu/data/SPITZER/docs/irs/irsinstrumenthandbook/41/>



slope was computed from the median value of the consecutive slopes. The optimal value with the minimum  $\chi^2$  shown in the inset gives the best correction. The slopes of the corrected ramps are shown with orange dots. In the computation the first and last slope are discarded since they are affected by the reset and chop change.

Figure 11 shows the values for the linearity correction coefficient  $\alpha$  and the saturation level of the ramp for each pixel in the red array. Comparable results are obtained for the blue array. Ramps saturate with voltages greater the 2.4 V, while  $\alpha$  is typically around -0.03 except for a few pixels with higher saturation values.

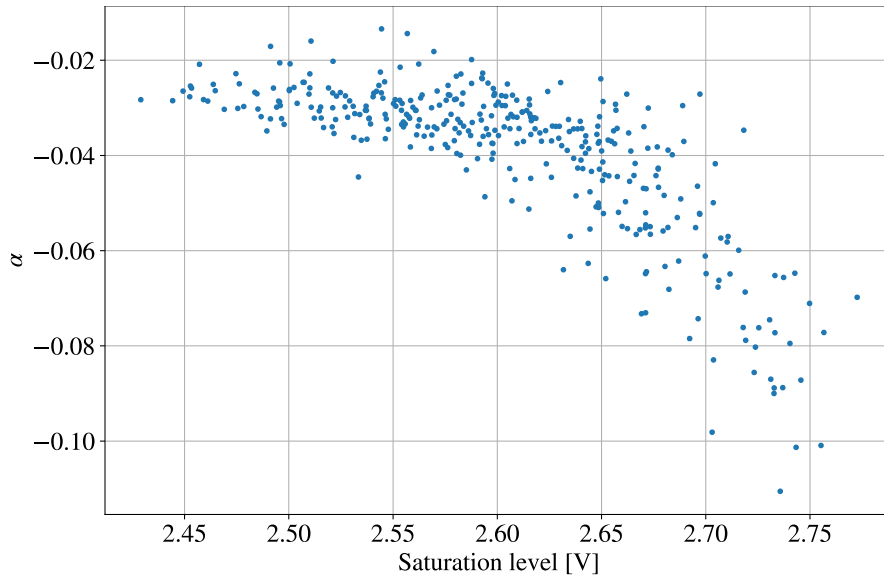


**Figure 11** Ramp saturation and linearity correction

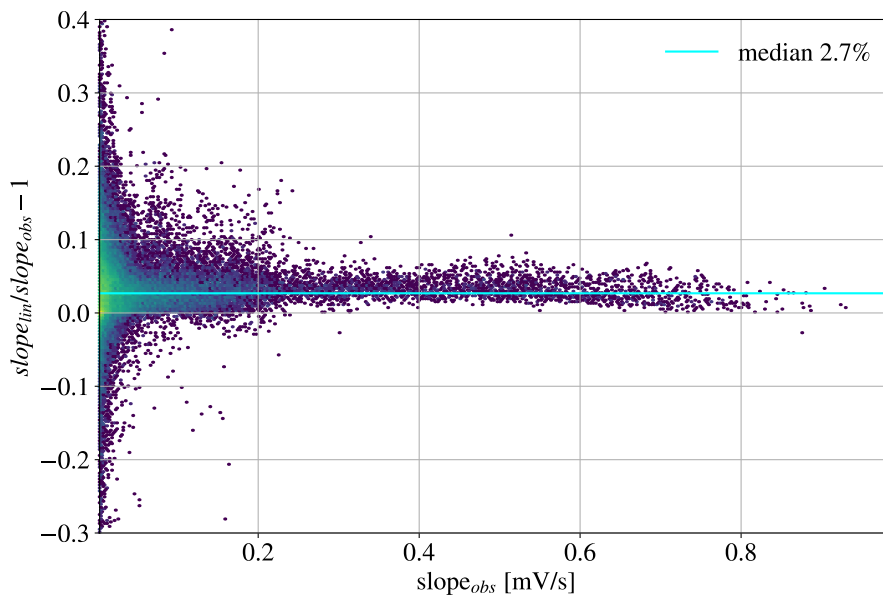


**Figure 12** The effect of linearization is less than 3%

Finally, [Figure 12](#) shows the effect of linearizing the ramps on the estimate of their slopes in the case of the red array. The comparison is between all the observations of Mars with the red array done on flight 312. There is a systematic effect corresponding to less than 3% of the slope. However, the dispersion is less than 1% for slopes higher than 0.1mV/s. Since the systematic effect is absorbed by the flux calibration (which will also be systematically higher), the effect of the linearization of the ramps is in general around 1%. *For this reason, the linearization of the ramps was not introduced in the FIFI-LS pipeline.*

#### 3.2 LINE PROFILE AND SPECTRAL RESOLUTION

Several lines were measured in the laboratory before each observational run with the purpose of calibrating the instrument in wavelength. To have a high signal-to-noise signal, these measurements were done with ‘pure H<sub>2</sub>O’ at a pressure of 5 mBar. However, some of these lines were broader than the spectral resolution of FIFI-LS. To better study their profile and the spectral resolution at different wavelengths, a few lines were also observed with ‘air’ cells which had air at the pressure of 10 mBar. The list of the lines used is reported in [Colditz et al. \(2018\)](#) except for two new lines (47.9732 and 51.0711 μm) which were added in 2018 when the filter window was changed to extend the range of FIFI-LS down to 47μm.

To study the line profiles, the lines were fit with several functions: Gaussian, Voigt, pseudo-Voigt, and asymmetric functions such as a skewed Gaussian, a skewed Voigt, and an asymmetric pseudo-Voigt. For all these functions the implementation in the Python package *lmfit*<sup>2</sup> was used except for the asymmetric pseudo-Voigt which followed the article where it was proposed ([Stankic et al. 2008](#)).

The pseudo-Voigt profile is a particularly good approximation of the Voigt profile obtained as a sum of fractional contributions of the Gaussian and Lorentzian profiles

$$PV(\lambda) = f G(\lambda) + (1 - f) L(\lambda)$$

with  $0 \leq f \leq 1$ .

By modifying the dispersion as a function of the distance from the center of the line:

$$\sigma_a = \frac{2\sigma}{1 + e^{a(\lambda - \lambda_0)}}$$

With  $a$  parameter of asymmetry and  $\lambda_0$ , center of the line, the asymmetric pseudo-Voigt profile is obtained.

[Figure 13](#) shows two examples of line profiles in the blue channel. In general, lines in the blue 2<sup>nd</sup> order are slightly asymmetric and can be well fitted with a skewed Gaussian or an asymmetric pseudo-Voigt. The case of the 1<sup>st</sup> order in the blue is different. As already remarked by [Colditz et al. 2018](#) (see [Figure 3](#) therein), the profile of the line changes in different spaxels. The combination of all the spaxel signals results in an asymmetric profile with a bump on the higher wavelength

<sup>2</sup> [https://lmfit.github.io/lmfit-py/builtin\\_models.html](https://lmfit.github.io/lmfit-py/builtin_models.html)



### 3. INSTRUMENT PERFORMANCE

side. The best shapes to reproduce this unusual profile are either the skewed Gaussian or the asymmetric pseudo-Voigt.

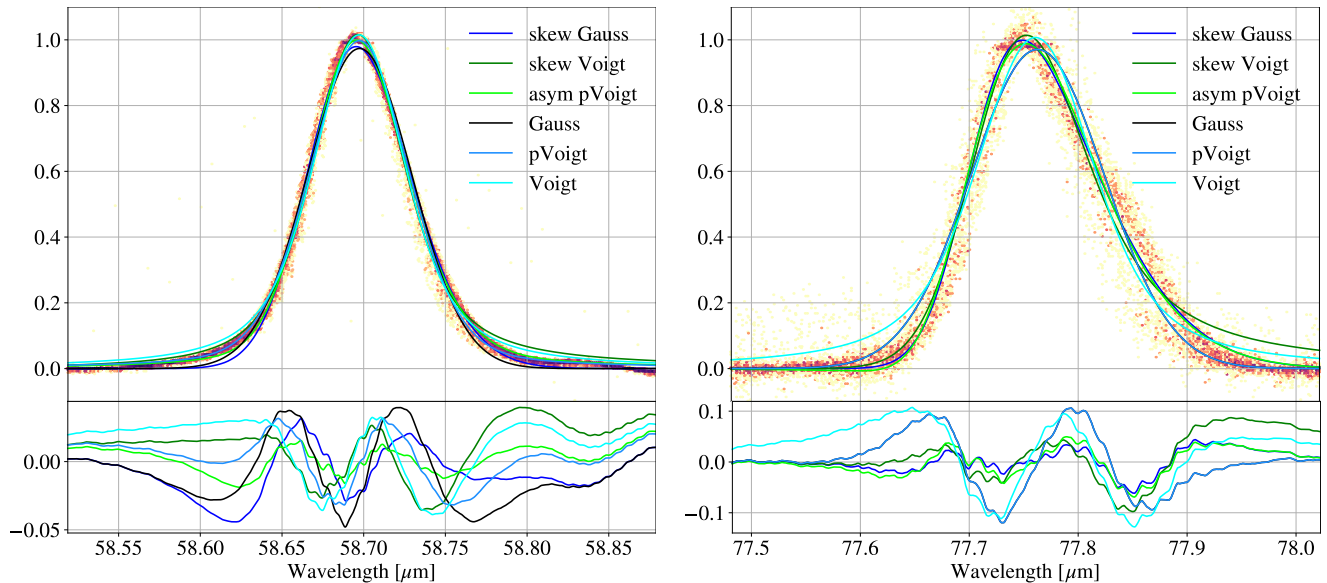


**Figure 13** *Asymmetric line profiles of the blue channel; (Left) 2nd order; (Right) 1st order*

The profile of the lines in the red array are much more regular ([Figure 14](#)). They can be fitted very well with a simple pseudo-Voigt. The profile is well behaved and has the smallest residuals among the different bands.

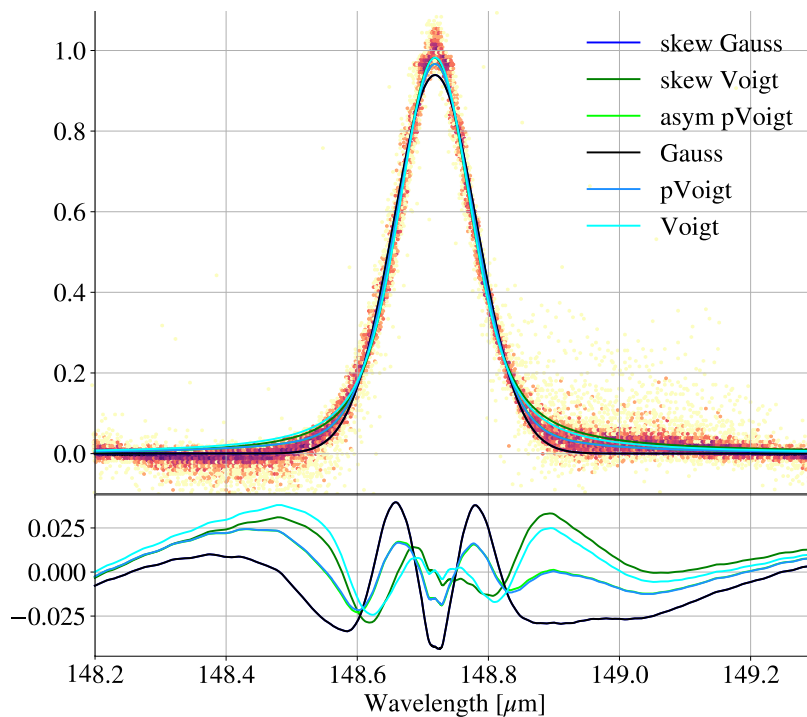


**Figure 14** *Symmetric line profile of the red channel.*

To measure the full-width half-maximum (FWHM) of the lines, the combination of all the measurements normalized to 1 were smoothed as shown in the top panel of the previous figures with the non-parametric fitting technique called LOWESS, which is available in the *statsmodel* library in Python. The width at 0.5 was then directly measured.

Figure 15 shows the spectral resolution, which relies on the measured FWHM values from the fits to the lines at different wavelengths.. The red points are done using water vapor cells, while the blue points correspond to measurements with ambient air cells. Pure water vapor gives a stronger emission but also a wider FWHM. Lines with a water vapor FWHM close or worse than the spectral resolution were observed with air cells.

In the fit to obtain a relationship for the spectral resolution, lines measured with H<sub>2</sub>O cells, which are broader than the spectral resolution, were not considered. The plot reports some of these measurements in different series to show how they are spread because the H<sub>2</sub>O quantity in the cell is variable. They are represented as lower limits with an arrow pointed upwards instead of an error bar.

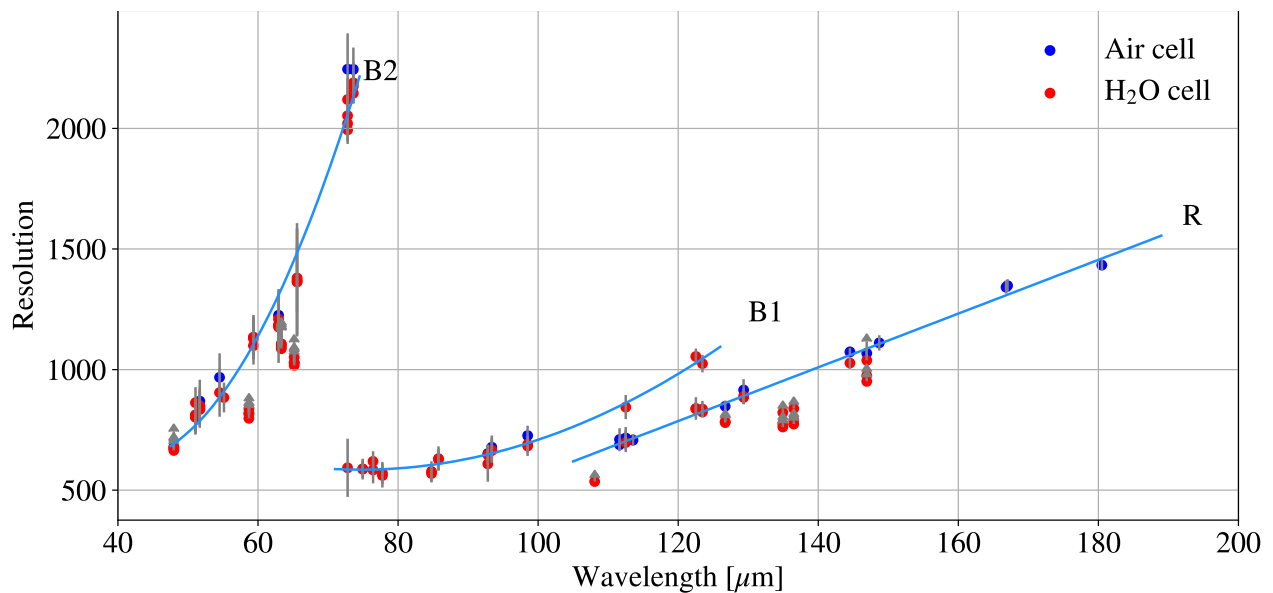


Figure 15 *Measured spectral resolution vs wavelength.*

The reported values are median values of the measurements in all the spaxels, while the dispersion values correspond to the dispersion of the values in the different spaxels.

A polynomial has been fitted to the points to obtain the dependency of the resolution on the wavelength. A second-degree polynomial is used for the blue array while, in the case of the red array, a first-degree polynomial is sufficient to fit the relationship. The fitted relationships are:

$$R = 11.14\lambda - 550.28[\text{Red}]$$

### 3. INSTRUMENT PERFORMANCE

$$R = 0.1934\lambda^2 - 28.89\lambda + 1664 \quad [\text{Blue}, 1^{\text{st}} \text{order}]$$

$$R = 1.937\lambda^2 - 113.7\lambda + 2932 \quad [\text{Blue}, 2^{\text{nd}} \text{order}]$$

The wavelength,  $\lambda$ , is expressed in  $\mu\text{m}$ . These relationships are used in the pipeline to resample the data at the desired multiple of the FWHM for a given wavelength.

**Table 4: Measurements of the Beam Size**

Source Name	Flight Number	Band	Wavelength [ $\mu\text{m}$ ]	FWHM [arcsec]
Uranus	636	B2	52.0	$7.1 \pm 0.8$
Uranus	636	R	158.5	$15.3 \pm 2.2$
Uranus	665	B2	62.1	$7.5 \pm 0.9$
Uranus	665	B1	88.35	$8.8 \pm 1.0$
Uranus	665	R	145.45	$14.2 \pm 3.4$
Uranus	665	R	185.85	$17.6 \pm 4.7$
Callisto	680	R	129.8	$13.0 \pm 0.2$
Callisto	680	R	142.3	$13.9 \pm 0.8$
Callisto	680	R	172.5	$16.1 \pm 1.3$
IRC+10216	737	R	157.7	$15.2 \pm 1.4$
Ganymede	738	B2	69.3	$7.5 \pm 0.7$
Ganymede	738	R	130.1	$13.6 \pm 1.6$
Europa	740	B1	97.1	$9.5 \pm 0.9$
Ceres	806	B1	102.6	$9.8 \pm 0.7$
Ceres	806	B1	110.5	$10.7 \pm 0.7$
Ceres	806	R	142.2	$13.8 \pm 1.4$
Ceres	806	R	150.1	$13.7 \pm 1.9$

**3.3 SPATIAL RESOLUTION**

As shown in [Figure 16](#), the instrumental point spread function (PSF) has a FWHM usually smaller than the diffraction limit of the telescope, except for the 2<sup>nd</sup> order in the blue where it is bigger (see [Colditz et al. 2018](#) for further discussion). To better study the instrumental effects on the size of PSF, several point sources at different key wavelengths in the red array and the two orders of the blue array were observed (see [Table 5](#)).

For such observations a fine dithering pattern was used to better recover the shape of the PSF. A Moffat function was then fitted to the distribution of the fluxes as a function of the distance from the center of the target. [Table 5](#) reports the objects and measurements considered to obtain the spatial resolution of FIFI-LS as a function of the wavelength. These values are plotted in [Figure 16](#) overlotted with the diffraction limit of the telescope (as a continuous grey line), the instrumental contribution to the PSF, and the total FWHM obtaining by combining quadratically these two components.

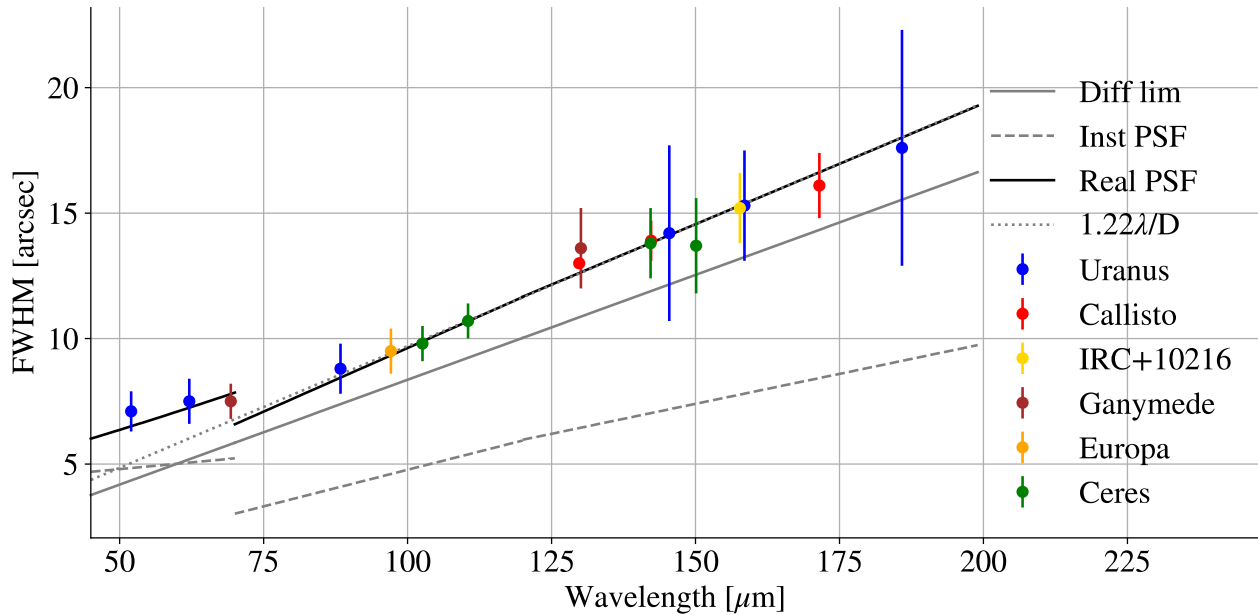


**Figure 16** *Measured beam size vs wavelength.*

The diffraction limited is computed using the formula of the point spread function for obstructed mirrors:

$$I[u] = \frac{1}{(1-\epsilon^2)^2} \left[ \frac{2J_1(u)}{u} - \epsilon^2 \frac{2J_1(\epsilon u)}{\epsilon u} \right]^2,$$

with  $u = \frac{\pi}{\lambda} D$ ,  $D$  diameter of the mirror, and  $\epsilon$  the fractional radius of the central obscuration of the primary aperture. The assumed diameter is 2.5 m, and the obstruction factor is  $\epsilon = 0.42/2.5$ . The FWHM corresponds to the distance at which  $I[u]$  drops to half of the central value, which leads to the formula:

$$FWHM[rad] = 1.013 \cdot 10^{-6} \cdot \frac{\lambda[\mu m]}{D[m]},$$

a value slightly smaller than that of an unobstructed mirror.

To compute the instrumental contributions, the geometric mean of the parameters in Table 3 of [Colditz et al. \(2018\)](#) were considered in the two dimensions (along and perpendicular to the slits) and the conversion factor 3.55 from mm to arcsec on the sky estimated for the FIFI-LS telescope simulator was used. The values were then shifted by subtracting 2.6, 0.8, and 5.0 arcsec for the blue 2<sup>nd</sup> order, 1<sup>st</sup> order, and red arrays, respectively, to better fit the measured points. The parameters for the instrumental PSF are obtained with a simulated source which is not perfectly point-like, so the contribution is overestimated.

Finally, for reference the diffraction limit for an unobstructed mirror of the same size as the SOFIA telescope was overplotted, with a dotted line, using the standard formula  $1.22\lambda/D$ , with  $D$  the diameter of the telescope mirror.

Except for wavelengths shorter than 70 $\mu$ m, this is a good approximation of the FWHM of the FIFI-LS point spread function. Simple linear relationships can be used to estimate the FIFI-LS spatial resolution at different wavelengths:

$$FWHM[arcsec] = 0.097 \cdot \lambda[\mu m] \quad \text{red, blue 1}^{\text{st}} \text{ order}$$

$$FWHM[arcsec] = 3 + 0.07 \cdot \lambda[\mu m] \quad \text{blue 2}^{\text{nd}} \text{ order}$$

#### 3.4 WAVELENGTH CALIBRATION AND ACCURACY

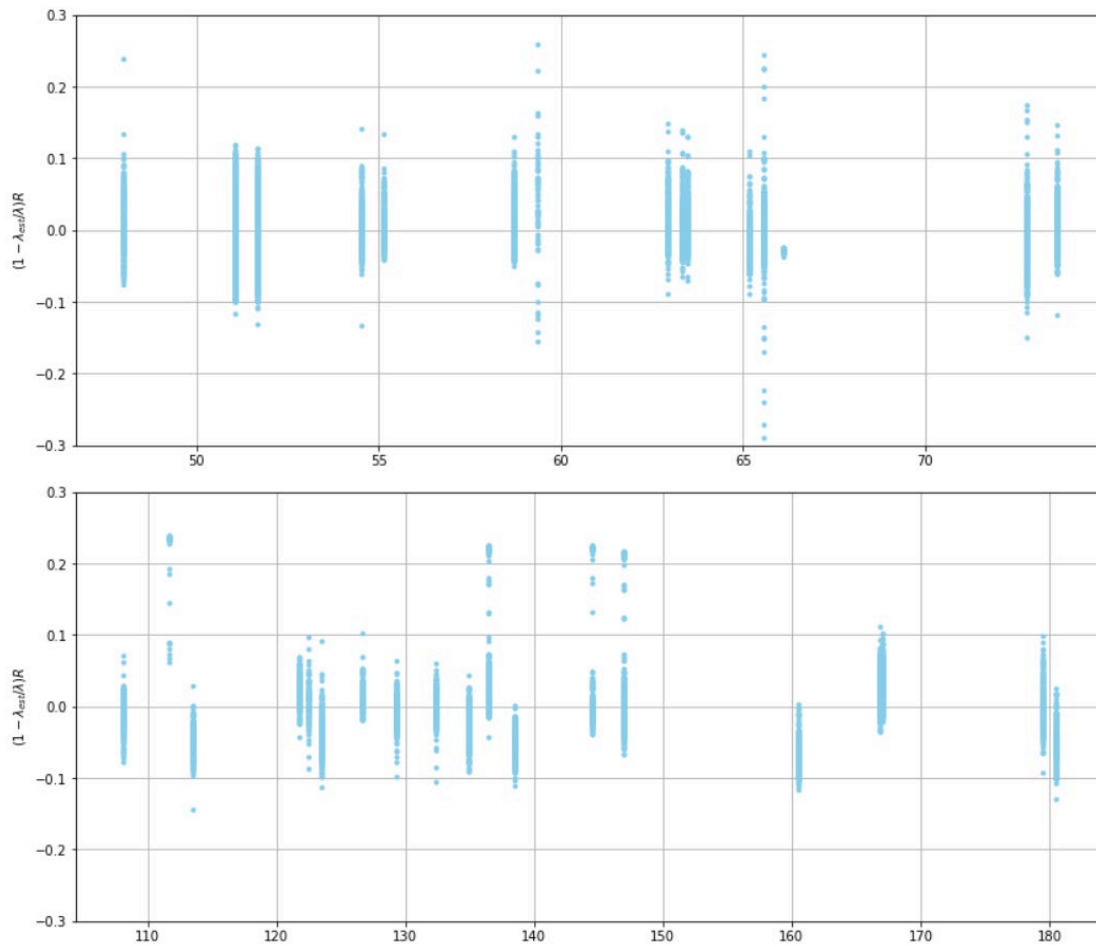
The wavelength calibration is computed by measuring several narrow water vapor lines across the wavelength range of the blue and red array in the laboratory. The procedure and its mathematical basis are explained in detail in [Colditz et al. \(2018\)](#). The formulae used to connect the grating position to the wavelength for each pixel are reported in Section [4.4.5](#).

[Figure 17](#) shows how the ratio  $\frac{\lambda - \lambda_{obs}}{\lambda/R} = (1 - \lambda_{obs}/\lambda)R$  which corresponds to ratio between the error in recovering the wavelength of the line and the spectral resolution elements varies with the wavelength. Each point corresponds to the measurement on a pixel of the detector. The difference between the measured wavelength and the expected wavelength for each line is better than 10% of the spectral resolution.

#### 3.1 FLAT FIELDS

Spectral scans of the interior calibrator are used to estimate the flats in the different arrays, orders, and dichroics. The interior calibrator is heated at 150 K to have a signal close to the background radiation observed in flight. These measurements were repeated before each flight to account for small mechanical changes in the instruments produced by different cool downs.

The biggest effect of these changes was the variation in illumination of the array. Slight differences in the optical path produced changes in the illumination patterns. To estimate such variations, the median flux detected in all the pixels of a spaxel were considered and the ratio of such values to the median flux of all the spaxels were computed.



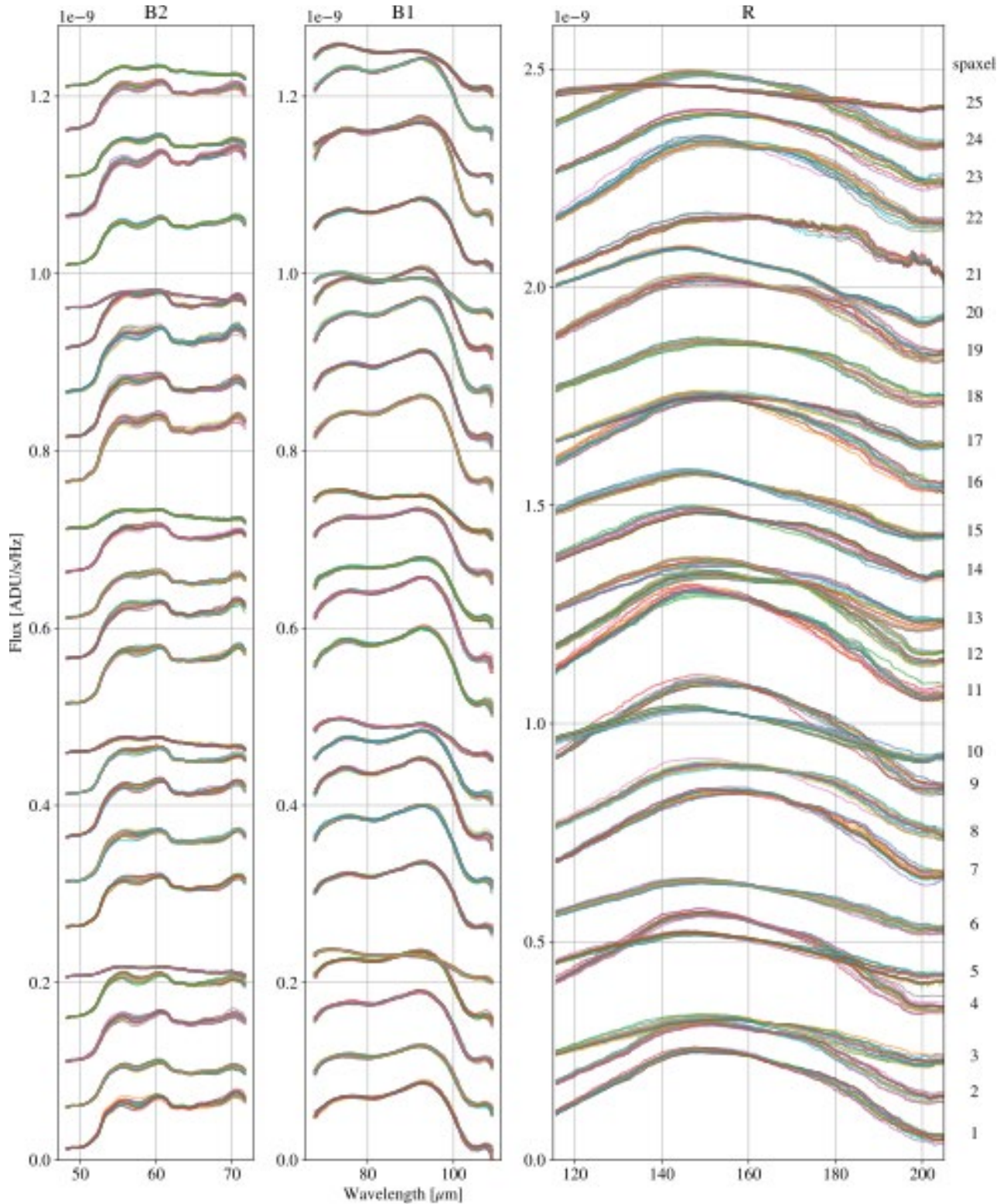
**Figure 17** *Accuracy of the wavelength calibration.*

Figure 18 shows the curves measured in March 2018 using the dichroic splitting the light at  $105\mu\text{m}$ . For each spaxel, the curves of its 16 pixels have been rescaled to a median value. In the blue array (two orders in the left side part of Figure 18) the different pixels have a similar response. The situation is different for the red array, where the curves differ much more, especially at the longest wavelengths.

This behavior can be explained by the fact that the detector elements in the red array were compressed in their mounting structures to shift the area of good spectral sensitivity into the wavelength range of  $120\text{-}210\mu\text{m}$  ([Rosenthal et al. 2000](#)). Since the pressure applied was not perfectly even, the shape of the response curves of the different pixels varied more than those of the blue array, and were even worse at the far-IR end where the detector sensitivity was the lowest.



### 3. INSTRUMENT PERFORMANCE



**Figure 18** *The spectral response curves for the 25 individual spaxels as measured in October 2018. Note the multiple curves for each spaxel are from the 16 individual pixels that comprise each spaxel.*

### 3. INSTRUMENT PERFORMANCE

The spatial flats have been derived from the ratio of the median spaxels curves (Figure 18) to the median curve. As they vary between cooldowns of the instrument, they have been derived for each observing series. The spatial flats for the two arrays are plotted in Figure 19.

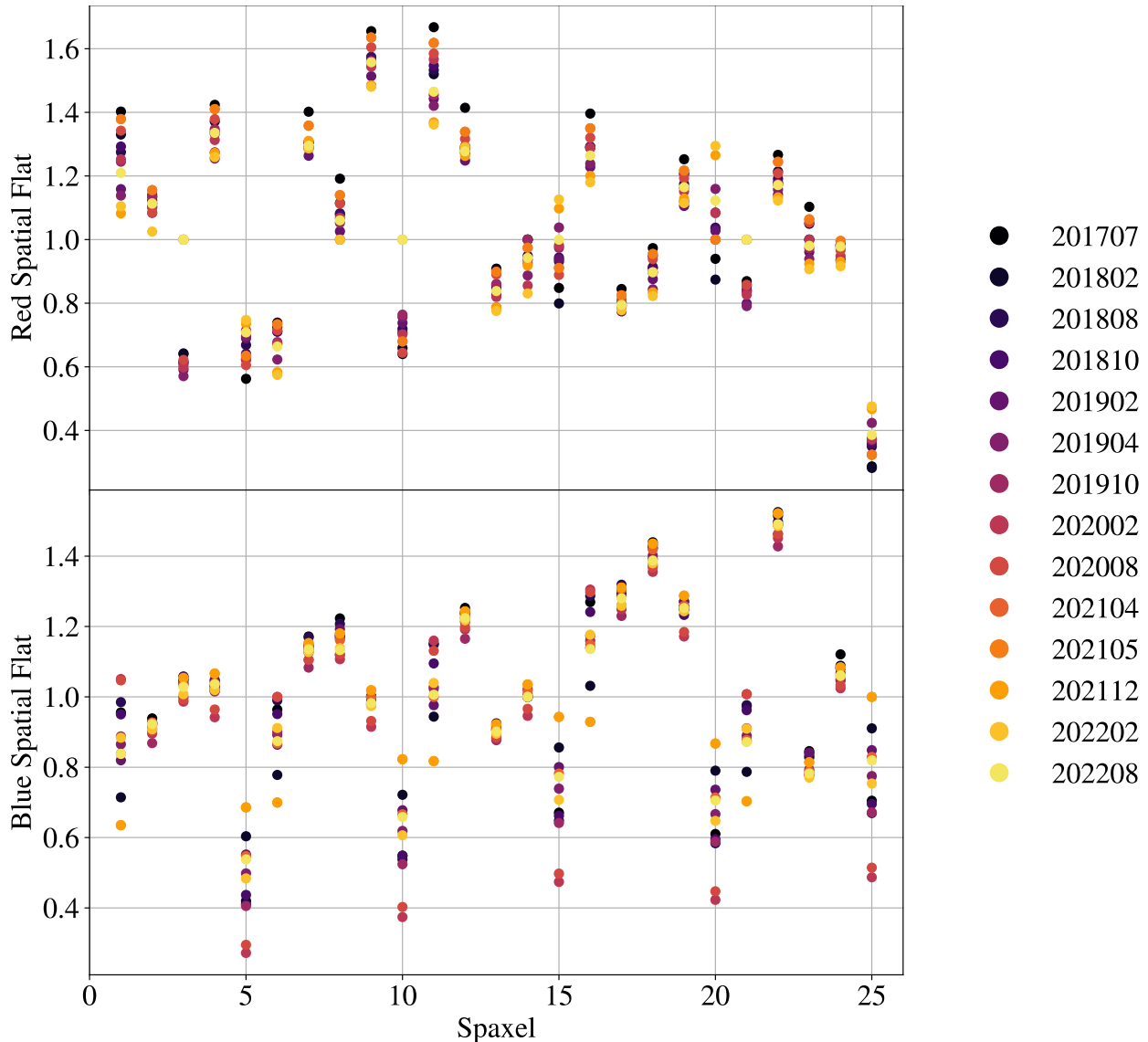


**Figure 19** *Spatial flatfields for each spaxel (derived from the median spectral response curves) as measured over the lifetime of FIFI-LS.*

The spaxels relative to one of the lateral columns (5, 10, 15, 20, and 25) usually have the lowest fluxes and the biggest dispersions between observing series. These spaxels are only partially illuminated. For this reason, these were not considered when obtaining the median signal from the various pixels and when obtaining the response curve.

Once all the pixels of each spaxel were renormalized with the spatial flat fields, for each pixel, the ratio of the pixel curve to the median curve of all the array was coadded. A Chebyshev polynomial



### 3. INSTRUMENT PERFORMANCE

was then computed to smooth the distribution of points from all the series and saved as spectral flats. [Figure 20](#) shows, as an example, the spectral flats for all the spaxels of the red array, dichroic 105 $\mu\text{m}$ , pixel 6. The blue lines correspond to the measurements from all the FIFI-LS series after applying the spatial flats of each series. The black lines are the accepted flats computed via a Chebyshev polynomial smoothing.

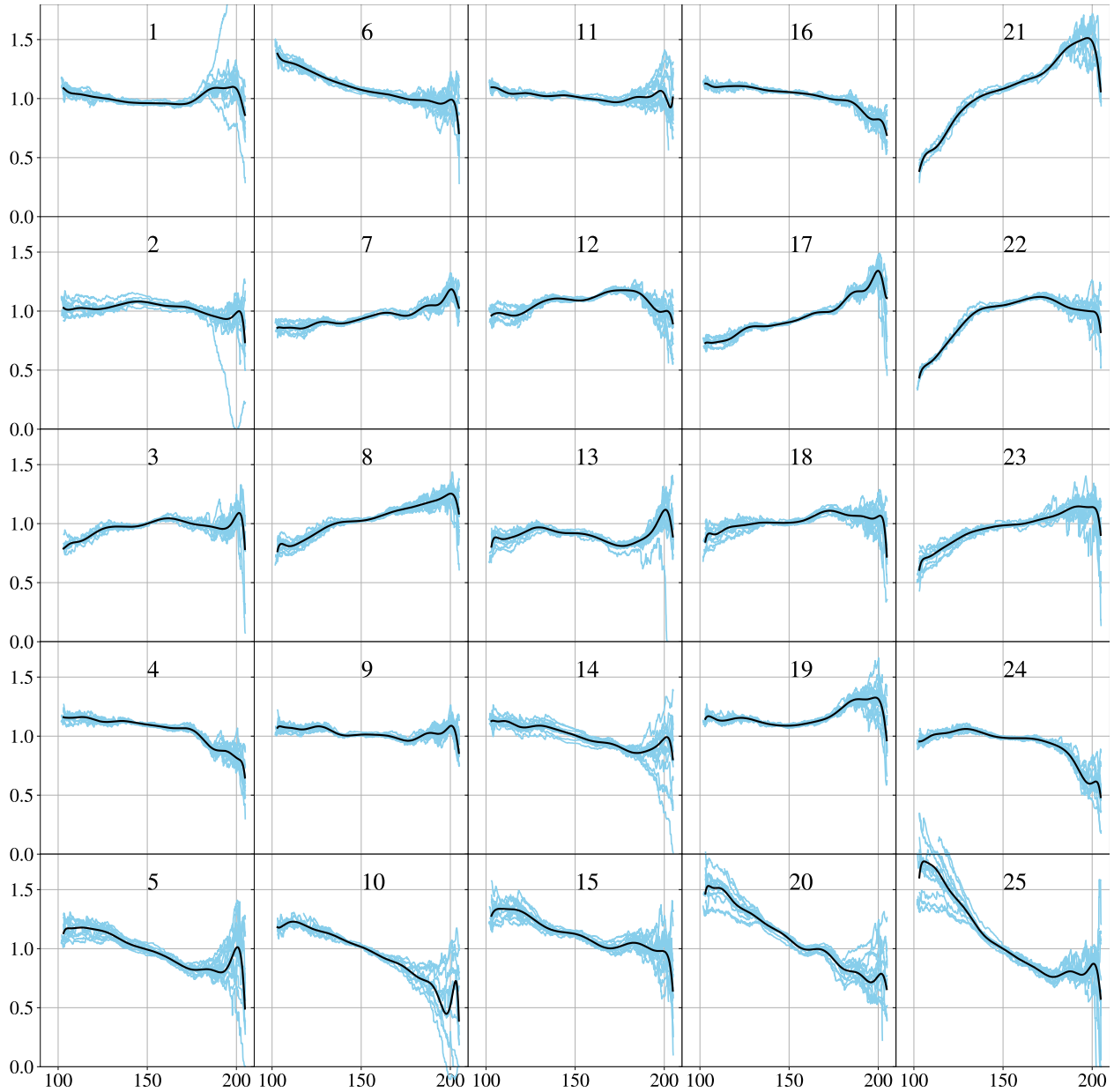


**Figure 20** The spectral flatfields for pixel 6 in all 25 spaxels of the red array over all FIFI-LS flight series are shown in blue. The black line is the accepted flatfield curve after smoothing by a Chebyshev polynomial.

#### 3.2 ABSOLUTE FLUX CALIBRATION

Several sky calibrators were observed during the lifetime of FIFI-LS. The primary calibrator was Mars since it is very bright at any wavelength observed with FIFI-LS. Even if it did not appear as a point source in certain periods of the year, it was always so small that it was completely covered by the FIFI-LS blue and red arrays.

Secondary calibrators used were Uranus, Jovian moons, and bright asteroids. In the present work, they were used only when needed since the signal from these sources is very faint. They were not used to define the response of the red array. [Table 6](#) lists the calibrators observed with the first filter window between 2015 and 2017. [Table 7](#) has the list of calibrators observed with the most recent filter window between 2018 and 2022.

**Table 5: Flux Calibration Measurements (Old Window)**

Date	Flight	Source	Band	Range [ $\mu\text{m}$ ]	Xfact
2015 Oct 22	249	Mars	B1-105	76-96	0.90
2015 Oct 22	249	Mars	R-105	126-156	0.95
2016 Feb 27	281	Mars	B2-105	59-75	1.03
2016 Mar 01	282	Mars	B2-105	51-61	1.00
2016 Mar 01	282	Mars	B1-130	86-104	1.04
2016 Mar 01	282	Mars	R-105	118-148	1.01
2016 Mar 01	282	Mars	R-130	169-188	1.00
2016 Mar 09	286	Mars	B1-105	74-96	0.99
2016 Mar 09	286	Mars	R-105	124-158	1.00
2016 Jun 30	312	Mars	B2-105	51-70	0.99
2016 Jun 30	312	Mars	R-105	118-175	1.11
2016 Jul 03	314	Mars	B1-105	71-118	0.97
2016 Jul 03	314	Mars	R-105	163-201	0.96
2016 Jul 05	316	Mars	B1-130	114-125	0.92
2016 Jul 05	316	Mars	R-105	198-205	0.95
2016 Jul 05	316	Mars	R-130	145-192	0.94
2016 Jul 06	317	Mars	B1-130	110-124	0.99
2016 Jul 06	317	Mars	B2-105	51-55	1.00
2016 Jul 06	317	Mars	B2-130	56-71	1.00
2016 Jul 06	317	Mars	R-105	118-130	1.13
2016 Jul 06	317	Mars	R-130	129-205	1.09
2017 Mar 01	380	Callisto	B1-105	71-94	1.01
2017 Mar 01	380	Callisto	B1-130	71-105	1.02
2017 Mar 03	382	Callisto	B1-130	91-124	1.00
2017 Jul 26	422	Uranus	B1-105	69-72	1.03
2017 Jul 28	424	Uranus	B1-105	70-108	1.01

**Table 6: Flux Calibration Measurements (New Window)**

Date	Flight	Source	Band	Range [ $\mu\text{m}$ ]	Xfact
2018 Nov 06	524	Mars	B1-105	65-105	0.85
2018 Nov 06	524	Mars	B2-105	50-68	0.89
2018 Nov 06	524	Mars	R-105	115-205	0.87
2018 Nov 07	525	Mars	B1-130	65-125	0.95
2018 Nov 07	525	Mars	R-130	145-205	0.97
2018 Nov 08	526	Mars	B1-130	119-126	0.86
2018 Nov 08	526	Mars	B2-130	51-71	0.92
2018 Nov 08	526	Mars	R-130	120-175/200-205	0.90
2018 Nov 09	527	Mars	B1-105	68-74	0.92
2018 Nov 09	527	Mars	B2-105	50-74	0.95
2018 Nov 09	527	Mars	R-105	115-188	1.03
2019 Feb 27	548	Mars	B1-130	65-110	0.98
2019 Feb 27	548	Mars	B2-105	50-66	0.98
2019 Feb 27	548	Mars	R-105	115-168	0.99
2019 Feb 27	548	Mars	R-130	145-190	1.01
2019 Feb 28	549	Mars	B1-105	65-105	1.00
2019 Feb 28	549	Mars	B2-130	49-55	1.00
2019 Feb 28	549	Mars	R-105	155-205	1.01
2019 Feb 28	549	Mars	R-130	120-131	1.00
2019 May 02	563	Mars	B2-105	50-60	0.97
2019 May 02	563	Mars	B2-130	50-65	1.04
2019 May 02	563	Mars	R-105	185-205	0.82
2019 May 02	563	Mars	R-130	181-205	0.89
2021 Apr 13	716	Mars	B2-105	50-60	1.06
2021 Apr 13	716	Mars	R-105	115-148	0.96
2021 Apr 14	717	Mars	B1-105	67-87	1.05
2021 Apr 14	717	Mars	B2-130	50-70	0.97
2021 Apr 14	717	Mars	R-105	156-178	1.00
2021 Apr 14	717	Mars	R-130	120-172	0.94
2021 Apr 20	720	Mars	B1-130	65-126	1.00
2021 Apr 20	720	Mars	R-105	150-155	0.95
2021 Apr 20	720	Mars	R-130	145-205	0.94
2021 Apr 21	721	Mars	B1-105	86-105	1.01
2021 Apr 21	721	Mars	B2-105	59-72	1.02
2021 Apr 21	721	Mars	R-105	145-205	0.93
2022 Mar 23	843	Mars	B1-105	65-98	1.06
2022 Mar 23	843	Mars	B2-130	50-70	1.12
2022 Mar 23	843	Mars	R-105	142-188	1.15
2022 Mar 23	843	Mars	R-130	125-178	1.16
2022 Mar 28	846	Mars	B1-130	84-90	1.21
2022 Mar 28	846	Mars	B2-105	51-72	1.11
2022 Mar 28	846	Mars	R-105	118-185	1.12
2022 Mar 28	846	Mars	R-130	162-169	1.20
2022 Mar 29	847	Mars	B1-130	85-130	1.16
2022 Mar 29	847	Mars	B2-105	49-53	1.18
2022 Aug 25	847	Mars	R-105	118-122/182-202	1.16
2022 Mar 29	847	Mars	R-130	167-205	1.19
2022 Aug 25	906	Mars	B1-105	65-105	0.92
2022 Aug 25	906	Mars	B1-130	65-128	1.00
2022 Mar 29	906	Mars	R-105	145-202	1.01
2022 Aug 25	906	Mars	R-130	143-205	1.09

### 3. INSTRUMENT PERFORMANCE

The models used for the absolute flux of Mars are the ones developed for Herschel by Lellouch and Moreno<sup>3</sup>. In the case of Uranus, the ESA4 model developed by [Orton et al. \(2014\)](#) was used, which was also used for the calibration of PACS on Herschel.

For the Jovian moons, the ESA2 models developed for Herschel by Moreno (see [Mueller et al. 2016](#)) were used. All these models are distributed with the SOFIA pipelines<sup>4</sup>.

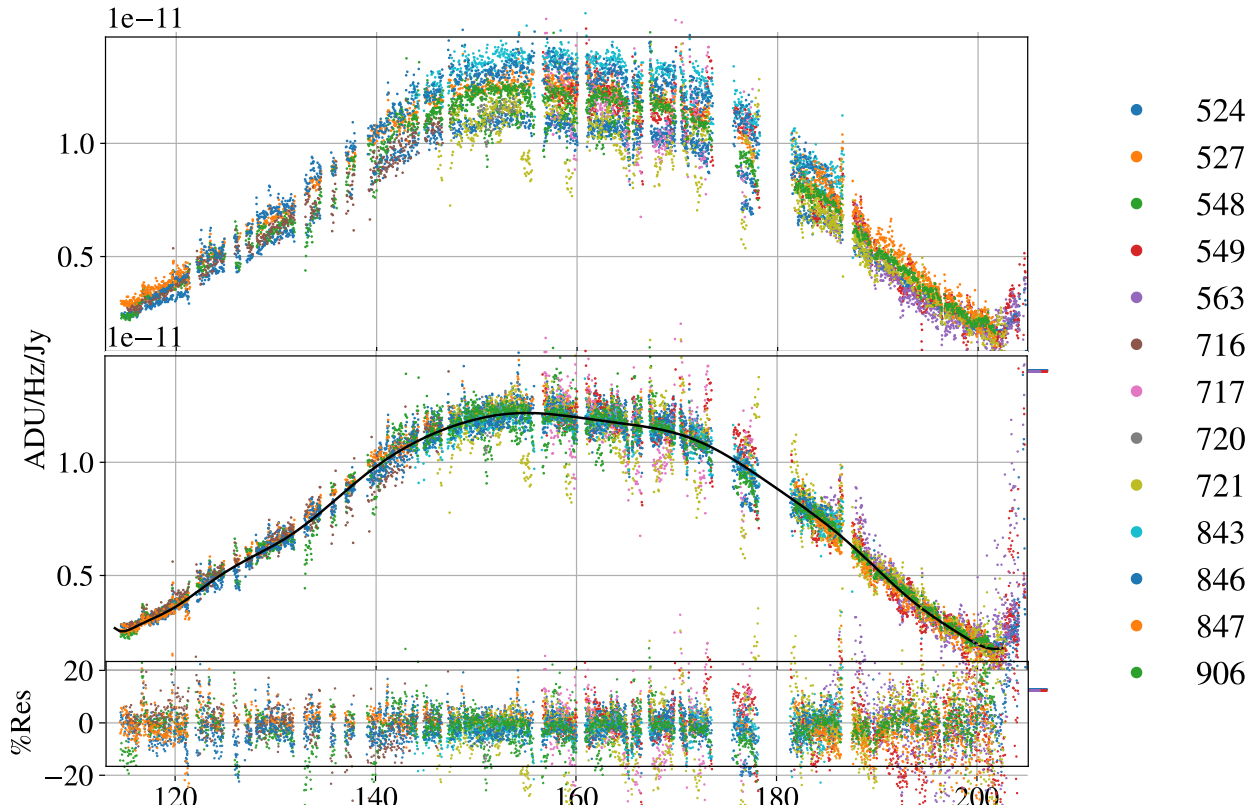


**Figure 21** *Response curves for the red channel.*

[Figure 21](#) shows the different response curves derived for the red channel with data from 2018-2022, i.e., after the filter window change. Each color corresponds to a response curve obtained in a different flight as specified in the legend. The top panel shows the original response curves, while the middle one shows the same curves after scaling them to a common median curve. The response curves obtained in different flights are similar and only differ by multiplicative factors. The scaling factors used to obtain the response curves are reported in the last column of the previous tables.

The fact that the curves obtained in different flights coincide so well after scaling them to a median curve shows that the limiting factor for the accuracy of the flux calibration is the scatter between different flights.

<sup>3</sup> <http://www.lesia.obspm.fr/perso/emmanuel-lellouch/mars/>

<sup>4</sup> [https://github.com/SOFIA-USRA/sofia\\_redux/tree/main/sofia\\_redux/calibration/data/models](https://github.com/SOFIA-USRA/sofia_redux/tree/main/sofia_redux/calibration/data/models)

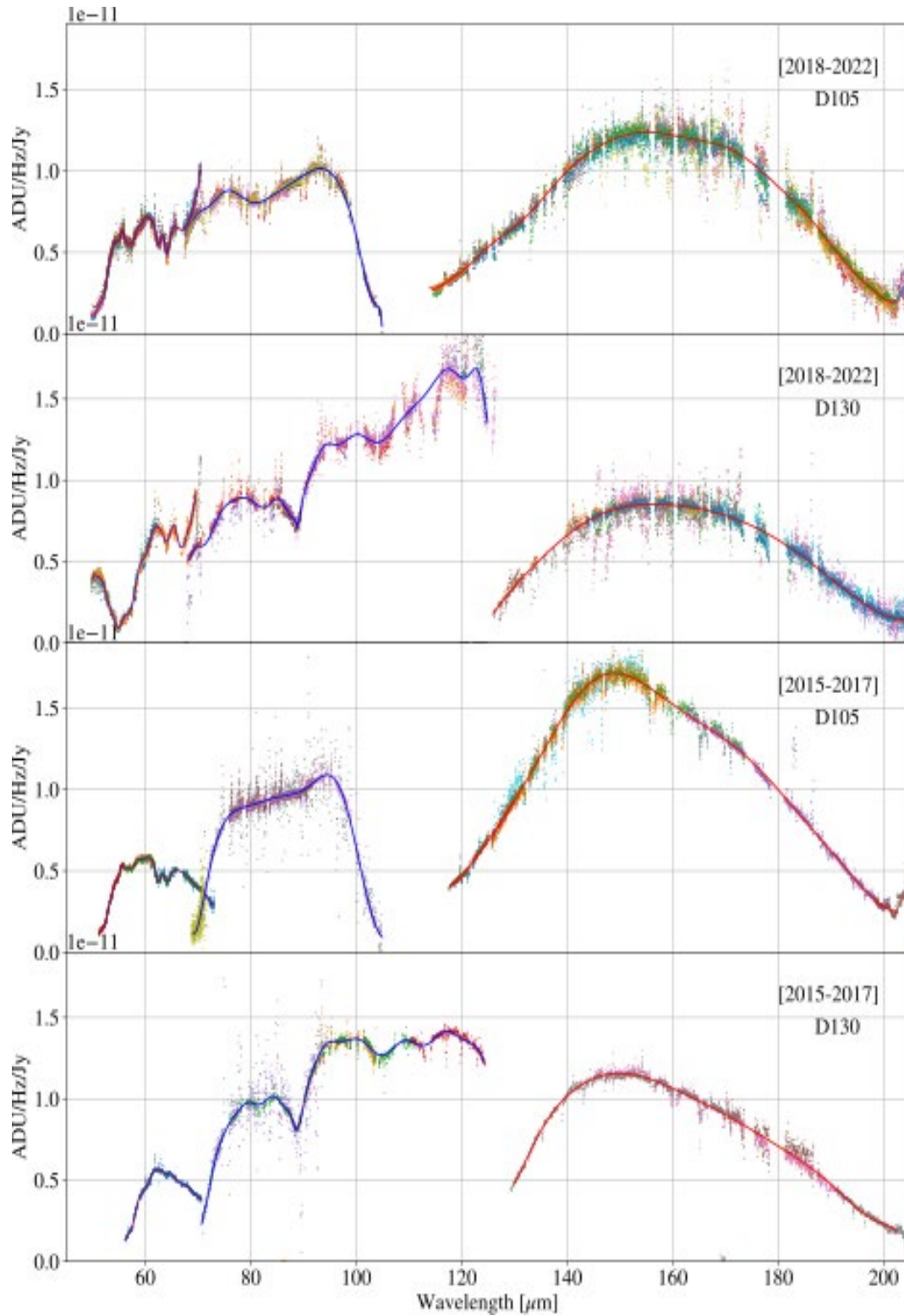


**Figure 22** *All response curves.*



The error in calibration could be reduced by half if calibration curves for each flight had been obtained. Restrictions in the availability of calibrators and the urgency to efficiently use the available science time limited the number of calibrators observed. Moreover, the internal calibrator was usable only in laboratory settings since it was never approved for flights. There was, therefore, no way to calibrate in flux every night of observation. The accuracy in the flux calibration of FIFI-LS is evaluated via the distribution of scaling factors used to match each flight to a common behavior.

The response curves for all the array/orders/dichroics combination in the two epochs (before and after the change of the filter window) are shown [Figure 22](#). Dots with distinct colors correspond to data taken in different flights. The response for the red, blue 1<sup>st</sup>, and 2<sup>nd</sup> orders are shown in red, blue, and purple, respectively. They were obtained by fitting Chebyshev polynomials to the data. In the case of the 1<sup>st</sup> order in the blue, dichroic 130 $\mu$ m, the curves have been fitted with two polynomials to better match the cuspid around 90 $\mu$ m which was due to a dip in the transmission of the 130 $\mu$ m dichroic. For the old filter window, the 1<sup>st</sup> order has more scattered points since calibrators fainter than Mars were used to obtain the response (Calisto and Uranus).

The response curves used until this final release were done in 2019 and had been used to process data until 2021. Since many FIFI-LS papers used these response curves in the analysis, the main variations between the previous and the new release for the main lines observed in the blue and red arrays are discussed here.

Changes are negligible for observations in the red array done after the filter window change (2018-2022). For the old filter, the new response was approximately 9% lower than the previous one with the 130 $\mu$ m dichroic and 6% lower with the 105 $\mu$ m dichroic.

In the case of the blue array, there are differences even with the new filter window. In the case of the old filter window (data pre-2018), the 1<sup>st</sup> order in the blue is 10% and 12% lower than before with the 105 and 130 $\mu$ m dichroics, respectively. For the 2<sup>nd</sup> order the difference is smaller since the new response is 5% lower in the two dichroics.

In the case of the new filter window (data between 2018 and 2022), the effect is similar. The new response was 12% lower than the previous one for the 1<sup>st</sup> order for the two dichroics. For the 2<sup>nd</sup> order the difference was smaller; the new response is 5% and 3% lower than the previous response with the 130 and 105 $\mu$ m dichroics.

#### 3.3 CROSS-CORRELATION OF PACS AND FIFI-LS FLUXES

This section presents the comparison of fluxes of several objects observed with Herschel/PACS and SOFIA/FIFI-LS. Most of the PACS observations considered were done with unchopped spectroscopy since it was impossible to chop in extended emitting regions with Herschel. When comparing these observations to FIFI-LS the PACS data was reprocessed using the transient correction pipeline ([Fadda et al. 2016](#)) and its recent updates in [Sutter & Fadda \(2022b\)](#). As already shown by [Sutter & Fadda \(2022a\)](#) in the case of NGC 7331, the PACS archival data can be significantly off in flux calibration since they are based on the internal calibrators rather than on the more stable telescope background as is the case of normal chop-nod observations. Such calibrators have a response which depends on memory effects of the detectors and can be off by 20% to 90% in an unpredictable way. In one of the cases (NGC 2146), the nucleus of the galaxy was examined and observed at 158 $\mu$ m with PACS in the two modes: chop-nod and unchopped. A

### 3. INSTRUMENT PERFORMANCE

direct comparison of the flux from the central part between the two observations shows that the unchopped flux was 80% higher than the chop-nod flux. The difference virtually disappeared when using the transient-correction pipeline. In this case, the measured flux agrees very well with the flux measured by SOFIA/FIFI-LS as shown in [Figure 23](#). It was also noticed that the astrometry was incorrect by a few arcseconds in a few PACS observations. Before measuring the flux, in the case of NGC 2146 and M 100, the astrometry was corrected by using the WISE channel 4 image to re-center the central peak of the [CII] emission to the nucleus of the galaxies. To obtain the values represented in [Figure 23](#) and [Figure 24](#), the PACS cube was first degraded to the same spatial resolution as the FIFI-LS cube. Then, the flux in several apertures was measured fitting the lines with a pseudo-Voigt profile with the interactive software *sospex* ([Fadda & Chambers 2018](#), see also [Appendix B](#)). In the case of the FIFI-LS blue array, a Gaussian was used to better approximate the line profile. The measurements from the two instruments agree very well inside the errors, except for the nucleus of M 82, which has several FIFI-LS measurements with discordant fluxes, probably taken in flights where the deviation from the median response was very high. The two PACS measurements, the first of them done during the verification phase, are in particularly good agreement. However, the FIFI-LS flux reported in [Figure 23](#) measured on the coaddition of the different flights does not differ significantly from the one measured with PACS.

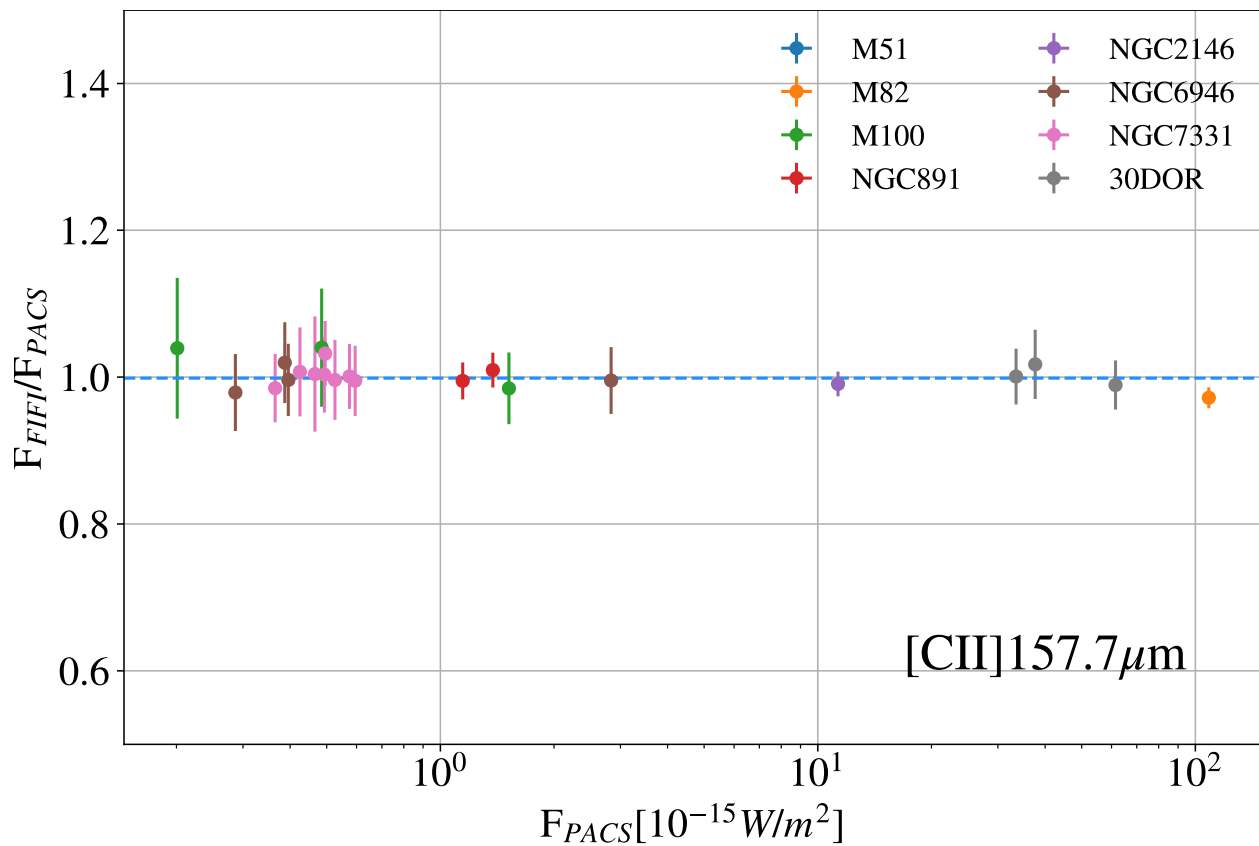


**Figure 23** Comparison of [CII] fluxes measured on the same targets by FIFI-LS and PACS.

The comparison between PACS and FIFI-LS for the blue array is more difficult since the field-of-view of FIFI-LS was much smaller and many parallel observations of [CII] maps have a shallower and sometimes incomplete coverage.

Of the two most intense oxygen lines, the focus is on the [OIII] line at  $88.3\mu\text{m}$  since the [OI] line at  $63.2\mu\text{m}$  is contaminated by a telluric line. Since the quality of the FIFI-LS data is not optimal in the 1<sup>st</sup> order because of the slightly skewed line profile, the scatter of these observations is larger than that of the comparison of [CII] measurements in the red array. Moreover, there are not many regions observed by both instruments with high signal-to-noise ratio. In fact, although many of the extended galaxies observed with PACS in [CII] have parallel data in [OIII], the parallel data are shallower (due to the different field of view) and usually only the nucleus is detected. Only in the case of NGC 6946 have a few deep observations of star forming regions been obtained. Generally, the measurements of PACS and FIFI-LS agree well (Figure 24) with one exception: NGC 253. The observation of NGC 253 was repeated twice with FIFI-LS with comparable results, while the Herschel/PACS observation was done in chopping mode. It is suspected that the discrepancy in flux with the FIFI-LS measurement is due to contamination in the sky position of the PACS observation.

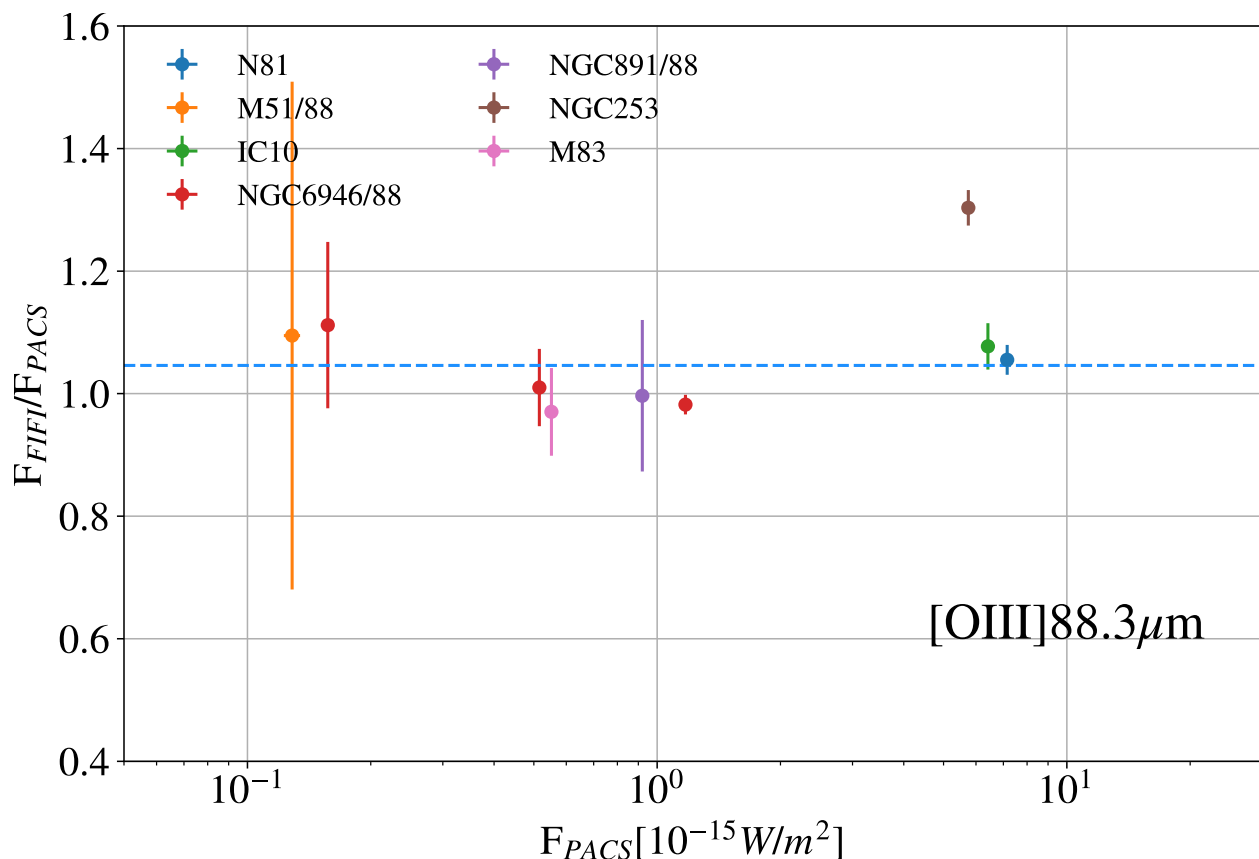


Figure 24 Comparison of [OIII] fluxes of the same targets observed with FIFI-LS and SOFIA



### 3. INSTRUMENT PERFORMANCE

The data considered in the comparison, the apertures, and flux measurements are reported in [Table 8](#).

**Table 7: Targets Used to Compare Fluxes of PACS and FIFI-LS**

Object Name	Line	SOFIA flights	PACS AOR IDs 1342000000+	Apertures				
				#	Center [J2000] [J2000]	r [as]	FIFI-LS [ $10^{15}$ W/m <sup>2</sup> ]	PACS [ $10^{15}$ W/m <sup>2</sup> ]
M51	[CII]	281,282,283, 284,285,287, 380,381,382, 383,384	211188	1	13:29:50.52 +47:11:35.00	10	1.14 ± 0.05	1.16 ± 0.01
				2	13:29:52.33 +47:11:23.24	10	0.85 ± 0.07	0.85 ± 0.01
				3	13:29:55.40 +47:11:45.76	10	1.07 ± 0.03	1.09 ± 0.01
				4	13:29:51.82 +47:11:56.66	10	1.37 ± 0.03	1.37 ± 0.02
				5	13:29:52.68 +47:10:46.90	10	0.43 ± 0.05	0.43 ± 0.01
M82	[CII]	202,280,283, 287,565,566	187205	1	09:55:51.49 +69:40:45.23	20	106 ± 1	109 ± 1
M100	[CII]	572,573, 638,640,663	223733	1	12:22:54.88 +15:49:20.40	11	1.50 ± 0.06	1.52 ± 0.01
				2	12:22:51.60 +15:49:38.42	11	0.50 ± 0.04	0.48 ± 0.01
				3	12:22:48.72 +15:50:04.43	11	0.21 ± 0.02	0.20 ± 0.01
NGC891	[CII]	549,635, 648,639	214874, 214879	1	02:22:36.04 +42:22:10.04	8	1.39 ± 0.02	1.38 ± 0.01
				2	02:22:37.47 +42:22:49.94	8	1.14 ± 0.02	1.15 ± 0.01
NGC2146	[CII]	199,567,568, 571,638	220742	1	06:18:38.33 +78:21:22.21	10	11.2 ± 0.1	11.3 ± 0.1
NGC6946	[CII]	202,203,247, 253,281,284, 285,286	223388	1	20:34:58.15 +60:10:19.21	10	0.28 ± 0.01	0.29 ± 0.01
				2	20:34:52.51 +60:09:14.50	10	2.82 ± 0.04	2.83 ± 0.08
				3	20:34:48.34 +60:08:24.24	10	0.39 ± 0.02	0.39 ± 0.01
				4	20:34:43.97 +60:07:24.79	10	0.39 ± 0.02	0.40 ± 0.01
NGC7331	[CII]	632,634, 640,681	222579	1	22:37:03.60 +34:24:29.94	7.8	0.57 ± 0.02	0.57 ± 0.01
				2	22:37:04.29 +34:24:42.51	7.8	0.43 ± 0.02	0.42 ± 0.01
				3	22:37:05.55 +34:24:41.27	7.8	0.52 ± 0.02	0.53 ± 0.01
				4	22:37:03.94 +34:24:57.45	7.8	0.36 ± 0.01	0.36 ± 0.01
				5	22:37:02.97 +34:24:45.19	7.8	0.51 ± 0.02	0.50 ± 0.01
				6	22:37:04.50 +34:25:11.97	7.8	0.47 ± 0.03	0.47 ± 0.01
				7	22:37:02.68 +34:25:01.07	7.8	0.49 ± 0.02	0.49 ± 0.01
				8	22:37:05.22 +34:24:56.44	7.8	0.59 ± 0.02	0.59 ± 0.00
30DOR	[CII]	310	270358,231283,231282, 222085,222088,222089 222094,231279,231281	1	05:38:49.27 -69:04:43.14	24	60.8 ± 0.4	61 ± 2
				2	05:38:33.06 -69:06:25.19	24	33.5 ± 0.8	33.5 ± 0.5
				3	05:38:59.18 -69:04:06.08	24	38.3 ± 0.9	37.7 ± 0.9
N81	[OIII]	842	253769	1	01:09:12.76 -73:11:39.07	13	7.55 ± 0.15	7.15 ± 0.02
M51	[OIII]	384	211191	1	13:29:50.81 +47:11:56.88	10	0.14 ± 0.05	0.13 ± 0.01
IC10	[OIII]	382	214367	1	00:20:27.84 +59:17:38.30	15	6.9 ± 0.2	6.42 ± 0.02
NGC6946	[OIII]	719	223762	1	20:34:52.40 +60:09:12.89	10	0.52 ± 0.03	0.52 ± 0.01
	[OIII]	721	222248	2	20:35:25.40 +60:09:57.96	12	1.15 ± 0.01	1.17 ± 0.01
	[OIII]	737,803	223377	3	20:35:16.89 +60:10:58.49	5	0.17 ± 0.02	0.16 ± 0.01
NGC891	[OIII]	635,638,639	223762	1	02:22:37.15 +42:22:42.81	20	0.92 ± 0.09	0.92 ± 0.02
NGC253	[OIII]	250,525	199415 <sup>c</sup>	1	00:47:32.99 -25:17:17.43	10	7.5 ± 0.1	5.7 ± 0.05
M83	[OIII]	312,741	223811	1	13:36:53.84 -29:53:06.93	15	0.54 ± 0.03	0.55 ± 0.01

A further comparison was performed in the Large Magellanic Cloud, which was observed with FIFI-LS in OTF mode (Figure 25 and Figure 26). Because this observing mode substantially differs from the standard chop/nod used in most FIFI-LS observations, there was a concern about the reliability of the flux measurements. Fortunately, the brightest regions of the LMC were observed by PACS in the same lines as FIFI-LS ([CII] and [OIII]).

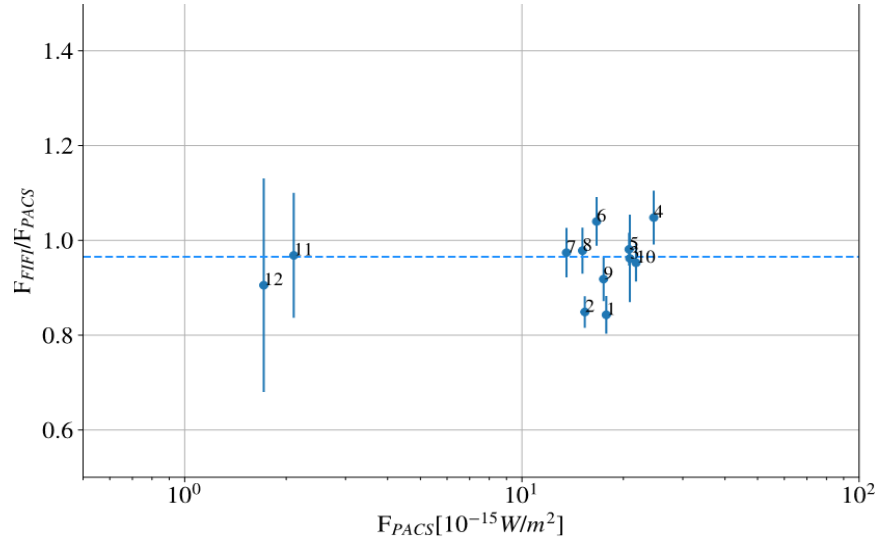


**Figure 25** Comparison of FIFI-LS and PACS fluxes for the [CII] line in several regions of the LMC.

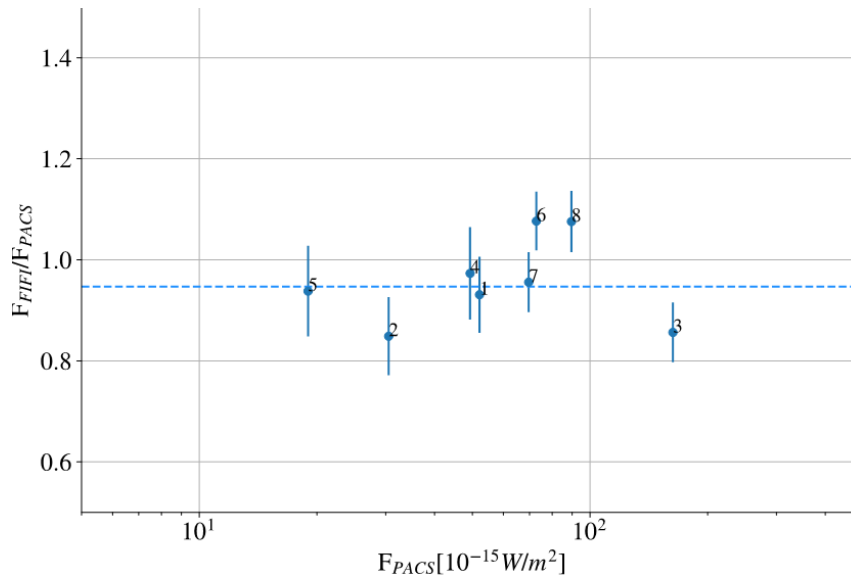


**Figure 26** Comparison of FIFI-LS and PACS fluxes for the [OIII]88 $\mu$ m line in several regions of the LMC.

The [CII] fluxes have a particularly good agreement, and are also the measurements with the highest signal-to-noise ratios. In the case of the [OIII] line, the FIFI-LS observations are shallower than the [CII] ones and the uncertainty on the fluxes is higher. This is reflected in the bigger dispersion of the measurements. Nevertheless, in this case the fluxes measured with FIFI-LS agree very well with the ones measured by PACS.

#### 3.4 SENSITIVITY

The sensitivity of FIFI-LS in the different arrays/orders was computed by estimating the errors in the ramp fitting with observations of the internal calibrator and applying the response curves to these limiting fluxes.

In the case of the minimum detectable continuum flux, the flux which is observed after coadding the 16 pixels of each spaxel, or spatial module was considered. The limiting factor for detection was the dispersion of the ramp fits ( $\sigma_r$ ). Since each series of ramps had an exposure time  $t_{exp}$ , considering a total integration time of 900s and a  $4\sigma$  detection, the minimum continuum flux detected is:

$$MDCF(\lambda)[Jy] = \frac{4\sigma_r(\lambda) \sqrt{\frac{t_{exp}}{900}}}{\sqrt{16} \rho(\lambda)} = \frac{\sigma_r(\lambda)[ADU/Hz] \sqrt{t_{exp}[S]}}{30\rho(\lambda)[ADU/Hz/Jy]},$$

where  $\rho(\lambda)$  is the response of the instrument at the wavelength  $\lambda$ .

To compute the minimum detectable line flux, in the case of an unresolved line, the number of pixels involved in detecting the flux must be considered. In practice, the optimal interval which allows the highest signal-to-noise ratio to detect the line must be considered. Assume a line with a Gaussian profile, which is a good approximation in the case of FIFI-LS:

$$F(\lambda) = \frac{F_0}{\sqrt{2\pi}\sigma} e^{-\frac{(\lambda-\lambda_0)^2}{2\sigma^2}}.$$

By integrating the line inside the wavelength interval of size  $2L$ , the following signal-to-noise ratio can be obtained:

$$\begin{aligned} S/N &= \frac{\frac{1}{\sqrt{2\pi}\sigma} \int_{\lambda_0-L}^{\lambda_0+L} F_0 e^{-(\lambda-\lambda_0)^2/(2\sigma^2)} d\lambda}{\sqrt{\frac{2L}{\delta_{pix}} \sigma_{pix}(\lambda) \delta_{pix}}} \\ &= \frac{\frac{1}{\sqrt{2\pi}\sigma} 2 \int_0^L F_0 e^{-\lambda^2/(2\sigma^2)} d\lambda}{\sqrt{\frac{2L}{\delta_{pix}} \sigma_{pix}(\lambda) \delta_{pix}}} \\ &= \frac{F_0}{\sqrt{\frac{2\sqrt{2}\sigma}{\delta_{pix}} \sigma_{pix}(\lambda) \delta_{pix}}} \frac{erf\left(\frac{L}{\sigma\sqrt{2}}\right)}{\sqrt{\frac{L}{\sigma\sqrt{2}}}} \end{aligned}$$

where  $erf(z) = \frac{2}{\sqrt{\pi}} \int_0^z e^{-t^2} dt$ , and in the denominator, there is the number of pixels in the interval  $2L/\delta_{pix}$ , with  $\delta_{pix}$  the size of the pixel in wavelength and  $\sigma_{pix}$  the noise in the single spectral pixel

measured on ramps. The noise is multiplied by the width of the pixel to get the integrated flux in the pixel.

The function to maximize is  $erf(x)/\sqrt{(x)}$  which has a maximum at  $x = \frac{L}{\sqrt{2}\sigma} \approx 1$ , which means an interval of  $2\sqrt{2}\sigma$ . Inside this interval, 84% of the total flux is detected.

The S/N in the optimal aperture is therefore:

$$S/N = \frac{F_{ap}}{\sqrt{\frac{2\sqrt{2}\sigma}{\delta_{pix}} \sigma_{pix}(\lambda) \delta_{pix}}}$$

Now, since the spectral resolution is defined as:  $R = \frac{\lambda}{FWHM}$ , assuming a Gaussian line of scale  $\sigma$ , since  $FWHM = 2\sqrt{2 \ln 2} \sigma$ , this means:  $\sigma = \frac{\lambda}{2\sqrt{2 \ln 2} R}$ . Therefore, the optimal interval to measure the flux of the line is:  $\Delta\lambda = 2\sqrt{2}\sigma = \frac{\lambda}{\sqrt{\ln 2} R}$ . So, the number of pixels in the optimal interval is:  $N_{pix} = \frac{\lambda}{\sqrt{\ln 2} R \delta_{pix}}$ , where  $\delta_{pix}$  is the spectral width of a pixel.

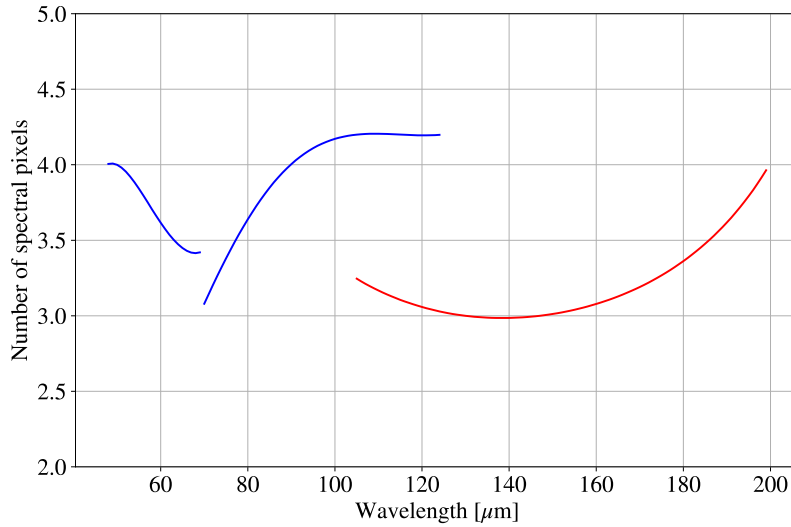


**Figure 27** *Optimal number of spectral pixels to integrate.*

Figure 27 shows that the number of pixels corresponding to the interval for optimal detection is between 3 and 4. At this point, the flux measured at a certain S/N by inverting the previous equation can be computed:

$$F_{ap} = S/N \sqrt{\frac{2\sqrt{2}\sigma}{\delta_{pix}}} \sigma_{pix}(\lambda) \delta_{pix}$$

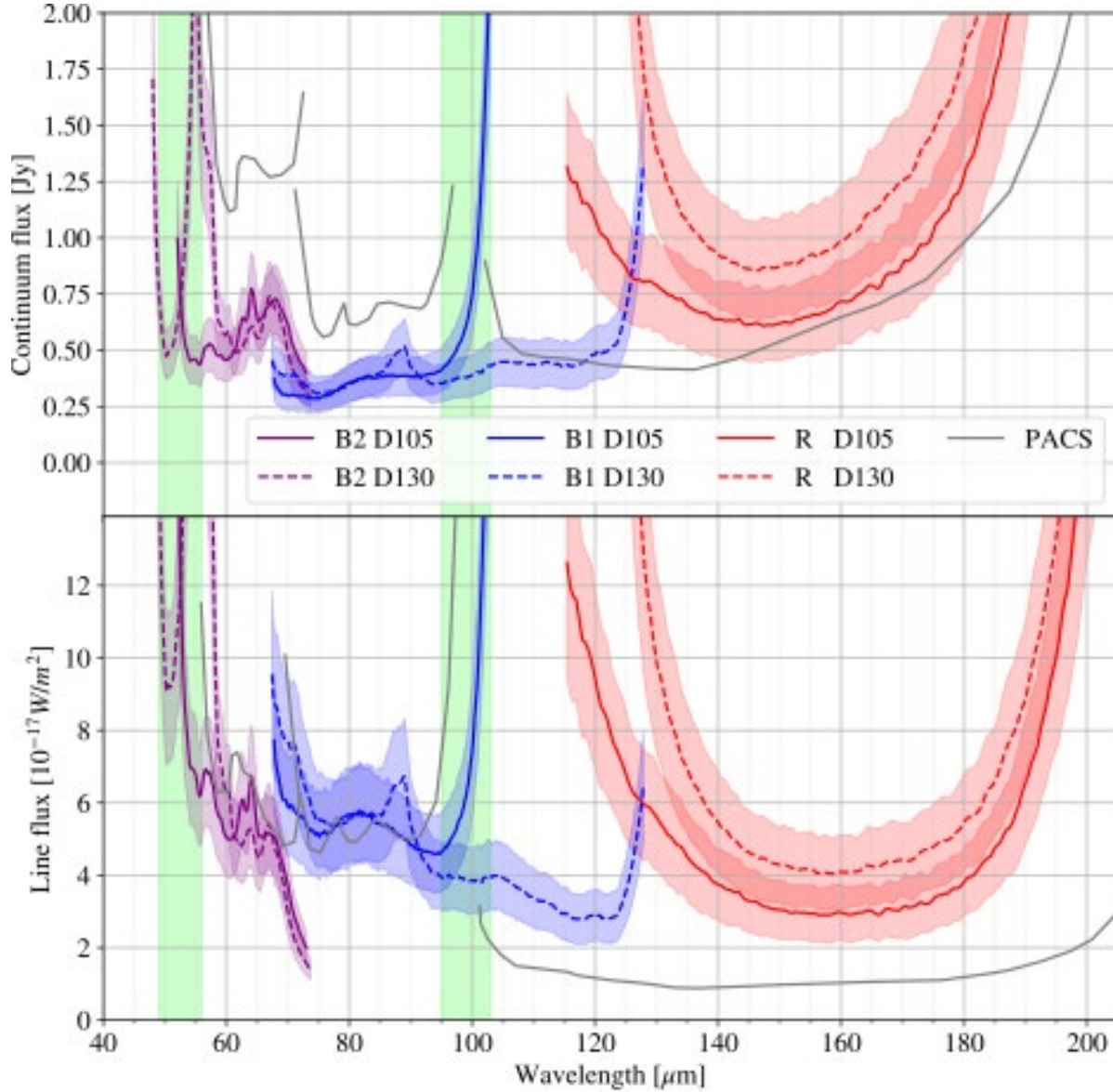


**Figure 28** Minimum detectable line flux (MDLF); The top panel shows the continuum limiting sensitivity. The band around the curve shows the error of the estimation. The bottom panel shows the line flux limiting sensitivity.

By substituting  $\sigma$  with  $\frac{\lambda}{2\sqrt{2}\ln 2R}$  and  $\sigma_{pix}(\lambda)$  with  $\sigma_{pix}(v) \frac{c}{\lambda^2}$  and using  $S/N = 4$ , the following is obtained:

$$MDLF[10^{-17}W/m^2] = 4 \sqrt{\frac{\delta_{pix}}{R\sqrt{\ln 2}} \frac{\sigma_{pix}(v)[Jy] c[km/s]}{\lambda^{3/2}[\mu m]}}$$

Figure 28 shows the curves for the three different bands covered by FIFI-LS (red, blue in 1<sup>st</sup>, and 2<sup>nd</sup> order) and the two possible dichroics. The solid curves correspond to the 105 $\mu$ m dichroic, while the dashed ones correspond to the 130 $\mu$ m dichroic. The shaded bands are the error bands for the estimated curves.

In the figure, the green bands mark the regions of the spectrum which were not observable with PACS on Herschel. In particular, the upgrade of the filter window in 2018 made possible the observation of the important line of [OIII] at 51.81 $\mu$ m. Depending on the redshift of the object, this line was observed with the dichroic which had the best sensitivity (130  $\mu$ m at low redshift, 105  $\mu$ m for targets with  $cz > 4500$  km/s).

For comparison the sensitivity of the PACS instrument on Herschel is also plotted with grey lines. This sensitivity was similar to FIFI-LS, but was operating from space with a slightly bigger telescope.

The main difference between the two instruments is in the blue array, since PACS was using the 2<sup>nd</sup> order of the grating while FIFI-LS used the 1<sup>st</sup> order of a dedicated grating. Moreover, PACS had the same pixel size for the two arrays, while FIFI-LS had pixels of 6" and 12" size for the blue and red array, respectively. Because of these reasons, the line sensitivity in the blue is only slightly worse for FIFI-LS, while PACS is much more sensitive in the red.

Although the sensitivity is similar, it should be stressed that the observations with FIFI-LS were affected by the atmospheric transmission and telluric features which sometimes made the observations rather challenging and the real sensitivity worse than what was estimated from the noise in the ramps.

### 3.5 COMPARISON WITH PACS SPECTROSCOPY

#### 3.5.1 FIFI-LS and PACS Observation Modes

The design of FIFI-LS was analogous to the design of the Herschel/PACS instrument as both instruments were designed almost in parallel at the same institute (MPE Garching) under the same PI (A. Poglitsch). The detectors of both instruments were essentially the same (two 16x25 Ge:Ga arrays), and the optical design was similar (same sized gratings in Littrow configuration, same IFU). The difference is that FIFI-LS didn't need to be as compact and featured two grating spectrometers, while the PACS spectrometer had only one. The two gratings made it possible to observe two different wavelengths simultaneously and independent of each other (one in each channel), significantly increasing observing efficiency. This was particularly advantageous for mapping large areas in several lines. This design also allowed different pixel sizes (6 arcsec and 12 arcsec) in each spectrometer, which meant a better match to the beam size. On the other hand, the PACS spectrometer had a pixel size of 9.4 arcsec which was good at longer wavelengths, but noticeably under-sampled the telescope PSF at shorter wavelengths. Furthermore, the blue channel of FIFI-LS allowed observations down to 51  $\mu$ m (by using the blue grating in 2<sup>nd</sup> order), while PACS could not routinely observe the [OIII] 52  $\mu$ m line.

The spectral resolution of the two instruments is comparable, but the execution time per observation and the sensitivities differ. The "raw" sensitivity (point source, unresolved spectral line) of Herschel/PACS was about eight times better than that of SOFIA/FIFI-LS, owing to the lower telescope temperature and emissivity, the lack of atmospheric emission and absorption, and the larger telescope diameter. The fundamental building block of a PACS observation took ~7



minutes to complete, after which the noise in a line detection was  $\sim 3 \times 10^{-18}$  W/m<sup>2</sup>. For deep observations, this was a useful building block, of which several repetitions could be executed to reach the desired depth (SNR). However, for (fully sampled) mapping of sufficiently bright, large objects (e.g., nearby galaxies), this led to exceptionally long integration times and highly “over-integrated” line-detections (e.g., SNR>100), which were then limited by systematic effects and calibration precision. Here SOFIA/FIFI-LS had an advantage, since the telescope time to move from pointing to pointing on the sky was only  $\sim 8$  sec on average. This enabled fast mapping of relatively bright sources. In the symmetric chop mode, the minimum on-source integration time typically used with FIFI-LS was 30 s, with a total wall-clock time of  $\sim 75$  sec (for one nod pair plus associated telescope moves).

#### 3.5.2 Flux Fraction in the Central Spaxel

When comparing the two similar instruments FIFI-LS and PACS on Herschel, it is important to remember that they had different spatial resolutions and sky pixel sizes. The spaxel size of FIFI-LS was set to capture most of the flux of a point source, since they are comparable to the FWHM of the point spread function. It is nevertheless important to realize that a spaxel will not capture all the flux of a point source, but will lose some fraction of it depending on the wavelength where it is detected.

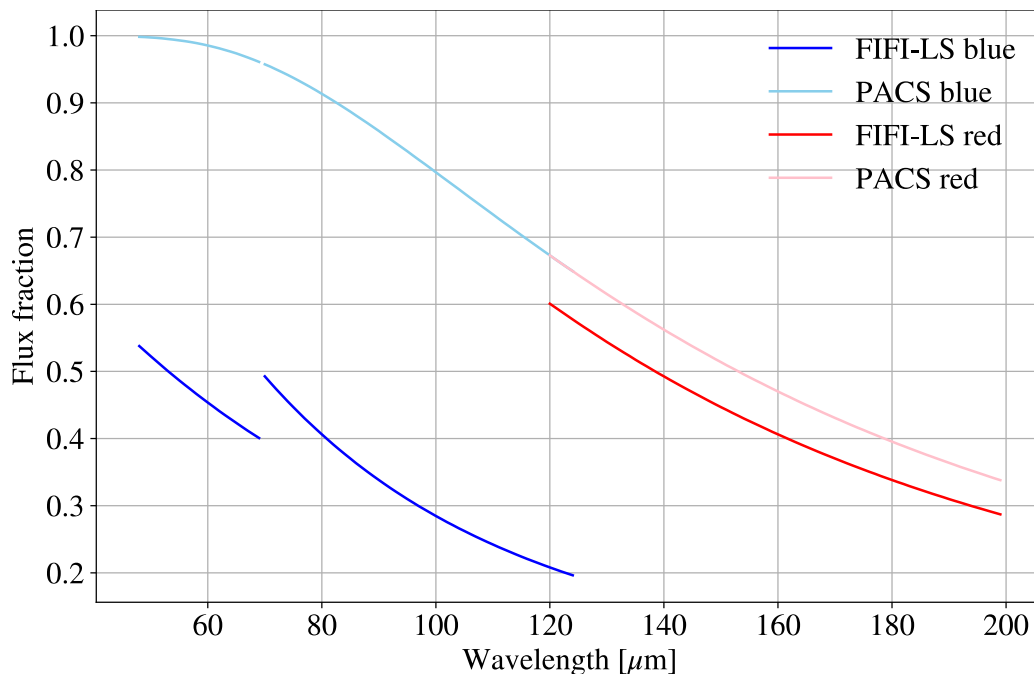


Figure 29 Flux fraction in the central pixel.

Figure 29 shows how the fraction of flux in the central pixels varied in the two detectors (red and blue) at different wavelengths, assuming that the source was centered on the spaxel. The curves for PACS on Herschel are shown for comparison. While for the red array they are almost equivalent since the better spatial resolution of PACS compensated for its smaller pixel, in the case of the blue array, FIFI-LS intercepted less flux since it used a much smaller spaxel better adjusted

### 3. INSTRUMENT PERFORMANCE

---

to the PSF in the blue, while PACS used the same spaxel size for the two arrays, therefore intercepting the almost totality of the flux in the blue.

### 4. DATA

This section describes the data reduction pipeline and how to use it as well as detailed information on the FIFI-LS data products from the raw data files to the final processed Level 4 files. In addition, considerations on how to account for SOFIA- and instrument-specific effects on the data, such as telluric corrections and instrumental artifacts, are discussed.

#### 4.1 PIPELINE SOFTWARE

The FIFI-LS pipeline is written entirely in Python. The pipeline is platform independent but has been tested only on Linux and Mac OS X operating systems. Running the pipeline requires a minimum of 16GB RAM, or equivalent-sized swap file.

The pipeline is primarily composed of four modules within the `sofia_redux` package:

- `sofia_redux.instruments.fifi_ls`
- `sofia_redux.pipeline`
- `sofia_redux.spectroscopy`
- `sofia_redux.toolkit`

More optional features are provided by the `sofia_redux.calibration` and `sofia_redux.scan` modules.

The `fifi_ls` module provides the data processing algorithms, with supporting libraries from the `toolkit` and `spectroscopy` modules. The `pipeline` module provides interactive and batch interfaces to the pipeline algorithms. The `calibration` module is used to provide interactive photometry routines in the interactive interface. The `scan` module provides support for more processing tasks specific to on-the-fly mapping modes.

##### 4.1.1 External Requirements

To run the pipeline for any mode, Python 3.8 or higher is needed, as well as the following packages: `numpy`, `scipy`, `matplotlib`, `pandas`, `astropy`, `configobj`, `numba`, `bottleneck`, `joblib`, and `astropy-helpers`. Some display functions for the graphical user interface (GUI) additionally require the `PyQt5`, `pyds9`, `photutils`, and `dill` packages. All required external packages are available to install via the `pip` or `conda` package managers. See the Anaconda environment file (`environment.yml`), or the `pip` requirements file (`requirements.txt`) distributed with `sofia_redux` for specific version requirements.

Running the pipeline interactively also requires an installation of SAO DS9 for FITS image display. See <http://ds9.si.edu/> for download and installation instructions. The DS9 executable must be available in the `PATH` environment variable for the `pyds9` interface to be able to find and control it.

##### 4.1.2 Source Code Installation

The source code for the FIFI-LS pipeline supported by the SOFIA Data Processing Systems (DPS) team can be obtained directly from the external GitHub repository. This repository contains all the

configuration files needed, auxiliary files, and Python code to run the pipeline on FIFI-LS data in any observation mode.

After obtaining the source code, install the four Python libraries with the command:

```
$ python setup.py install
```

from the top-level directory. Alternatively, a development installation may be performed from inside the directory with the command:

```
$ pip install -e .
```

After installation, the top-level pipeline interface commands should be available in the PATH.

Typing:

```
$ redux
```

from the command line should launch the GUI interface, and

```
$ redux_pipe -h
```

should display a brief help message for the command line interface.

### 4.1.3 Configuration

For FIFI-LS algorithms, default parameter values are defined by the Redux object that interfaces to them. These values may be overridden manually for each step, while running in interactive mode. They may also be overridden by an input parameter file, in INI format, in either interactive or automatic mode. See Appendix [D](#) for an example of an input parameter file, which contains the current defaults for all parameters.

Requirements for input header keywords are also specified in a configuration file, called *headerdef.dat*, found in the *fifi\_ls/data* package directory. This table lists the keyword name, whether it is a value required to be present in the input headers, its default value, the data type of the value, and any requirements on the value range (minimum value, maximum value, or enumerated value). The table also defines how keywords from multiple input files should be combined for a single output file (e.g., take the first value, take the sum, string-concatenate, etc.). A sample of this configuration file is also given in Appendix [D](#). All keywords present in the table will be written to output files produced by the FIFI-LS Redux pipeline.

## 4.2 INPUT DATA

Redux takes as input raw FIFI-LS FITS data files, which contain unsigned tables. The number of frames per raw data cube depends on the readout mode used to acquire the data. The FITS headers contain data acquisition and observation parameters and, combined with the pipeline configuration files, include the information necessary to complete all steps of the data reduction process. Some critical keywords must be present in the raw data to perform a successful grouping, reduction, and ingestion into the SOFIA archive (see Appendix [D](#)).

It is assumed that the input data have been successfully grouped before beginning reduction: Redux considers all input files in a reduction to be science files that are part of a single homogeneous reduction group, to be reduced together with the same parameters.

### 4.2.1 Auxiliary Files

To complete a standard reduction, the pipeline requires several auxiliary files to be on disk, in standard locations within the *fifi\_ls/data* package directory. These files may be overridden in custom reductions, using input parameters for the relevant pipeline steps. See [Table 9](#) for a list of all commonly used types of auxiliary files.

**Table 8: Auxiliary Files Used by FIFI-LS Reductions**

Auxiliary File	File Type	Pipeline Step	Contents
<b>Bad Pixel</b>	ASCII	Fit ramps	List of known bad pixels
<b>Wavelength Calibration</b>	CSV	Lambda calibrate	Wavelength calibration constants, by date
<b>Spatial Calibration</b>	ASCII	Spatial calibrate	Spaxel position values, by date
<b>Spatial Flat</b>	ASCII	Apply flat	Flat correction values for all 25 spaxels, by date
<b>Spectral Flat</b>	FITS	Apply flat	Flat correction values for all spaxels at all possible wavelengths
<b>Resolution</b>	ASCII	Telluric correct, Resample	Expected spatial and spectral resolutions for all modes
<b>ATRAN</b>	FITS	Telluric correct	An unsmoothed atmospheric transmission model spectrum
<b>Response</b>	FITS	Flux calibrate	An instrumental response spectrum

### 4.3 DATA FORMAT

All files produced by the pipeline are multi-extension FITS files, for which the primary HDU contains only the primary header, and all data are contained in separate extensions.

For standard chop/nod modes, all output extensions are FITS image extensions. Pipeline steps prior to the Combine Scans step output one extension of each type for each of  $N_{\text{scan}}$  grating scans performed. Intermediate flux and error data for all steps after the Fit Ramps step are 2D arrays (spaxel  $\times$  spaxel); the final product contains 3D spectral cubes (RA  $\times$  Dec  $\times$  wavelength).

For the OTF mode, intermediate data files produced by pipeline steps prior to the Spatial Calibrate step additionally contain a binary table holding sky position data for each scan position (extension SCANPOS\_G0). Intermediate flux and error data in this mode are 3D cubes (spaxel  $\times$  spaxel  $\times$  scan position). The final product is identical to other modes.

#### 4.4 REDUCTION PROCEDURE

This section describes each of the data reduction pipeline steps in detail. However, as a general overview, the pipeline performs the following steps:

1. Reformat the data
  - Split grating and chop
  - Fit ramps
2. Demodulate
  - Subtract chops
  - Combine nods
3. Correct instrumental coordinates and response
  - Wavelength calibrate
  - Spatial calibrate
  - Apply flat
  - Combine grating scans
4. Calibrate to physical units
  - Telluric correct
  - Flux calibrate
  - Wavelength shift
5. Resample onto a regular grid
  - Resample in spatial and spectral dimensions

##### 4.4.1 Split Grating Chop

A single FIFI-LS raw FITS file contains the data from both chop positions (on and off) for each grating step used in a single nod position. FIFI-LS recorded its grating positions in “inductosyn” units. These are long integer values from the grating mechanism and are later used to convert the data to a micron scale in the wavelength calibrate step.

The raw FIFI-LS data consists of a header (metadata describing the observation) and a table of voltage readings from the detector pixels. Each data section contains one frame, i.e., simultaneous readouts of all detector pixels and grating values.

The detectors were read out with integrating amplifiers: at each pixel, a current proportional to the incident flux charged a capacitor. The resulting voltage was sampled at about 256Hz. After a certain number of read-outs (the ramp length), the capacitors were reset to prevent saturation. Thus, the data consists of linearly rising ramps for which the slope is proportional to the flux. See [Figure 30](#) for an illustration of the read-out sequence.



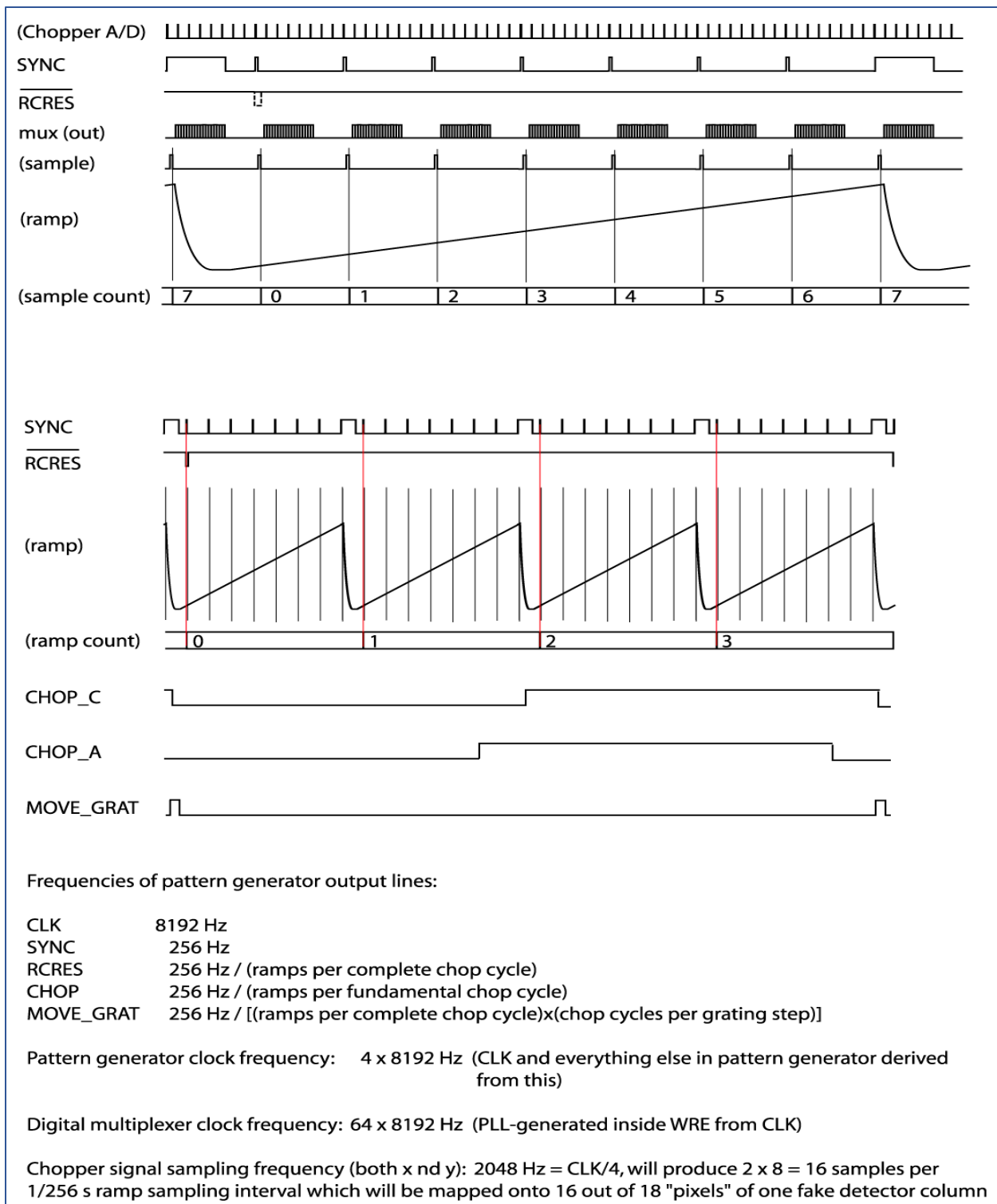


Figure 30 FIFI-LS timing and readout diagram.

A header was sent before each frame. The header consisted of the following eight unsigned 16-bit words.

- Word 0: The word #8000 marks the start of the header.
- Word 1: The low word of the 32-bit frame counter.
- Word 2: The high word of the 32-bit frame counter.
- Word 3: The flag word. Bit 0 is the chopper signal. Bit 1 is the detector (0=red, 1=blue). Unused bits are fixed to 1 to recognize this flag word.
- Word 4: The sample count as defined in the timing diagrams (see [Figure 30](#)). This count gets advanced at every sync pulse and reset at every long sync pulse.
- Word 5: The ramp count as defined in the timing diagrams. This counter gets advanced with a long sync pulse and reset by RCRES.
- Word 6: The scan index
- Word 7: A spare word (for now used as “end of header”: #7FFF).

Only columns 3, 4, and 5 are used in the split grating/chop step. The following shows example header values for a raw RED FIFI-LS file:

								columns:									
		0	1	2	3	4	5	6			7						
-----																	
32768	28160	15	1	0	0	89	32767										
32768	28161	15	1	1	0	89	32767										
32768	28162	15	1	2	0	89	32767										
32768	28163	15	1	3	0	89	32767										
32768	28164	15	1	4	0	89	32767										
32768	28165	15	1	5	0	89	32767										
32768	28166	15	1	6	0	89	32767										
32768	28167	15	1	7	0	89	32767										
32768	28168	15	1	8	0	89	32767										
32768	28169	15	1	9	0	89	32767										
32768	28170	15	1	10	0	89	32767										
32768	28171	15	1	11	0	89	32767										
...																	

Column 3 is all ones, showing that the data is for the RED channel, column 4 counts the readouts from 0 to 31, and column 5 shows the ramp number.

The keywords for each chop and grating position starts and stops in the raw data table are found using the header keywords RAMPLN\_[B,R], C\_CYC\_[B,R], C\_CHOPLN, G\_PSDN\_[B,R], G\_PSDN\_[B,R] keywords. A RED data example is as follows:

RAMPLN\_R= 32 / number of readouts per red ramp  
C\_CHOPLN= 64 / number of readouts per chop position  
G\_PSUP\_R= 5 / number of grating positions up in one cycle  
G\_PSDN\_R= 0 / number of grating positions down in one cycle

Here, C\_CHOPLN / RAMPLN\_R is 64 / 32 = 2; therefore, there are 2 ramps per chop.

Each chop switch index is determined using the 5<sup>th</sup> column in the header. It is chop 0 if the value is odd and chop 1 if the value is even. Grating scan information determines how that chop phase is split up into separate extensions using the following formula:

$$\text{binsize} = (\text{nreadout} \times \text{ramplength}) / (\text{nstep} \times \text{choplengh})$$

where *nreadout* is the total number of readouts (frames) in the file, *ramplength* is determined by the appropriate RAM- PLN keyword, *nstep* is the number of grating steps (G\_PSDN + G\_PSUP), and *choplengh* is the number of readouts per chop position (C\_CHOPLN).

The binary data section is comprised of 468 signed 16-bit words: one each for 25 spaxels, plus one control value, times 18 total spectral channels (“spexels”). Data is read one spectral channel at a time. Spectral channel zero of all 25 pixels is read out, and then a grating value (analog readout from the grating mechanism, in this case “inductosyn” units) is recorded; then the next channel of all the pixels is read out, and then the next grating value, and so on, through all the spectral channels. The grating values may be checked during pipeline processing to discard samples with inconsistent grating positions. Of the 18 spectral channels, channel 0 is the CRE resistor row and row 17 is the empty CRE row (“dummy channel”). The empty row may be used during processing to help remove correlated noise from a spaxel. These two channels are then discarded; the other 16 channels are considered valid spexels.

The first step in the data reduction pipeline is to split out the data from each grating scan position into separate FITS image extensions, and to save all grating positions from a single chop position into a common file. For example, if there are five grating scans per chop, and two chop positions, then a single one-extension input raw FITS file will be reorganized into two files (chop 0 and chop 1) with five extensions each. For total power mode, there is only one chop position, so there will be one output file, with one extension for each grating step. Each extension in the output FITS files contains the data array corresponding to the grating position recorded in its header (keyword INDPOS). Hereafter, in the pipeline, until the Combine Grating Scans step, each grating scan is handled separately.

For OTF mode data, an additional binary table is attached to the FITS file, recording the telescope position at each readout sample. These positions are calculated from the telescope speed keywords in the FITS header (OBSLAMV and OBSBETV, for RA and Dec speeds in arcsec/s, respectively). Readouts taken before and after the telescope scanning motion are also identified using the OTFSTART and TRK\_DRTN header keywords. These readouts are flagged in the SCANPOS table for removal from consideration in later pipeline steps.

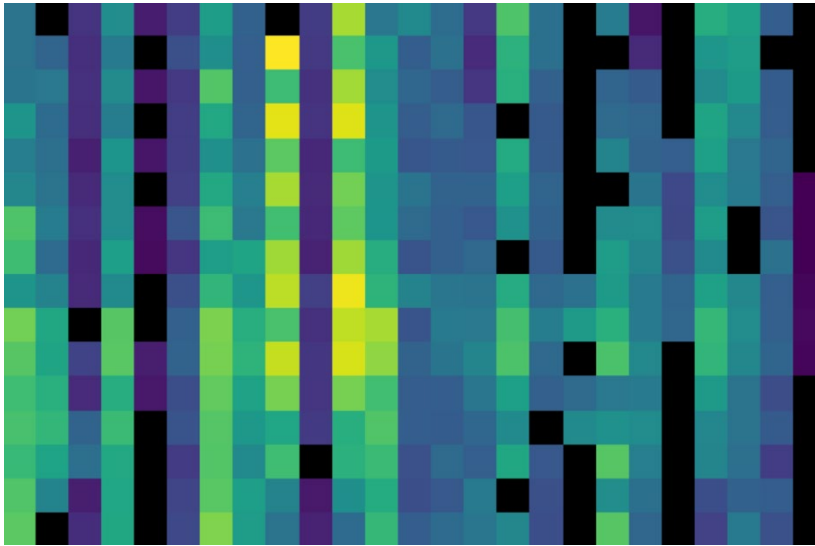


**Figure 31** *The flux array from a single grating scan in the RED channel, at the chop 0 position in nod A after fitting ramps, flattened into a 25 x 16 array. The spectral dimension runs along the y-axis. The data was taken in symmetric chopping mode.*

#### 4.4.2 Fit Ramps

The flux measured in each spatial and spectral pixel is reconstructed from the readout frames by fitting a line to the voltage ramps. The slope of the line corresponds to the flux value.

Before fitting a line to a ramp, some likely bad frames are removed from the data. The grating values (in the 26th spaxel position), the first ramp from each spaxel, the first 2-3 readouts per ramp, and the last readout per ramp are all removed before fitting. Optionally, the flux in the first (empty) spectral pixel may be subtracted from all other pixels in its associated spaxel, as a correction for detector readout bias. The dummy channels in the first and last spectral pixels are then removed from the flux array; they are not propagated through the rest of the pipeline.

Additionally, the grating values in the spare spaxel may be used to identify ramps for which the grating deviated from the expected position. The grating values are averaged over a ramp and compared to the expected value. If they do not fall within a threshold of the expected position, the ramp is flagged for rejection.

A ramp may be marked as saturated if it does not have its largest value in the last readout of the ramp. If this occurs, the readout before the largest value along with any readouts after it are removed before fitting. This ensures that the slope is not contaminated by any non-linearity near the saturation point.

Typically, multiple ramps are taken at each chop position. After the slope of each ramp is derived, the slopes are combined with a robust weighted mean. This final averaged value is recorded as the flux for the pixel and the error on the mean is recorded as the error on the flux for that pixel. After this pipeline step, there is a flux value for each spatial and spectral pixel, recorded in a  $25 \times 16$  data array in a separate FITS image extension for each grating scan. The error values are recorded in a separate  $25 \times 16$  array, in another FITS image extension (Figure 31). The extensions are named with a suffix indicating the grating scan number. For example, for two grating scans, the output will have extensions FLUX\_G0, STDDEV\_G0, FLUX\_G1, and STDDEV\_G1.

For OTF data, each ramp represents a different sky position, so separate ramps are not averaged together, but are propagated through the pipeline as a data cube. The flux and error data arrays have dimension  $25 \times 16 \times N_{\text{ramp}}$ , where  $N_{\text{ramp}}$  is the number of ramps for which the telescope motion was nominal. In the SCANPOS table attached to the FITS file, the telescope positions for each ramp are calculated from an average over the positions for the readouts in the ramp and propagated forward for later use in spatial calibration.

Some pixels in the data array may be set to not-a-number (NaN). These are either known bad detector pixels, or pixels for which the ramp fits did not have sufficient signal-to-noise. These pixels will be ignored in all further reduction steps.

### 4.4.3 Subtract Chops

To remove instrument and sky background emission, the data from the two chop positions must be subtracted. For A nods in symmetric mode, chop 1 is subtracted from chop 0. For B nods in symmetric mode, chop 0 is subtracted from chop 1. All resulting source flux in the symmetric chop-subtracted data should therefore be positive, so that the nods are combined only by addition (see [Figure 32](#)). In asymmetric mode, chop 1 is subtracted from chop 0 regardless of nod position.

This pipeline step produces one output file for each pair of input chop files. In total power mode, no chop subtraction is performed.

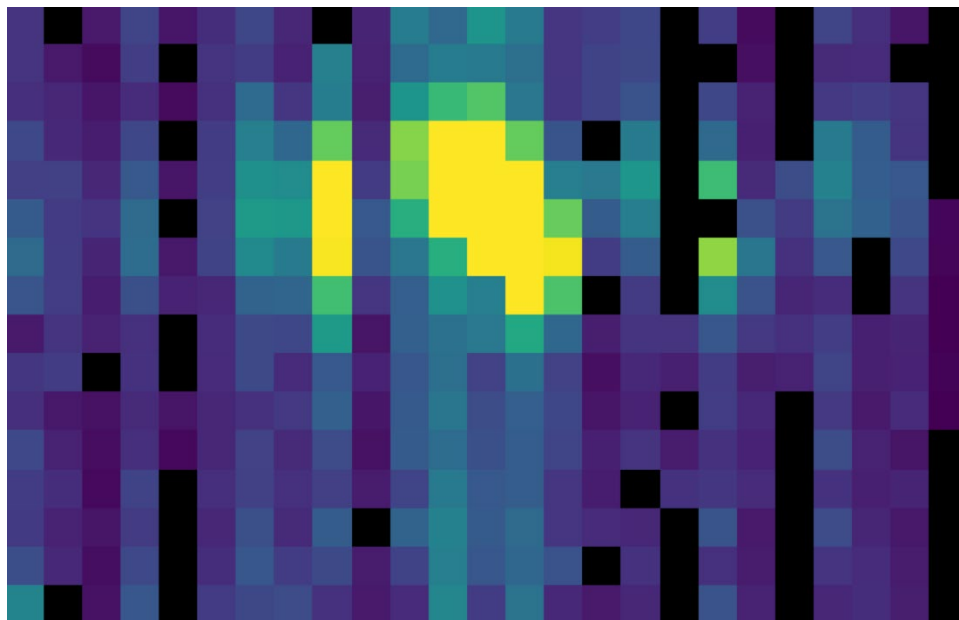


**Figure 32** *The same flux array as in Figure 31, with the corresponding chop 1 subtracted.*

### 4.4.4 Combine Nods

After the chops are subtracted, the nods must be combined to remove residual background. In symmetric chopping mode, the A nods are paired to adjacent B nods. To match a given A nod, a B nod must have been taken at the same dither position (FITS header keywords DLAM\_MAP and DBET\_MAP), and with the same grating position (INDPOS). The B nod meeting these conditions

and taken nearest in time to the A nod (keyword DATE-OBS) is added to the A nod. In asymmetric mode, a single B nod may be subtracted from multiple A nods. For example, in an AAB pattern the B nod is combined with each preceding A nod. The B nods in this mode need not have been taken at the same dither position as the A nods, but the grating position must still match. The matching B nod taken nearest in time is subtracted from each A nod. Optionally, in asymmetric mode, the nearest B nods before and after the A nod may be combined before subtracting from the A nod, either by averaging them, or by linearly interpolating their values to the time of the A nod observation. In some cases, this may reduce background artifacts resulting from changes in the sky background between the A and B nod observations.

This pipeline step produces an output file for each input A nod file, containing the chop- and nod-combined flux (see Figure 33) and error values for each grating scan.

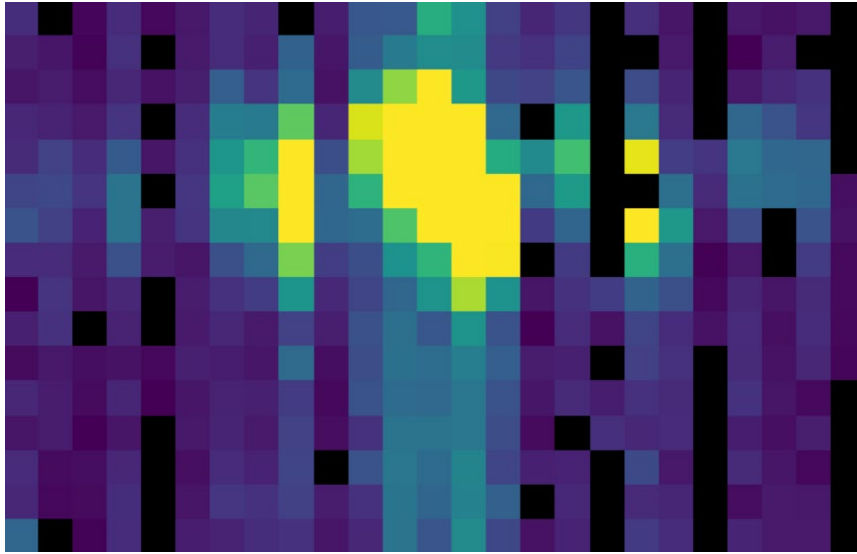


**Figure 33** *The chop-subtracted symmetric mode nod A flux array, with the corresponding nod B added.*

#### 4.4.5 Wavelength Calibration

The wavelength calibrate step calculates wavelength values in microns for each of the spectral pixels in each grating scan, based on the known grating position, a model of the optical geometry of the instrument, and measurements of the positions of known spectral lines. The optics within FIFI-LS tend to drift with time and therefore the FIFI-LS team updated the wavelength solution every year the instrument was used. The wavelength equations (below) are stored in a script, while all relevant constants are stored in a reference table, with an associated date of applicability.

The wavelength ( $\lambda$ ) for the pixel at spatial position  $i$  and spectral position  $j$  is calculated from the equation:

$$\phi_i = 2\pi ISF \frac{ind + ISOFF_i}{2^{24}}$$

$$\delta_j = [j - 8.5] * PS + sign[j - QOFF] * (j - QOFF)^2 * QS$$



$$g_i = g_0 * \cos\left(\frac{SlitPos_i - NP}{a}\right)$$

$$\lambda_{ij} = 1000 \frac{g_i}{m} * [\sin(\phi_i - \gamma) + \sin(\phi_i + \gamma + \delta_j)]$$

where:

- *ind*: the input inductosyn position (physical unit denoting grating position)
- *m*: the spectral order of the observation (1 or 2)

are inputs that depend on the observation settings, and

- *ISF*: inductosyn scaling factor
- *PS*: plate scale, in radians
- *QOFF*: offset of quadratic pixel scale part from the “zero” pixel, in pixels
- *QS*: quadratic pixel scale correcting factor, in radians/pixel<sup>2</sup>
- *g<sub>0</sub>*: grating constant
- *NP*: slit position offset
- *a*: slit position scale factor
- *γ*: offset from Littrow angle

are constants determined by the FIFI-LS team, and

- *ISOFF<sub>i</sub>*: offset of the home position from grating normal in inductosyn units for the *i*<sup>th</sup> spaxel
- *SlitPos<sub>i</sub>*: slit position of the *i*<sup>th</sup> spaxel

are values that depend on the spatial position of the pixel, also determined by the FIFI-LS team. The spaxels are ordered from 1 to 25 spatially as follows:

1	2	3	4	5
6	7	8	9	10
11	12	13	14	15
16	17	18	19	20
21	22	23	24	25

with corresponding slit positions ([Table 10](#)).

**Table 9: The Spaxel Corresponding to Each Slit Position**

Slit P.	Spaxel	Slit P.	Spaxel	Slit P.	Spaxel	Slit P.	Spaxel	Slit P.	Spaxel
1	21	7	16	13	11	19	6	25	1
2	22	8	17	14	12	20	7	26	2
3	23	9	18	15	13	21	8	27	3
4	24	10	19	16	14	22	9	28	4
5	25	11	20	17	15	23	10	29	5
6		12		18		24			

Note that each spectral pixel has a different associated wavelength, but it also has a different effective spectral width. This width ( $d\lambda/dp$ ) is calculated from the following equation:

$$\frac{d\lambda_{ij}}{dp} = 1000 \frac{g_i}{m} [PS + 2 * \text{sign}(j - QOFF) * (j - QOFF) * QS] * \cos(\phi_i + \gamma + \delta_j)$$

where all variables and constants are defined above.

To propagate consistent values throughout the pipeline, all flux values are now divided by the spectral bin width in frequency units:

$$\frac{dv_{ij}}{dp} = \frac{c}{\lambda^2} * \frac{d\lambda_{ij}}{dp}$$

The resulting flux density values (in units of ADU/sec/Hz) are propagated throughout the rest of the pipeline.

The wavelength values calculated by the pipeline for each pixel are stored in a new  $25 \times 16$  array in an image extension for each grating scan (extension name LAMBDA\_Gi for grating scan  $i$ ).

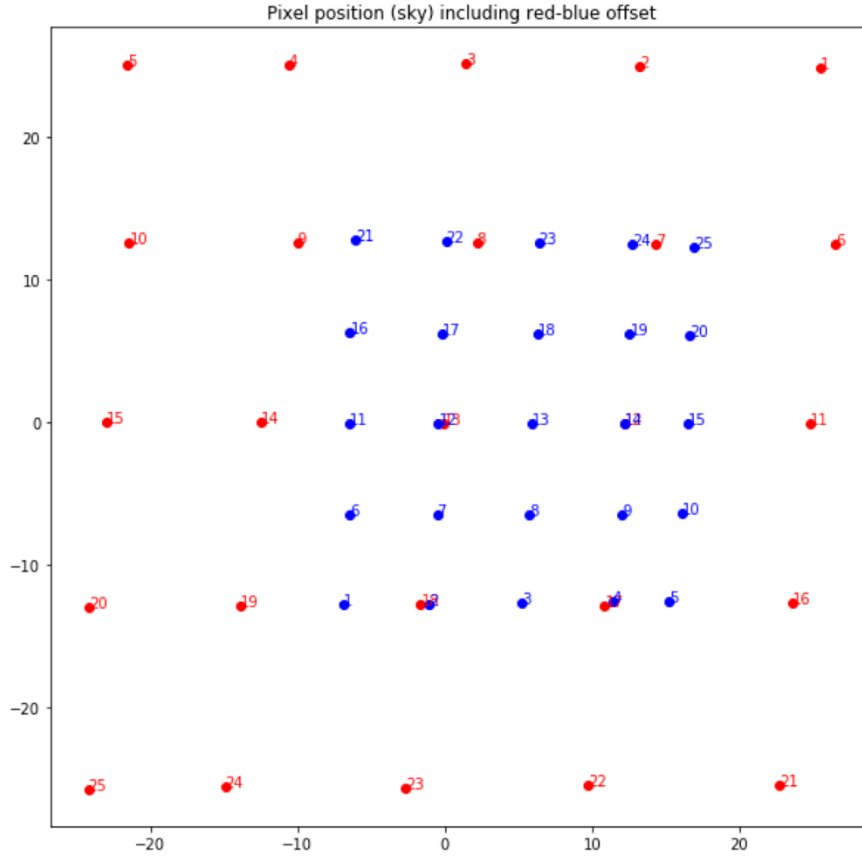


**Figure 34** Average fitted spaxel positions in arcsecond offsets from the center of the detector. The red dots show the positions for the RED channel; blue dots indicate the BLUE channel.

#### 4.4.6 Spatial Calibrate

The locations of the spaxels are not uniformly spaced in the sky, due to the optics not being perfectly aligned. See [Figure 34](#) for a plot of the average of the center of each spaxel location, as measured in the lab. In addition, their locations are slightly different at different wavelengths. These spaxel positions are determined by the FIFI-LS team and recorded in a look-up table.

For a particular observation in standard chop-nod modes, the recorded dither offsets in arcseconds are used to calculate the x and y coordinates for the pixel in the  $i^{\text{th}}$  spatial position and the  $j^{\text{th}}$  spectral position using the following formulae:

$$x_{ij} = ps(xpos_{ij} + dx) + d\lambda * \cos(\theta) - d\beta \sin(\theta)$$

$$y_{ij} = ps(ypos_{ij} + dy) + d\lambda * \sin(\theta) + d\beta \cos(\theta)$$

where  $ps$  is the plate scale in arcsec/mm (FITS header keyword PLATSCAL),  $d\lambda$  is the right ascension dither offset in arcsec (keyword DLAM\_MAP),  $d\beta$  is the declination dither offset in arcsec (keyword DBET\_MAP),  $\theta$  is the detector angle,  $xpos_{ij}$  and  $ypos_{ij}$  are the fitted spaxel

positions in mm for pixel  $(i, j)$ , and  $dx$  and  $dy$  are the spatial offsets between the primary array (usually BLUE), used for telescope pointing, and the secondary array (usually RED). The  $dx$  and  $dy$  offsets also consider a small offset between the instrument boresight and the telescope boresight, for both the primary and secondary arrays. By default, the coordinates are then rotated by the detector angle (minus  $180^\circ$ ), and the  $y$ -coordinates are inverted to set North up and East left in the final coordinate system:

$$\begin{aligned}x'_{ij} &= -x_{ij} \cos(\theta) + y_{ij} \sin(\theta) \\y'_{ij} &= x_{ij} \sin(\theta) + y_{ij} \cos(\theta)\end{aligned}$$

The pipeline stores these calculated  $x$  and  $y$  coordinates for each spaxel in two 25 element arrays for each grating scan (extensions `XS_Gi` and `YS_Gi` for grating scan  $i$ ).

In addition, the pipeline uses the base position for the observation and the computed offsets to derive true sky coordinates for each spaxel, in RA (decimal hours) and Dec (decimal degrees). These positions are also stored in the output file in separate image extensions for each grating scan (`RA_Gi` and `DEC_Gi` for grating scan  $i$ ), with array dimensions matching the corresponding `XS` and `YS` extensions.

For OTF data, the process is the same as described above, except that each ramp in the input data has its own `DLAM_MAP` and `DBET_MAP` value, recorded in the `SCANPOS` table, rather than in the primary FITS header. The output spatial coordinates match the number of spaxels and ramps in the flux data, which has dimensions  $25 \times 16 \times N_{\text{ramp}}$ , such that the `XS_Gi`, `YS_Gi`, `RA_Gi`, and `DEC_Gi`, extensions have dimensions  $25 \times 1 \times N_{\text{ramp}}$ .

### 4.4.7 Apply Flat

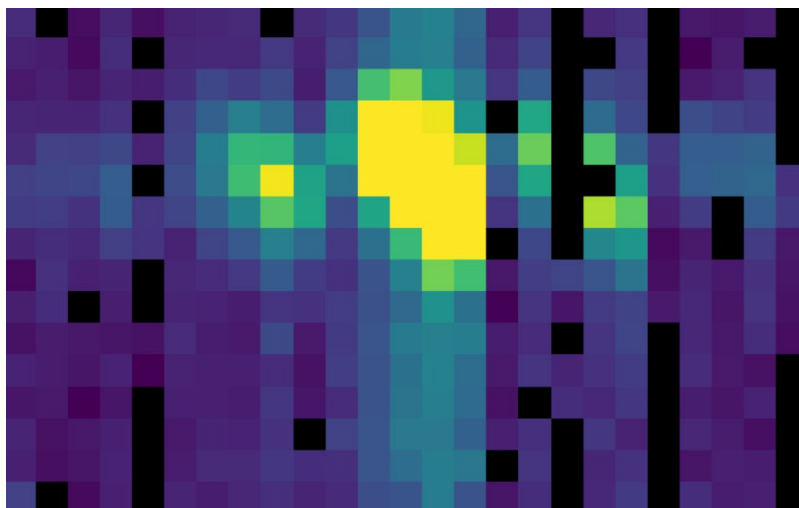


**Figure 35** *The flat-corrected flux array.*

To correct for variations in response among the individual pixels, the FIFI-LS team has generated flat field data. There is a normalized spatial flat field for each of the RED and BLUE channels, which specifies the correction for each spaxel. This correction may vary over time. There is also a

set of spectral flat fields, for each channel, order, and dichroic, over the full wavelength range for the mode, which specifies the correction for each spixel.

To apply the flat fields to the data, the pipeline interpolates the appropriate spectral flat onto the wavelengths of the observation, for each spixel, then multiplies the value by the appropriate spatial flat. The flux is then divided by this correction value (Figure 35). The updated flux and associated error values are stored in the FLUX\_Gi and STDDDEV\_Gi extensions.

#### 4.4.8 Combine Grating Scans

Up until this point, all processing has been done on each grating scan separately. The pipeline now combines the data from all grating scans, to fill in the wavelength coverage of the observation.

Due to slight variations in the readout electronics, there may be additive offsets in the overall flux level recorded in each grating scan. To correct for this bias offset, the pipeline calculates the mean value of all pixels in the overlapping wavelength regions for each grating scan. This value, minus the mean over all scans, is subtracted from each grating scan, to set all extensions to a common bias level (Figure 36).

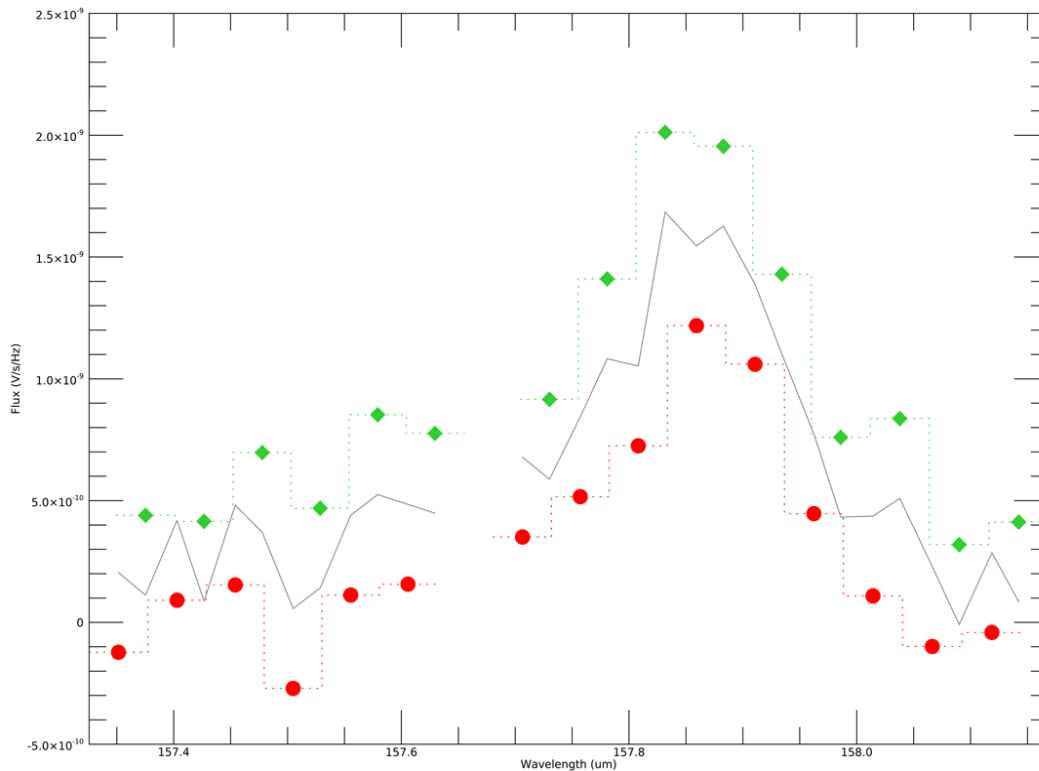


**Figure 36** Example spectral flux from the center spixel for a single dither position. The red circles and green diamonds represent two different grating scans. The gray line indicates the combined flux array, after bias correction.

For standard chop/nod modes, the pipeline sorts the data from all grating scans by their associated wavelength values in microns and stores the result in a single data array with dimensions  $25 \times (16 * N_{\text{scan}})$ , where  $N_{\text{scan}}$  is the total number of grating scans in the input file. Note that the wavelengths are still irregularly sampled at this point, due to the differing wavelength solutions for each grating

scan and spatial pixel (Figure 37). All arrays in the output FITS file (FLUX, STDDEV, LAMBDA, XS, YS, RA, and DEC) now have dimensions  $25 \times (16 * N_{\text{scan}})$ .

For the OTF mode, only a single grating scan exists. The output FLUX, STDDEV, XS, YS, RA, and DEC arrays for this mode have dimensions  $25 \times 16 \times N_{\text{ramp}}$ . Since the wavelength solution does not depend on the sky position, the LAMBDA array has dimensions  $25 \times 16$ .

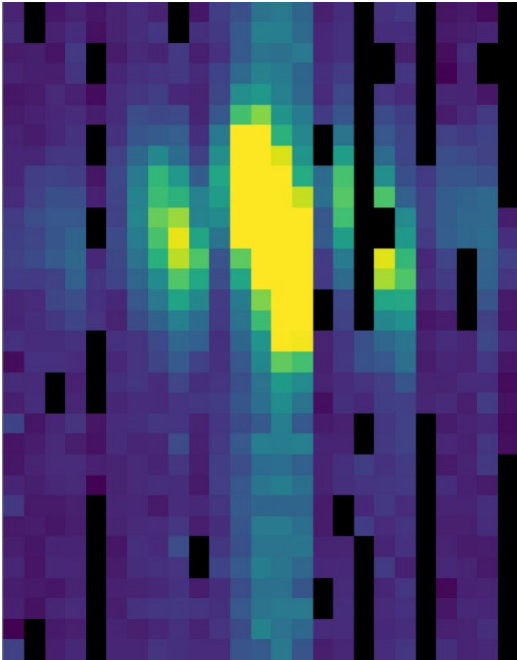


**Figure 37** The full  $25 \times 16 \times 2$  (flattened to  $25 \times 32$ ) flux array, after combining two grating scans.

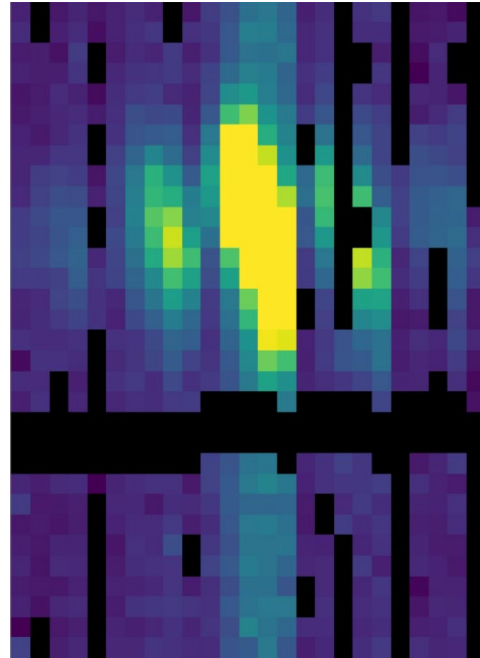


**Figure 38** The telluric-corrected flux array. Some pixels are set to NaN due to poor atmospheric transmission at those wavelengths. The cutoff level was set to 80% for this observation, for illustrative purposes.

### 4.4.9 Telluric Correction

Telluric correction is the process of attempting to correct an observed spectrum for absorption by molecules in the earth’s atmosphere, to recover the intrinsic (“exo-atmospheric”) spectrum of the source. The atmospheric molecular components (primarily water, ozone, and CO<sub>2</sub>) can produce both broad absorption features that are well resolved by FIFI-LS and narrow, unresolved features. The strongest absorption features are expected to be due to water. Because SOFIA traveled quite large distances during even short observing legs, the water vapor content along the line of sight through the atmosphere could vary substantially on short timescales during an observation. Therefore, observing a “telluric standard,” as is usually done for ground-based observations, will not necessarily provide an accurate absorption correction spectrum. For this reason, telluric corrections of FIFI-LS data relied on models of the atmospheric absorption, as provided by codes such as ATRAN, in combination with the estimated line-of-sight water vapor content (precipitable water vapor, PWV).

The correction spectra are generated using PWV values derived from observations of telluric lines made with FIFI-LS during the set-up period at the start of observing legs and after changes of altitude. This is described in more detail in Section 4.8 below. Experience has shown that these



provided better corrections than simply using the expected value for the flight altitude and airmass, particularly at wavelengths with deep, sharp features (e.g., near 63  $\mu\text{m}$ ). However, accurate correction of spectral lines near narrow telluric absorption features is problematic even with good atmospheric models and knowledge of the PWV. This is because the observed spectrum is the result of a multiplication of the intrinsic spectrum by the telluric absorption spectrum, and then a convolution of the product with the instrumental profile, whereas the correction derived from a model is the result of the convolution of the theoretical telluric absorption spectrum with the instrumental profile. The division of the former by the latter does not necessarily yield the correct results, and the output spectrum may retain telluric artifacts after telluric correction.

A set of ATRAN models appropriate for a range of altitudes, zenith angles, and PWV values has been generated for pipeline use. In the telluric correction step, the pipeline selects the model closest to the observed altitude, zenith angle, and PWV value and smooths the transmission model to the resolution of the observed spectrum, interpolates the transmission data to the observed wavelength at each pixel, and then divides the data by the transmission model. A custom PWV can be set during the pipeline reduction process; see Section 4.6.3. Extremely low transmission values result in poor corrections, so any pixel for which the transmission is less than 60% (by default) is set to NaN. For reference, the smoothed, binned transmission data is attached to the FITS file as a  $25 \times (16 * N_{\text{scan}})$  data array (extension ATRAN). The original unsmoothed data is attached as well, in the extension UNSMOOTHED\_ATRAN.

Since the telluric correction may introduce artifacts, or may, at some wavelength settings, produce flux cubes for which all pixels are set to NaN, the pipeline also propagates the uncorrected flux cube through the remaining reduction steps (Figure 38). The telluric-corrected cube and its associated error are stored in the FLUX and STDDEV extensions. The uncorrected cube and its associated error are stored in the UNCORRECTED\_FLUX and UNCORRECTED\_STDDEV extensions.

### 4.4.10 Flux Calibrate

Flux calibration of FIFI-LS data is carried out via the division of the instrumental response, as recorded in response files appropriate for each grating setting, wavelength range, and dichroic. The response values have units of ADU/s/Hz/Jy and are derived from observations of “flux standards.” At the wavelengths at which FIFI-LS operated, there are very few stars bright enough to yield high signal-to-noise data useful for flux calibration purposes. Therefore, observations of asteroids, planets, and planetary moons were used, along with models of such objects, to derive the response curves. Since the observed fluxes of such solar system objects vary with time, the models had to be generated for the time of each specific observation. Observations of Mars were used as the primary flux calibration source. Predicted total fluxes for Mars across the FIFI-LS passband at the specific UT dates of the observations were generated using the model of [Lellouch & Amri \(2006\)](#). Predicted fluxes at several frequencies have been computed and then have then been fitted with blackbody curves to derive values at many wavelength points. The deviations of the fits from the input predictions are much less than 1%. After the models have been generated, the telluric-corrected spectra of the standards, in units of ADU/s/Hz, are divided by the theoretical spectra, in Jy. The results are smoothed and then fit with a polynomial to derive response functions (ADU/s/Hz/Jy) that can then be used to flux calibrate the telluric-corrected spectra of other astronomical sources (Figure 39).

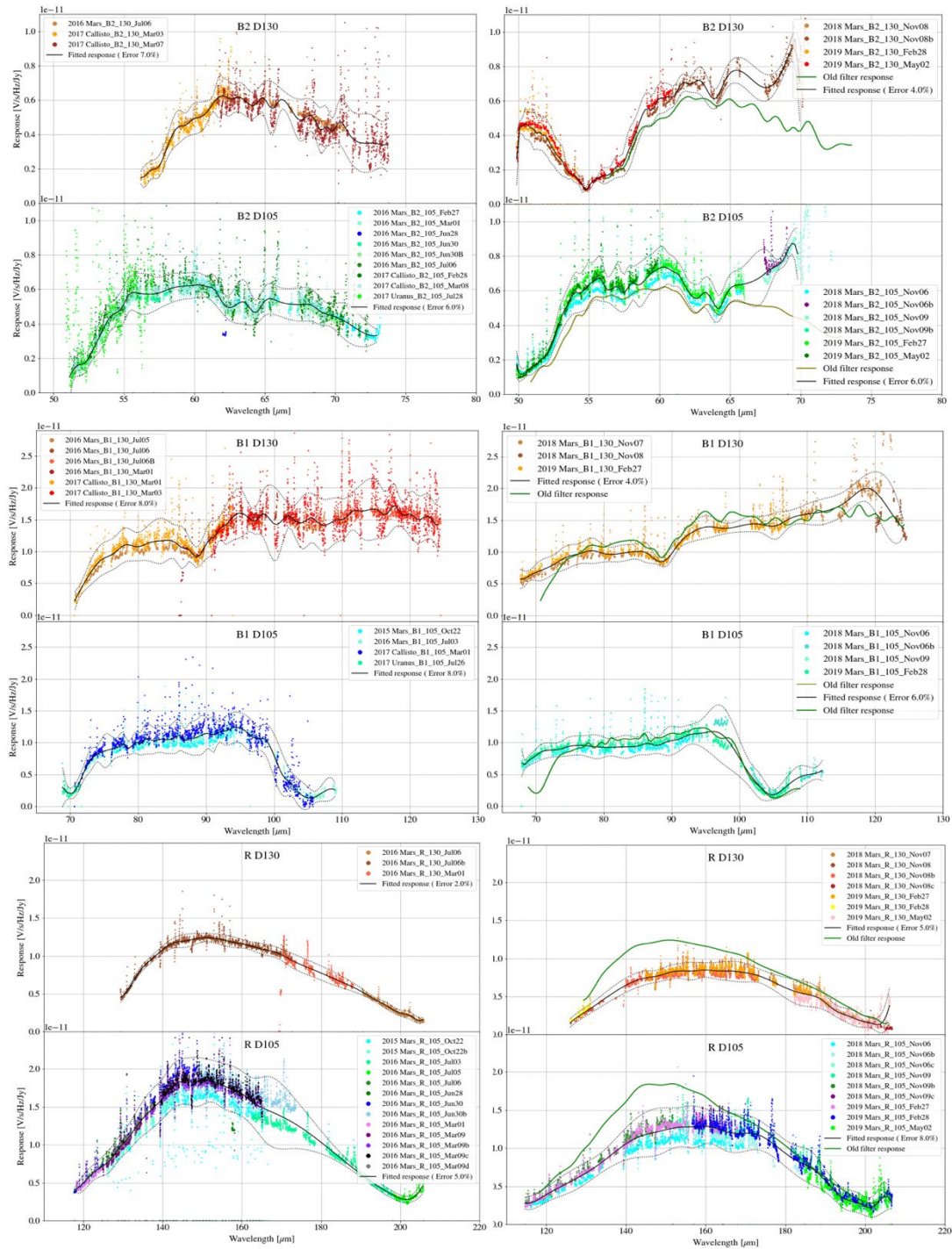


**Figure 39** Response obtained in 2019 and used until 2022 before the latest release of the FIFI-LS pipeline in 2023. The curves are overplotted on telluric-corrected data, with model spectra divided out. Data shown was taken in 2015-2019 for the blue channel order 2, blue channel order 1, and red channel. Plots on the left are from an older filter set; plots on the right are for data taken with an updated filter set.

The pipeline stores a set of response functions for each channel and dichroic value. To perform flux calibration, it selects the correct response function for each input observation, interpolates the response onto the wavelengths of each spixel, and divides the flux by the response value to convert it to physical units (Jy/pixel). From this point on, the data products are Level 3 (FITS keyword PROCSTAT=LEVEL\_3). For reference, the resampled response data is attached to the FITS file as a  $25 \times (16 * N_{\text{scan}})$  data table in the first FITS extension (column RESPONSE). Flux calibration is applied to both the telluric-corrected cube and the uncorrected cube. The estimated systematic error in the flux calibration is recorded in the CALERR keyword in the FITS header, as an average fractional error. Flux calibration is expected to be good to within about 5-10% ( $\text{CALERR} \leq 0.1$ ).

### 4.4.11 Correct Wave Shift

Due to the motion of the Earth with respect to the barycenter of the solar system, the wavelengths of features in the spectra of astronomical sources will appear to be slightly shifted, by different amounts on different observation dates. To avoid introducing a broadening of spectral features when multiple observations obtained over different nights are combined, the wavelength calibration of FIFI-LS observations must be adjusted to remove the barycentric wavelength shift. This shift is calculated as an expected wavelength shift ( $d\lambda/\lambda$ ), from the radial velocity of the earth with respect to the solar barycenter on the observation date, toward the RA and Dec of the observed target. This shift is recorded in the header keyword BARYSHFT, and applied to the wavelength calibration in the LAMBDA extension as:

$$\lambda' = \lambda + \lambda \left( \frac{d\lambda}{\lambda} \right)$$

Since the telluric absorption lines do not change with the motion of the earth, the barycentric wavelength shift cannot be applied to non-telluric-corrected data. Doing so would result in a spectrum in which both the intrinsic features and the telluric lines are shifted. Therefore, the unshifted wavelength calibration is also propagated in the output file, in the extension UNCORRECTED\_LAMBDA.

It is possible to apply an additional wavelength shift to correct for the solar system's velocity with respect to the local standard of rest (LSR). This shift is calculated and stored in the header keyword LSRSHFT, but it is not applied to the wavelength calibration. Note that earlier versions of this pipeline (prior to v2.4.0) applied both the barycentric shift and the shift to LSR to the wavelength calibration. The summed barycentric and LSR radial velocity was stored as the BARYSHFT value.

### 4.4.12 Resample

In the last step, the pipeline resamples the flux for each spatial and spectral pixel onto a regular 3D grid (right ascension, declination, and wavelength). This step combines the spatial information from all input nod-combined dither positions into a single output map. See [Figure 40](#) for an overview of the resampling algorithm.

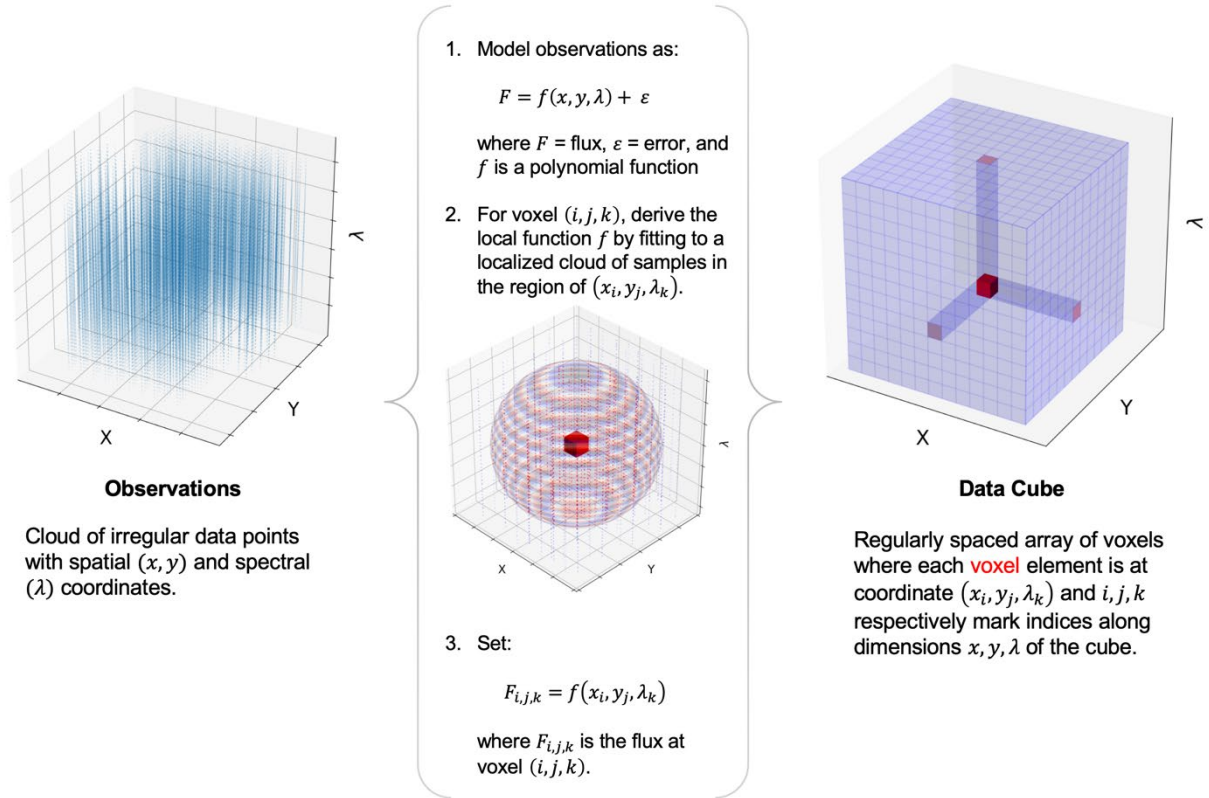


**Figure 40** Overview of the resampling algorithm. Given a cloud of irregularly spaced data points, the algorithm assigns values to voxels of a regular grid by fitting data points in a local cloud with a low-order polynomial function.

#### 4.4.12.1 Grid Size

The pipeline first determines the maximum and minimum wavelengths and spatial offsets present in all input files by projecting all dither positions for the observation into a common world coordinate system (WCS) reference frame. For OTF data, the scan positions for each ramp in each input file are also considered. The full range of sky positions and wavelengths observed sets the range of the output grid.

The spacing of the output grid in the wavelength dimension ( $dw$ ) is set by the desired oversampling. By default, in the wavelength dimension, the pipeline samples the average expected spectral FWHM for the observation (Table 11) with eight output pixels.

The spacing in the spatial dimensions ( $dx$ ) is fixed for each channel at 1.5 arcseconds in the BLUE and 3.0 arcseconds in the RED. These values are chosen to ensure an oversampling of the spatial FWHM by at least a factor of three.

For example, for the RED observation in the figures above, the expected spectral FWHM at the central wavelength is  $0.13 \mu\text{m}$ , so sampling this FWHM with eight pixels creates a grid with a spectral width of  $0.016 \mu\text{m}$ . Given a min and max wavelength of  $157.27 \mu\text{m}$  and  $158.48 \mu\text{m}$ , the output grid will sample the full range of wavelengths with 76 spectral pixels. Since it is a RED



channel observation, the spatial scale will be 3.0 arcseconds. If the range of x offsets is -41.0 to 57.74 and the range of y offsets is -43.9 to 36.9, then the output spatial grid will have dimensions  $33 \times 27$ , with an oversampling of the FWHM (using the interpolated value at  $157.876 \mu\text{m}$  of 15.6 arcseconds) of 5.2. The full output cube is then  $33 \times 27 \times 76$  ( $n_x \times n_y \times n_w$ ).

**Table 10: Spectral and Spatial Resolution by Central Wavelength**

Channel/Order	Wavelength ( $\mu\text{m}$ )	Spectral Resolution ( $\lambda / d\lambda$ )	Spatial Resolution (arcsec)
Blue Order 1	70	545	6.9
Blue Order 1	80	570	7.9
Blue Order 1	90	628	8.9
Blue Order 1	100	720	9.9
Blue Order 1	110	846	11.0
Blue Order 1	120	1005	12.0
Blue Order 2	45	947	5.9
Blue Order 2	50	920	6.2
Blue Order 2	65	1415	7.3
Blue Order 2	70	1772	7.7
Red	120	747	11.9
Red	140	939	13.9
Red	160	1180	15.8
Red	180	1471	17.7
Red	200	1813	19.6

In the spatial dimensions, the flux in each pixel represents an integrated flux over the area of the pixel. Since the pixel width changes after resampling, the output flux must be corrected for flux conservation. To do so, the resampled flux is multiplied by the area of the new pixel ( $dx^2$ ) and divided by the intrinsic area of the spaxel (approximately  $36 \text{ arcseconds}^2$  for BLUE,  $144 \text{ arcseconds}^2$  for RED).

#### 4.4.12.2 *Algorithm*

For each pixel in the 3D output grid, the resampling algorithm finds all flux values with assigned wavelengths and spatial positions within a fitting window, typically 0.5 times the spectral FWHM in the wavelength dimension, and 3 times the spatial FWHM in the spatial dimensions. For the spatial grid, a larger fit window is typically necessary than for the spectral grid, since the observation setup usually allows more oversampling in wavelength than in space.

A low-order 3D polynomial surface is then fit to all the good data points within the window. The fit is weighted by the error on the flux, as calculated by the pipeline, and a Gaussian function of the distance of the input data value from the grid location. The distance weighting function may be held constant for each output pixel, or it may optionally be allowed to vary in scale and shape in response to the input data characteristics. This adaptive smoothing kernel may help in preserving peak flux values for bright, compact flux regions, but may over-fit the input data in some sparsely sampled observations (see [Figure 41](#)).

The output flux value for this algorithm is the value of the fit polynomial surface, evaluated at the grid location, and the associated error is the error on the fit (see [Figure 42](#)).

Output grid locations for which there was insufficient input data for stable polynomial fits are set to NaN. The threshold for how much output data is considered invalid is a tunable parameter, but it is typically set to eliminate most edge effect artifacts from the final output cube.

For some types of observations, especially un-dithered observations of point sources for which the spatial FWHM is under-sampled, the polynomial surface fits may not return satisfactory results. In these cases, it is beneficial to use an alternate resampling algorithm. In this algorithm, the master grid is determined as above, but each input file is resampled with polynomial fits in the wavelength dimension only. Then, for each wavelength plane, the spatial data is interpolated onto the grid, using radial basis function interpolation. Areas of the spatial grid for which there is no data in the input file are set to NaN. The interpolated cubes are then averaged, ignoring any NaNs, to produce the final output cube.

For either algorithm, the pipeline also generates an exposure map cube indicating the number of observations of the source that were taken at each pixel (see [Figure 43](#)). These exposure counts correspond to the sum over the projection of the detector field of view for each input observation onto the output grid. The exposure map may not exactly match the valid data locations in the flux cube since additional flagging and pixel rejection occurs during the resampling algorithms.

#### 4.4.12.3 *Uncorrected Flux Cube*

Both the telluric-corrected and the uncorrected flux cubes are resampled in this step, onto the same 3D grid. However, the telluric-corrected cube is resampled using the wavelengths corrected for barycentric motion, and the uncorrected cube is resampled using the original wavelength calibration. The spectra from the uncorrected cube will appear slightly shifted with respect to the spectra from the telluric-corrected cube.

#### 4.4.12.4 *Detector Coordinates*

For most observations, the output grid is determined from projected sky coordinates for each input data point, for the most accurate astrometry in the output map. However, this is undesirable for non-sidereal data, for which the target's sky coordinates change over the observation. For non-sidereal sources, the detector offsets (from input XS and YS extensions) are used instead of the



sky coordinates (from RA and DEC extensions) to generate the output grid. For all other sources, detector coordinates may optionally be used instead of sky coordinates.

### 4.4.12.5 *Additional Scan Processing*

For OTF data, the standard sky subtraction and flat correction algorithms may not be sufficient to remove residual sky and detector noise. In this mode, temporal variations frequently result in artifacts like striping along the scan direction, or residual sky backgrounds that overwhelm diffuse emission.

In this case, it may be beneficial to apply an iterative correction to the detector gain and noise. For OTF data, the FIFI-LS pipeline provides this correction as an optional scan reduction step, just prior to resampling. The iterative scan reduction algorithm is described at length in the HAWC+ Pipeline User's Manual and in the software documentation for the `sofia_redux.scan` module.

### 4.4.12.6 *Output Data*

The pipeline stores the resampled data as a 3D FITS image extension with the extension name `FLUX`. The associated error is stored in a separate extension, with the name `ERROR`. The non-telluric-corrected cubes are stored in `UNCORRECTED_FLUX` and `UNCORRECTED_ERROR` extensions, respectively. The output wavelengths, x and y offsets, and RA and Dec coordinates are stored in `WAVELENGTH`, `X`, `Y`, `RA-TAN`, and `DEC-TAN` extensions.

For reference, a model of the atmospheric transmission spectrum, smoothed to the resolution of the observation, and the instrumental response curve used in flux calibration are also attached to the FITS file in 1D extensions called `TRANSMISSION` and `RESPONSE`.

Finally, an unsmoothed transmission spectrum is attached in a 2D image extension called `UNSMOOTHED_TRANSMISSION`. This extension will have size  $N_{\text{trans}} \times 2$ , where  $N_{\text{trans}}$  is the number of data points in the spectrum, the first row is the wavelength array, and the second row is the transmission fraction. This spectrum may be useful for further analysis of the data (e.g., for determining the total flux in an emission line).

The final output from the pipeline is a FITS file with 11 image extensions:

- `FLUX`: The  $n_x \times n_y \times n_w$  cube of flux values.
- `ERROR`: The associated error values on the flux (also  $n_x \times n_y \times n_w$ ).
- `UNCORRECTED_FLUX`: The  $n_x \times n_y \times n_w$  cube of flux values that have not been corrected for atmospheric transmission.
- `UNCORRECTED_ERROR`: The associated error values on the uncorrected flux (also  $n_x \times n_y \times n_w$ ).
- `WAVELENGTH`: The wavelength values associated with each plane of the cube ( $n_w$ ).
- `X`: The x-coordinates of the data, in arcsecond offsets from the base position ( $n_x$ ).
- `Y`: The y-coordinates of the data, in arcsecond offsets from the base position ( $n_y$ ).
- `RA-TAN`: The right ascension coordinates of the data, in decimal hours, in a tangent projection from the base position.

- DEC-TAN: The declination coordinates of the data, in decimal degrees, in a tangent projection from the base position.
- TRANSMISSION: The atmospheric transmission model (nw).
- RESPONSE: The instrumental response curve (nw).
- EXPOSURE\_MAP: The exposure map ( $n_x \times n_y \times n_w$ ).
- UNSMOOTHED\_TRANSMISSION: The unsmoothed atmospheric transmission model ( $N_{\text{trans}} \times 2$ ).

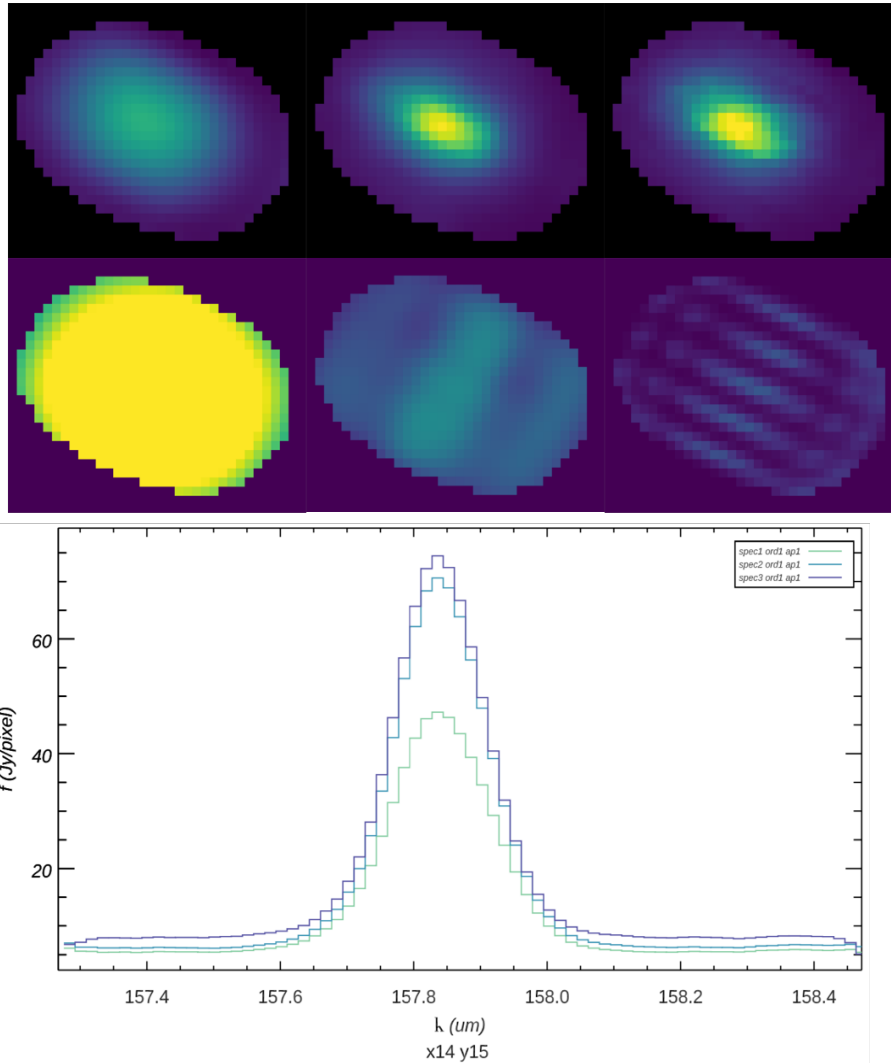


**Figure 41** Comparison of a non-adaptive (left), adaptively scaled (middle), and adaptively shaped and scaled (right) smoothing kernel for the above target, using a baseline smoothing radius corresponding to the spatial beam size. The top row shows the spatial slice at wavelength 157.83 um, locked to a common display scale. The bottom row shows the distance weights used by the resampling algorithm at the wavelength slice shown, also locked to a common display scale. Distance weights correlate with the size of the kernel used and the number of input pixels within the fit window. The plot below compares the spectral slice at pixel  $x,y = 14, 15$  for the three resampled versions: green is non-adaptive, blue is adaptively scaled, and purple is adaptively shaped and scaled.

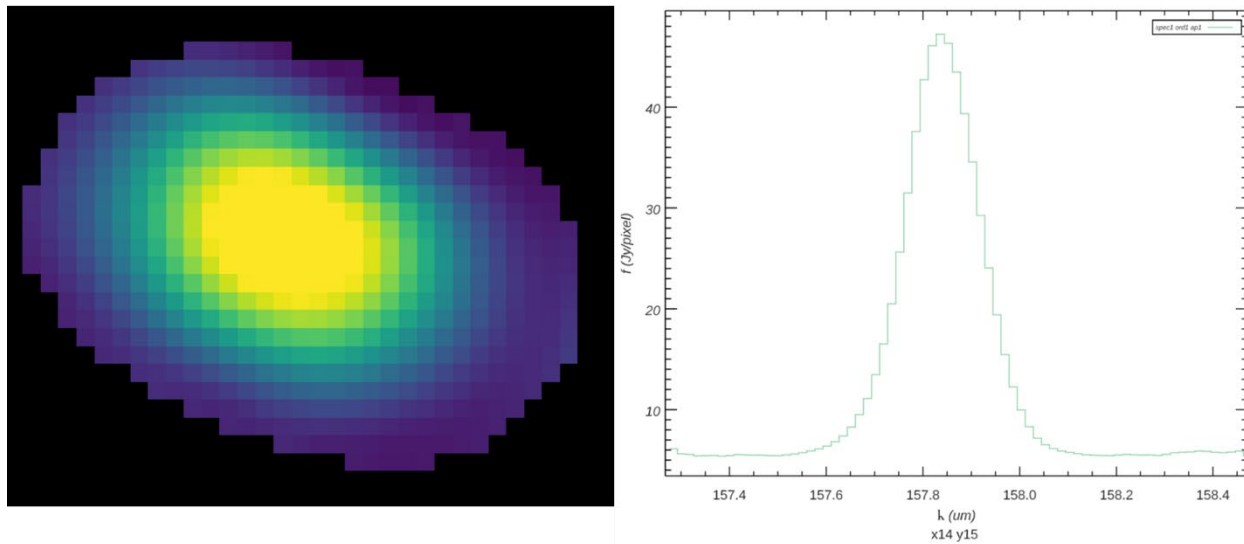


**Figure 42** The final output flux cube. The image on the left is a spatial slice at wavelength  $157.83 \mu\text{m}$ . The plot on the right is a spectral slice at pixel  $x,y = 14, 15$ , near the peak of the source.

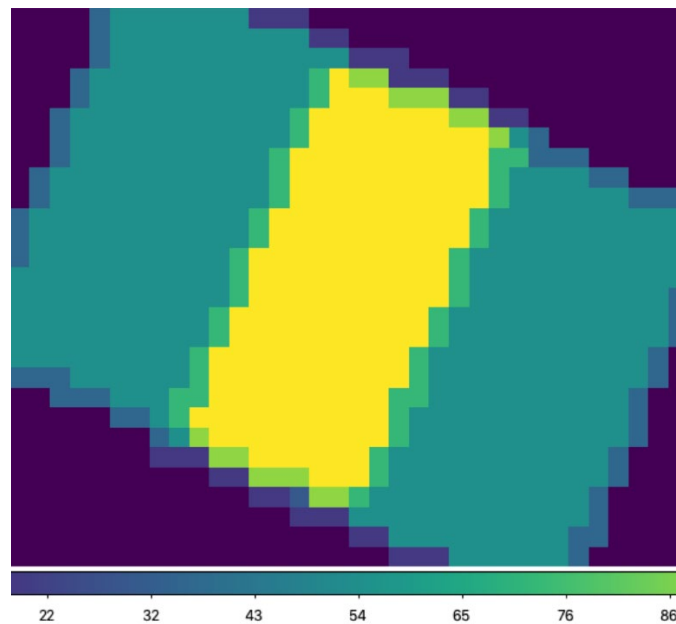


**Figure 43** Exposure map of input dither positions, corresponding to the above flux cube. Values range from 0 (purple, near the edges) to 108 (yellow, near the center).

#### 4.5 AUTOMATIC REDUCTION

The DPS pipeline infrastructure runs a pipeline on previously defined reduction groups as a fully automatic black box. To do so, it creates an input manifest (*infile.txt*) that contains relative paths to the input files (one per line). The command-line interface to the pipeline is run as:

```
$ redux_pipe infile.txt
```

The command-line interface will read in the specified input files, use their headers to determine the observation mode, the steps to run, and any intermediate files to save. Output files are written to the current directory, from which the pipeline was called. After reduction is complete, the script will generate an output manifest (*outfile.txt*) containing the relative paths to all output FITS files generated by the pipeline.

Optionally, in place of a manifest file, file paths to input files may be explicitly specified on the command line. Input files may be raw FITS files or intermediate products previously produced by the pipeline. For example, this command will complete the reduction for a set of FITS files in the current directory, previously reduced through the calibration step of the pipeline:

```
$ redux_pipe *CAL*.fits
```

To customize batch reductions from the command line, the `redux_pipe` interface accepts a configuration file on the command line. This file may contain any subset of the full configuration file, specifying any non-default parameters for pipeline steps. An output directory for pipeline products and the terminal log level may also be set on the command line.

The full set of optional command-line parameters accepted by the `redux_pipe` interface is:

```
-h, --help                show this help message and exit
-c CONFIG, --configuration CONFIG
                          Path to Redux configuration file.
-o OUTDIR, --out OUTDIR
                          Path to output directory.
-l LOGLEVEL, --loglevel LOGLEVEL
                          Log level.
```

### 4.6 MANUAL REDUCTION

In manual mode, the pipeline may be run interactively, via a graphical user interface (GUI) provided by the Redux package. The GUI is launched by the command:

```
$ redux
```

entered at the terminal prompt. The GUI allows output directory specification, but it may write initial or temporary files to the current directory, so it is recommended to start the interface from a location to which the user has write privileges.

From the command line, the `redux` interface accepts an optional config file (-c) or log level specification (-l), in the same way the `redux_pipe` command does. Any pipeline parameters provided to the interface in a configuration file will be used to set default values; they will still be editable from the GUI.

#### 4.6.1 Basic Workflow

To start an interactive reduction, select a set of input files, using the File menu (**File** → **Open New Reduction**). This will bring up a file dialog window ([Figure 44](#)). All files selected will be reduced together as a single reduction set.

Redux will decide the appropriate reduction steps from the input files, and load them into the GUI, as in [Figure 45](#).

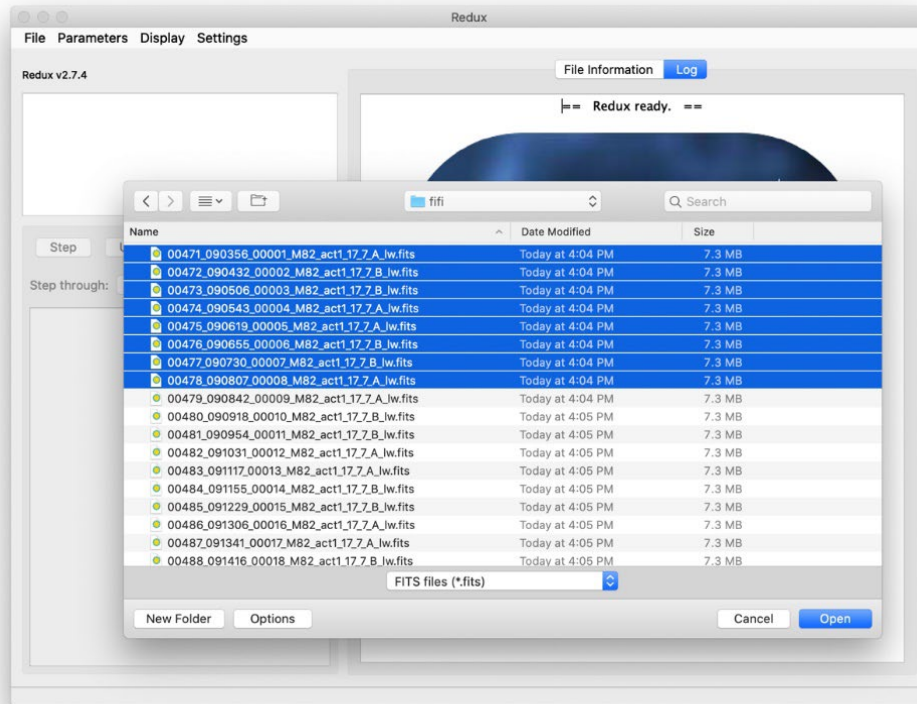


**Figure 44** *Open new reduction.*

Each reduction step has a few parameters that can be edited before running the step. To examine or edit these parameters, click the **Edit** button next to the step name to bring up the parameter editor for that step ([Figure 46](#)). Within the parameter editor, all values may be edited. Click **OK** to save the edited values and close the window. Click **Reset** to restore any edited values to their last saved values. Click **Restore Defaults** to reset all values to their stored defaults. Click **Cancel** to discard all changes to the parameters and close the editor window.

The current set of parameters can be displayed, saved to a file, or reset all at once using the **Parameters** menu. A previously saved set of parameters can also be restored for use with the current reduction (**Parameters** → **Load Parameters**).

After all parameters for a step have been examined and set to the user’s satisfaction, a processing step can be run on all loaded files either by clicking **Step**, or the **Run** button next to the step name. Each processing step must be run in order, but if a processing step is selected in the **Step through** widget, then clicking **Step** will treat all steps up through the selected step as a single step and run them all at once. When a step has been completed, its buttons become gray and inaccessible.

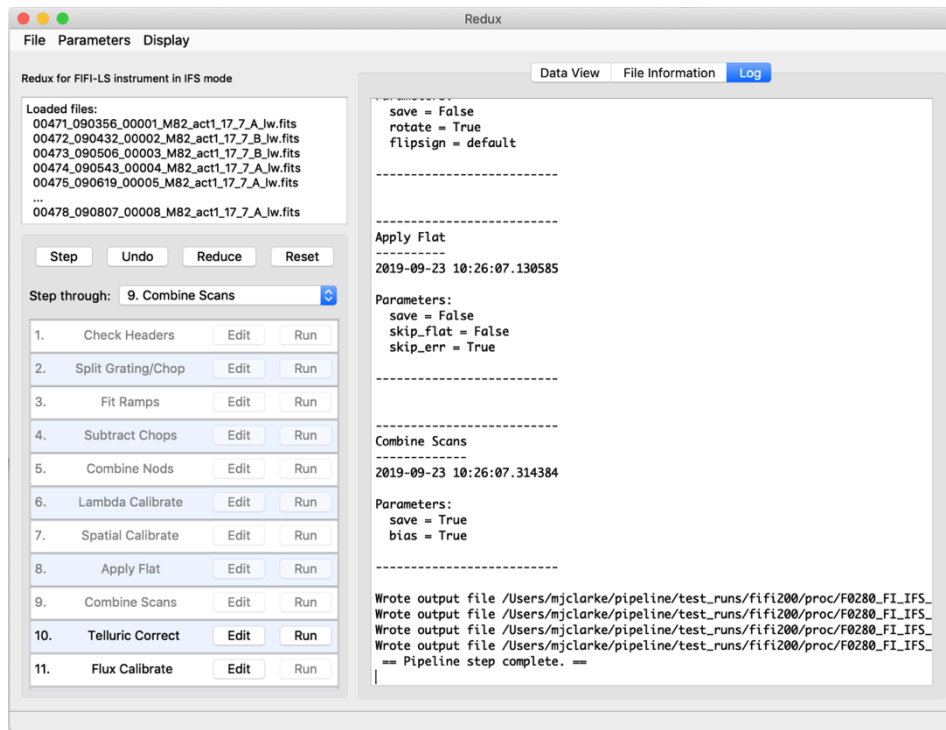


Figure 45 Sample reduction steps. Log output from the pipeline is displayed in the Log tab.

It is possible to undo one previous step by clicking **Undo**. All remaining steps can be run at once by clicking **Reduce**. After each step, the results of the processing may be displayed in a data

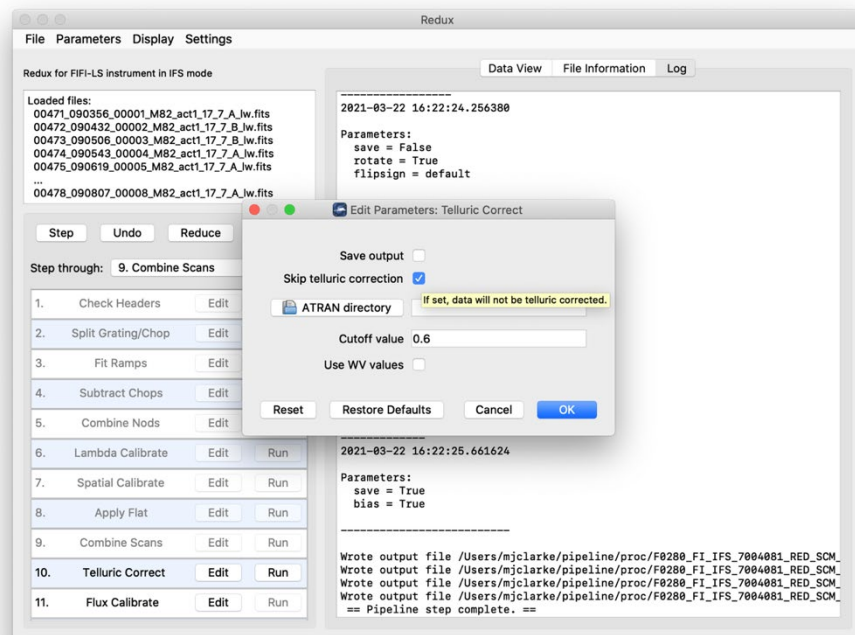
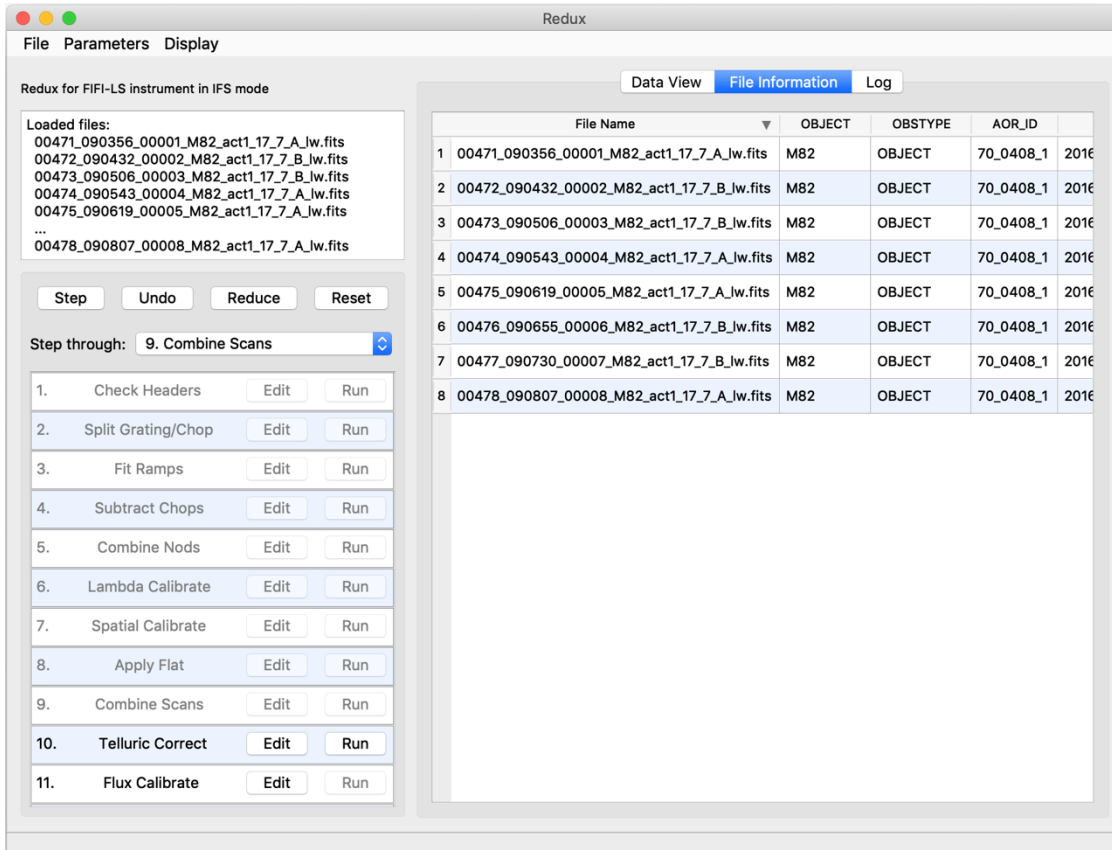


Figure 46 Sample parameter editor for a pipeline step.



viewer. After running a pipeline step or reduction, click **Reset** to restore the reduction to the initial state, without resetting parameter values.

Files can be added to the reduction set (**File** → **Add Files**) or removed from the reduction set (**File** → **Remove Files**), but either action will reset the reduction for all loaded files. Select the **File Information** tab to display a table of information about the currently loaded files ([Figure 47](#)).



Redux

File Parameters Display

Redux for FIFI-LS instrument in IFS mode

Loaded files:  
 00471\_090356\_00001\_M82\_act1\_17\_7\_A\_lw.fits  
 00472\_090432\_00002\_M82\_act1\_17\_7\_B\_lw.fits  
 00473\_090506\_00003\_M82\_act1\_17\_7\_B\_lw.fits  
 00474\_090543\_00004\_M82\_act1\_17\_7\_A\_lw.fits  
 00475\_090619\_00005\_M82\_act1\_17\_7\_A\_lw.fits  
 ...  
 00478\_090807\_00008\_M82\_act1\_17\_7\_A\_lw.fits

Step Undo Reduce Reset

Step through: 9. Combine Scans

	File Name	OBJECT	OBSTYPE	AOR_ID	
1	00471_090356_00001_M82_act1_17_7_A_lw.fits	M82	OBJECT	70_0408_1	2016
2	00472_090432_00002_M82_act1_17_7_B_lw.fits	M82	OBJECT	70_0408_1	2016
3	00473_090506_00003_M82_act1_17_7_B_lw.fits	M82	OBJECT	70_0408_1	2016
4	00474_090543_00004_M82_act1_17_7_A_lw.fits	M82	OBJECT	70_0408_1	2016
5	00475_090619_00005_M82_act1_17_7_A_lw.fits	M82	OBJECT	70_0408_1	2016
6	00476_090655_00006_M82_act1_17_7_B_lw.fits	M82	OBJECT	70_0408_1	2016
7	00477_090730_00007_M82_act1_17_7_B_lw.fits	M82	OBJECT	70_0408_1	2016
8	00478_090807_00008_M82_act1_17_7_A_lw.fits	M82	OBJECT	70_0408_1	2016

1. Check Headers Edit Run
2. Split Grating/Chop Edit Run
3. Fit Ramps Edit Run
4. Subtract Chops Edit Run
5. Combine Nods Edit Run
6. Lambda Calibrate Edit Run
7. Spatial Calibrate Edit Run
8. Apply Flat Edit Run
9. Combine Scans Edit Run
10. Telluric Correct Edit Run
11. Flux Calibrate Edit Run

**Figure 47** *File information table.*

### 4.6.2 Display Features

The Redux GUI displays images for quality analysis and display (QAD) in the DS9 FITS viewer. DS9 is a standalone image display tool with an extensive feature set. See the SAO DS9 site (<http://ds9.si.edu/>) for more usage information.

After each pipeline step completes, Redux may load the produced images into DS9. Some display options may be customized directly in DS9; some commonly used options are accessible from the Redux interface, in the **Data View** tab ([Figure 48](#)).

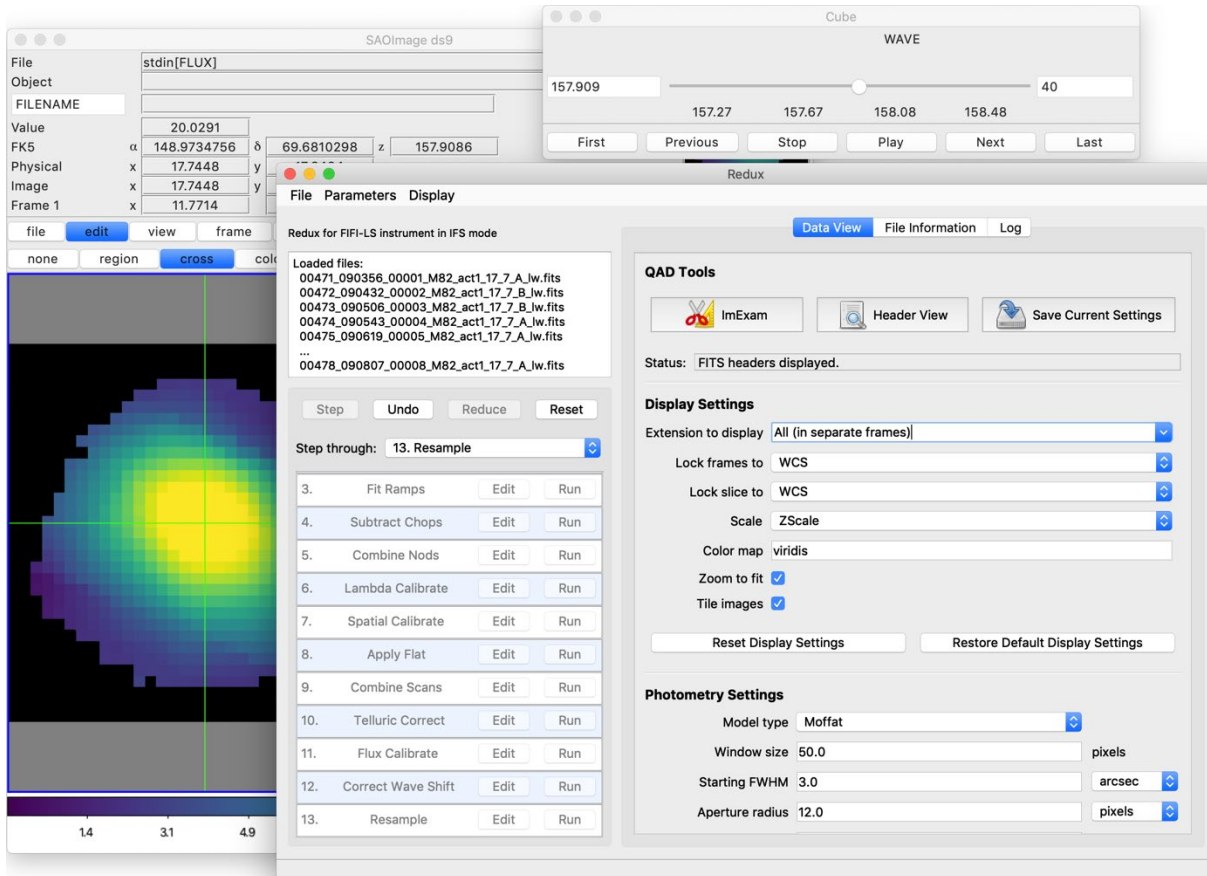


**Figure 48** *Data viewer settings and tools.*

From the Redux interface, the **Display Settings** can be used to:

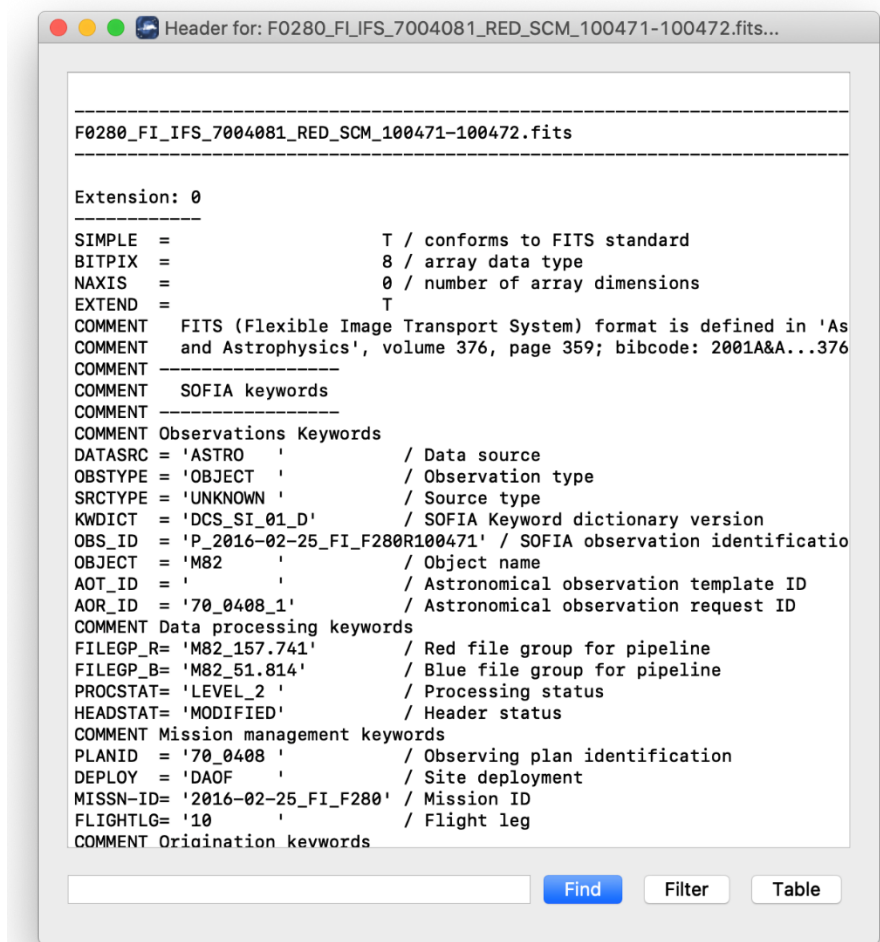
- Set the FITS extension to display (**First**, or edit to enter a specific extension), or specify that all extensions should be displayed in a cube or in separate frames.
- Lock individual frames together, in image or WCS coordinates.
- Lock cube slices for separate frames together, in image or WCS coordinates.
- Set the image scaling scheme.
- Set a default color map.
- Zoom to fit image after loading.
- Tile image frames, rather than displaying a single frame at a time.

Changing any of these options in the Data View tab will cause the currently displayed data to be reloaded with the new options. Clicking **Reset Display Settings** will revert any edited options to the last saved values. Clicking **Restore Default Display Settings** will revert all options to their default values.

In the **QAD Tools** section of the **Data View** tab, there are several additional tools available. Clicking the **ImExam** button (scissors icon) launches an event loop in DS9. After launching it, bring the DS9 window forward, then use the keyboard to perform interactive analysis tasks:

- Type ‘a’ over a source in the image to perform photometry at the cursor location.
- Type ‘p’ to plot a pixel-to-pixel comparison of all frames at the cursor location.
- Type ‘s’ to compute statistics and plot a histogram of the data at the cursor location.
- Type ‘c’ to clear any previous photometry results or active plots.
- Type ‘h’ to print a help message.
- Type ‘q’ to quit the ImExam loop.

The photometry settings (the image window considered, the model fit, the aperture sizes, etc.) may be customized in the **Photometry Settings**. Plot settings (analysis window size, shared plot axes, etc.) may be customized in the **Plot Settings**. After modifying these settings, they will take effect only for new apertures or plots (use ‘c’ to clear old ones first). For the display settings, the reset button will revert to the last saved values and the restore button will revert to default values. For the pixel-to-pixel and histogram plots, if the cursor is contained within a previously defined DS9



```

Header for: F0280_FI_IFS_7004081_RED_SCM_100471-100472.fits...

-----
F0280_FI_IFS_7004081_RED_SCM_100471-100472.fits
-----

Extension: 0
-----
SIMPLE =                T / conforms to FITS standard
BITPIX =                8 / array data type
NAXIS =                 0 / number of array dimensions
EXTEND =                T
COMMENT  FITS (Flexible Image Transport System) format is defined in 'As
COMMENT  and Astrophysics', volume 376, page 359; bibcode: 2001AJ...376
COMMENT  -----
COMMENT  SOFIA keywords
COMMENT  -----
COMMENT  Observations Keywords
DATASRC = 'ASTRO'      / Data source
OBSTYPE = 'OBJECT'    / Observation type
SRCTYPE = 'UNKNOWN'   / Source type
KWDICT = 'DCS_SI_01_D' / SOFIA Keyword dictionary version
OBS_ID = 'P_2016-02-25_FI_F280R100471' / SOFIA observation identification
OBJECT = 'M82'        / Object name
AOT_ID = '            / Astronomical observation template ID
AOR_ID = '70_0408_1'  / Astronomical observation request ID
COMMENT  Data processing keywords
FILEGP_R= 'M82_157.741' / Red file group for pipeline
FILEGP_B= 'M82_51.814' / Blue file group for pipeline
PROCSTAT= 'LEVEL_2'   / Processing status
HEADSTAT= 'MODIFIED'  / Header status
COMMENT  Mission management keywords
PLANID = '70_0408'    / Observing plan identification
DEPLOY = 'DAOF'       / Site deployment
MISSN-ID= '2016-02-25_FI_F280' / Mission ID
FLIGHTLG= '10'        / Flight leg
COMMENT  Origination keywords

```

Figure 49 QAD FITS header viewer.

region (and the `regions` package is installed), the plot will consider only pixels within the region. Otherwise, a window around the cursor is used to generate the plot data. Setting the window to a blank value in the plot settings will use the entire image.

Clicking the **Header** button (magnifying glass icon) from the **QAD Tools** section opens a new window that displays headers from currently loaded FITS files in text form (Figure 49). The extensions displayed depend on the extension setting selected (in **Extension to Display**). If a particular extension is selected, only that header will be displayed. If all extensions are selected (either for cube or multi-frame display), all extension headers will be displayed. The buttons at the bottom of the window may be used to find or filter the header text or generate a table of header keywords. For filter or table display, a comma-separated list of keys may be entered in the text box.

Clicking the **Save Current Settings** button (disk icon) from the **QAD Tools** section saves all current display and photometry settings for the current user. This allows the user's settings to persist across new Redux reductions, and to be loaded when Redux next starts up.

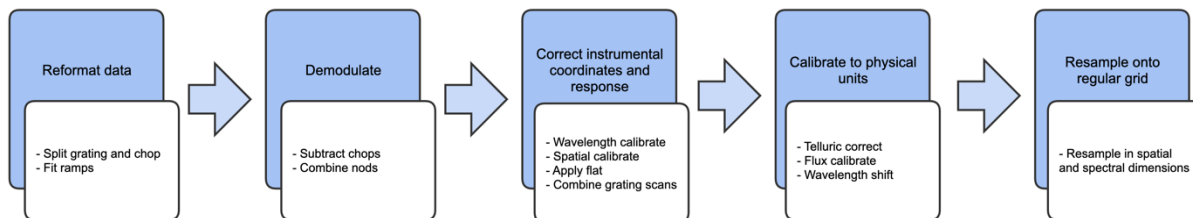


Figure 50 *FIFI-LS data reduction flowchart.*

### 4.6.3 Descriptions of Key Parameters

FIFI-LS data reduction with Redux follows the data reduction flowchart given in Figure 50. At each step, Redux attempts to automatically determine the correct action, given the input data and default parameters, but each step can be customized as needed. Some key parameters to note are listed below:

#### Check Headers

- Abort reduction for invalid headers: By default, Redux will halt the reduction if the input header keywords do not meet requirements. Uncheck this box to attempt the reduction anyway.

#### Fit Ramps

- Signal-to-noise threshold: This value defines the signal-to-noise cut-off to flag a ramp as bad and ignore it. Set to -1 to skip the signal-to-noise cut.
- Combination threshold (sigma): This value defines the rejection threshold for the robust mean combination of the ramp slopes. Set higher to reject fewer ramps, lower to reject more.

- **Bad pixel file:** By default, the pipeline looks up a bad pixel mask in `fifs/data/badpix_files`. To override the default mask, use this parameter to select a different text file. The file must be an ASCII table with two columns: the spaxel number (1-25, numbered left to right in displayed array), and the spexel number (1-16, numbered bottom to top in displayed array). This option may be used to block a bad spaxel for a particular observation, by entering a bad pixel for every spexel index in a particular spaxel.
- **Remove 1st 2 ramps:** Select to remove the first two ramps. This is on by default. This option has no effect if there are fewer than three ramps per chop.
- **Subtract bias:** If set, the value from the open zeroth spexel will be subtracted before fitting.
- **Threshold for grating instability:** Threshold in sigma for allowed ramp-averaged deviation from the expected grating position. Set to -1 to turn off filtering.

### Combine Nods

- **Method for combining off-beam images:** For C2NC2 only: ‘nearest’ takes the closest B nod in time, ‘average’ will mean-combine before and after B nods, and ‘interpolate’ will linearly interpolate before and after B nods to the A nod time. For OTF mode data, the B nods are interpolated to the time of each scan position.
- **Propagate off-beam image instead of on-beam:** If selected, B beams will be treated as if they were A beams for all subsequent reductions. That is, the map will be produced at position B instead of A. All other filenames and header settings will remain the same, so use it with caution. This option is mostly used for testing purposes.

### Spatial Calibrate

- **Rotate by detector angle:** By default, Redux rotates the data by the detector angle to set North up and East to the left in the final map. Deselect this box to keep the final map in detector coordinates.
- **Flip RA/Dec sign convention (+, -, or default):** For most data, the sign convention of the DLAM\_MAP and DBET\_MAP header keywords, which define the dither offsets, is determined automatically (parameter value “default”). Occasionally, for peculiar observations, these keywords may need their signs flipped, or used as is (no flip). This is usually determined by inspection of the results of the Resample step.

### Apply Flat

- **Skip flat correction:** Select this option to skip flat fielding the data. This option is mostly used for testing purposes.
- **Skip flat error propagation:** Deselect this option to propagate the systematic flat correction error in the flux error plane. This option is not currently recommended; the systematic error is stored in the CALERR keyword instead.

### Combine Scans

- **Correct bias offset:** Select this option to subtract an overall bias offset between the individual grating scans.

### Telluric Correct

- Skip telluric correction: Select to skip correcting the data for telluric absorption. This option is mostly used for testing.
- ATRAN directory: Use this option to select a directory containing ATRAN FITS files. This must be set to use water vapor values for telluric correction.
- Cutoff value: Modify to adjust the transmission fraction below which the telluric-corrected data will be set to NaN.
- Use WV values: Select to use water vapor values from the header (keyword WVZ\_OBS) to select the ATRAN file to apply. This option will have no effect unless the ATRAN directory is set to a location containing ATRAN files derived for different PWV values.

### Flux Calibrate

- Skip flux calibration: Select to skip flux calibration of the data. The flux will remain in instrumental units (ADU/sec), with PROCSTAT=LEVEL\_2. This option is mostly used for testing.
- Response file: Use this option to select a FITS file containing an instrumental response spectrum to use in place of the default file on disk.

### Correct Wave Shift

- Skip wavelength shift correction: Select to skip applying the correction to the wavelength calibration due to barycentric velocity. In this case, both telluric-corrected and uncorrected cubes will be resampled onto the original wavelengths. This option is mostly used for testing.

### Resample

- General parameters
  - Use parallel processing: If not set, data will be processed serially. This will likely result in longer processing times, but smaller memory footprint during processing.
  - Maximum cores to use: Specify the maximum cores to use, in the case of parallel processing. If not specified, the maximum is the number of available cores, minus 1.
  - Check memory use during resampling: If set, memory availability will be checked before processing, and the number of processes will be modified if necessary. If not set, processing is attempted with the maximum number of cores specified. Use with caution, as in some conditions, unsetting this option may result in software or computer crashes.
  - Skip coadd: If selected, a separate flux cube will be made from each input file, using the interpolation algorithm. This option is useful for identifying bad input files.
  - Interpolate instead of fit: If set, an alternate resampling algorithm will be used, rather than the local polynomial surface fits. This option may be preferable for data with small dither offsets; it is not recommended for large maps.



- Weight by errors: If set, local fits will be weighted by the flux errors, as calculated by the pipeline.
- Fit rejection threshold (sigma): If the fit value is more than this number times the standard deviation away from the weighted mean, the weighted mean is used instead of the fit value. This parameter is used to reject bad fit values. Set to -1 to turn off.
- Positive outlier threshold (sigma): Sets the rejection threshold for the input data, in sigma. Set to -1 to turn off.
- Negative outlier threshold (sigma): If non-zero, sets a separate rejection threshold in sigma for negative fluxes, to be used in a first-pass rejection. Set to -1 to turn off.
- Append distance weights to output file: If set, distance weights calculated by the resampling algorithm will be appended to the output FITS file. This option is primarily used for testing.
- Skip computing the uncorrected flux cube: If set, the uncorrected flux data will be ignored. This option is primarily for faster testing and/or quick look when the full data product is not required.
- Scan resampling parameters
  - Use scan reduction before resampling: If set, an iterative scan reduction will be performed to attempt to remove residual correlated gain and noise before resampling.
  - Save intermediate scan product: If set, the scan product will be saved to disk as a FITS file, for diagnostic purposes.
  - Scan options: Parameters to pass to the scan reduction. Enter as key=value pairs, space separated.
- Spatial resampling parameters
  - Create map in detector coordinates: If set, data are combined in arcsecond offsets from the base position, rather than in sky coordinates. If not set, detector coordinates are used for non-sidereal targets and sky coordinates otherwise.
  - Spatial oversample: This parameter controls the resolution of the output spatial grid, with reference to the assumed FWHM at the observed wavelength. The value is given in terms of pixels per reference FWHM for the detector channel used.
  - Output spatial pixel size (arcsec): This parameter directly controls the resolution of the output spatial grid. If set, this parameter overrides the spatial oversample parameter. For BLUE data, the default value is 1.5 arcsec; for RED data, it is 3.0 arcsec.
  - Spatial surface fit order: This parameter controls the order of the surface fit to the spatial data at each grid point. Higher orders give more fine scale detail but are more likely to be unstable. Set to zero to do a weighted mean of the nearby data.

- Spatial fit window: This parameter controls how much data to use in the fit at each grid point. It is given in terms of a factor times the average spatial FWHM. Higher values will lead to more input data being considered in the output solution, at the cost of longer processing time. Too-low values may result in missing data (holes) in the output map.
- Spatial smoothing radius: Set to the fraction of the fit window to use as the radius of the distance-weighting Gaussian. Lowering this value results in finer detail for the same input fit window. Too-low values may result in noisy output data; too high values effectively negate the distance weights.
- Spatial edge threshold: Specifies the threshold for setting edge pixels to NaN. Set lower to block fewer pixels.
- Adaptive smoothing algorithm: If ‘scaled’, the size of the smoothing kernel is allowed to vary, to optimize reconstruction of sharply peaked sources. If ‘shaped’, the kernel shape and rotation may also vary. If ‘none’, the kernel will not vary.
- Spectral resampling parameters
  - Spectral oversample: This parameter controls the resolution of the output spectral grid. The value is given in terms of pixels per reference spectral FWHM at the central wavelength of the observation.
  - Output spectral pixel size ( $\mu\text{m}$ ): This parameter directly controls the resolution of the output spectral grid. If set, this parameter overrides the spatial oversample parameter. It does not have a default value.
  - Spectral surface fit order: This parameter controls the order of the surface fit to the spectral data at each grid point.
  - Spectral fit window: This parameter controls how much data to use in the fit at each wavelength grid point. It is given in terms of a factor times the average spatial FWHM. Higher values will lead to more input data being considered in the output solution, at the cost of longer processing time. Too-low values may result in missing data (holes) in the output map.
  - Spectral smoothing radius: Set to the fraction of the fit window to use as the radius of the distance-weighting Gaussian, in the wavelength dimension.
  - Spectral edge threshold: Specifies the threshold for setting edge pixels to NaN, in the wavelength dimension. Set lower to block fewer pixels.

### Make Spectral Map

- Skip making the preview image: If set, no preview image (PNG file) will be produced.
- Extension to map: Extension name to display in the output image. This is typically ‘FLUX’ in the first extension, but for some cubes, ‘UNCORRECTED\_FLUX’ may be more appropriate.
- Method for selecting spectral slice: May be ‘reference’ or ‘peak’. If set to ‘reference’, the G\_WAVE\_B or G\_WAVE\_R keys are used to identify the reference wavelength. The nearest wavelength slice to the reference wavelength will be used as the spectral slice for

the image. For the ‘peak’ method, the flux cube is smoothed by a couple of pixels, then the highest S/N voxel is used to select the spectral slice for the image.

- Method for selecting spatial point: May be ‘reference’ or ‘peak’. If set to ‘reference’, the OBSRA and OBSDEC keys are used to identify the spatial point for the displayed spectrum. For the ‘peak’ method, the peak flux in the selected spectral slice is used to select the spatial point.
- Override wavelength slice: Manually specify the wavelength slice (zero-indexed) for the image.
- Override spatial point: Manually specify the spatial index for the spectrum, as ‘x,y’, zero-indexed.
- Fraction of outer wavelengths to ignore: Used with method = ‘peak’. Set to 0 to include all wavelengths in calculating signal peak. Set to a fraction less than 1 to exclude wavelengths at the beginning and end of the cube.
- Color map: Color map for the output PNG image. Any valid Matplotlib name may be specified.
- Flux scale for image: A low and high percentile value, used for scaling the spectral image, e.g. [0,99].
- Number of contours: Number of contour levels to be over-plotted on the image. Set to 0 to turn off contours.
- Contour color: Color for the contour lines. Any valid Matplotlib color name may be specified.
- Filled contours: If set, contours will be filled instead of overlaid.
- Overlay grid: If set, a coordinate grid will be overlaid.
- Beam marker: If set, a beam marker will be added to the plot.
- Overplot transmission: If set, the atmospheric transmission spectrum will be displayed in the spectral plot.
- Flux scale for spectral plot: Specify a low and high percentile value for the spectral flux scale, e.g. [0, 100]. If set to [0, 100], Matplotlib defaults are used.
- Watermark text: If set to a non-empty string, the text will be added to the lower-right of the image as a semi-transparent watermark.

### 4.6.4 Data Quality Assessment

After the pipeline has been run on a set of input data, the output products should be checked to ensure that the data has been properly reduced. Data quality and quirks can vary widely across individual observations, but the following general guidelines give some strategies for approaching quality assessment for FIFI-LS data.

- Check the output to the log file (usually called *redux\_[date]\_[time].log*), written to the same directory as the output files. Look for messages marked ERROR or WARNING. The log will also list every parameter used in the pipeline steps, which may help disambiguate the parameters as actually run for the pipeline.
- Check that the expected files were written to disk. There should, at a minimum, be a scan-combined file (*SCM*), a flux-calibrated file (*CAL*), and a resampled file (*WXY*).
- Look at each plane of the reduced image in the *WXY* file. Check that the resampling seems to have completed successfully: there should not be excessive holes in the map, or bad pixels away from the edges of the image. If there are, the spatial resampling may need to be redone with modified parameters.
- Look at the spectra for a sampling of spatial pixels in the *WXY* file. Check that there are no sudden dropouts or other discontinuities in the spectrum that are not associated with poor atmospheric transmission. If there are such discontinuities, the wavelength resampling may need to be redone with modified parameters.

### 4.7 PRODUCTS

#### 4.7.1 Grouping LEVEL\_1 Files for Processing

Table 11: Keywords and Their Data Types That Must Match to be Combined into a Final Map

Keyword	Data Type	Match Criterion
<b>OBSTYPE</b>	STR	Exact
<b>DETCAN</b>	STR	Exact
<b>DICHROIC</b>	INT	Exact
<b>NODSTYLE</b>	STR	Exact
<b>PLANID</b>	STR	Exact
<b>FILEGPID</b>	STR	Exact
<b>AOR-ID (optional)</b>	STR	Exact

FIFI-LS observations of a single object may dither in wavelength and/or in space. It is common to use a set of FIFI-LS observations to map out large regions of diffuse emission in a few small wavelength regions, but it is also common to use FIFI-LS to take a set of observations of a compact source over a wide range of wavelengths. As such, observations cannot be split on the central wavelength or base positions. Grouping relies on a keyword, `FILEGPID`, which defines a set of observations that should be reduced together to produce one final spectral map. In addition, however, observations must always be separated by detector channel, dichroic setting, nodding style (symmetric vs. asymmetric), observation type (source vs. sky flat), and the observational program ID. It may also be desirable to group files by the observation ID (AOR-ID), but this is

considered optional. This is since, because FIFI-LS incorporates a dichroic, different AORs can have the same grating setting for one of the two detectors. In such cases, the data sets with the same settings should be combined even though the AORs are different. All these requirements together define a set of FITS keywords that must match for a group of input files to be reduced together (see [Table 12](#)).

### 4.7.2 Pipeline Files

FIFI-LS output files from Redux are named according to the convention:

F[####]\_FI\_IFS\_[AOR-ID]\_[CHANNEL]\_[File-Code]\_[FN1-FN2].fits

where [####] is the four-digit SOFIA flight number, FI is the instrument identifier, IFS specifies that it is integral field spectroscopy data, [AOR-ID] is the AOR identifier for the observation, [CHANNEL] is either BLU or RED, [File-Code] is three letters identifying the product type (listed in [Table 13](#)), and [FN1] is the file number from that flight corresponding to a single input file used to generate the output file. [FN1-FN2] is used if there are multiple input files for a single output file, where FN1 is the file number of the first input file and FN2 is the file number of the last input file. Note that in some cases “pattern crashes” occur during flight which resets the file number counter and may cause FN2 to be less than FN1. These files have already been largely removed from the archive and should not be run through the pipeline as they have corrupted data.

[Table 13](#) lists all intermediate products generated by Redux for FIFI-LS, in the order in which they are produced. The product type is stored in the primary FITS header of the file, under the keyword PRODTYPE. By default, the *scan\_combined*, *flux\_calibrated*, and *resampled* products are saved.

As a last step, the pipeline additionally produces an image in PNG format, intended to provide a quick look preview of the data contained in the final product. These auxiliary products may be distributed to observers separately from the FITS file products.

**Table 12: FIFI-LS Pipeline Steps and Products**

Step	Product Type	Process Status	File Code	Saved	Extensions
<b>Split Grating / Chop</b>	<i>grating_chop_split</i>	LEVEL_2	CP0, CP1	No	$N_{\text{scan}}$ image extensions: FLUX_Gi for $i=0 \dots N_{\text{scan}}-1$
<b>Fit Ramps</b>	<i>ramps_fit</i>	LEVEL_2	RP0, RP1	No	$2N_{\text{scan}}$ image extensions: FLUX_Gi, STDDEV_Gi for $i=0 \dots N_{\text{scan}}-1$
<b>Subtract Chops</b>	<i>chop_subtracted</i>	LEVEL_2	CSB	No	$2N_{\text{scan}}$ image extensions: FLUX_Gi, STDDEV_Gi for $i=0 \dots N_{\text{scan}}-1$
<b>Combine Nods</b>	<i>nod_combined</i>	LEVEL_2	NCM	No	$2N_{\text{scan}}$ image extensions: FLUX_Gi, STDDEV_Gi for $i=0 \dots N_{\text{scan}}-1$

Step	Product Type	Process Status	File Code	Saved	Extensions
<b>Wavelength Calibrate</b>	<i>wavelength_calibrated</i>	LEVEL_2	WAV	No	$3N_{\text{scan}}$ image extensions: FLUX_Gi, STDDEV_Gi, LAMBDA_Gi for $i=0\dots N_{\text{scan}}-1$
<b>Spatial Calibrate</b>	<i>spatial_calibrated</i>	LEVEL_2	XYC	No	$5N_{\text{scan}}$ image extensions: FLUX_Gi, STDDEV_Gi, LAMBDA_Gi, XS_Gi, YS_Gi, RA_Gi, DEC_Gi for $i=0\dots N_{\text{scan}}-1$
<b>Apply Flat</b>	<i>flat_fielded</i>	LEVEL_2	FLF	No	$7N_{\text{scan}}$ image extensions: FLUX_Gi, STDDEV_Gi, LAMBDA_Gi, XS_Gi, YS_Gi, RA_Gi, DEC_Gi, FLAT_Gi, FLATERR_Gi for $i=0\dots N_{\text{scan}}-1$
<b>Combine Scans</b>	<i>scan_combined</i>	LEVEL_2	SCM	Yes	7 image extensions: FLUX, STDDEV, LAMBDA, XS, YS, RA, DEC
<b>Telluric Correct</b>	<i>telluric_corrected</i>	LEVEL_2	TEL	No	11 image extensions: FLUX, STDDEV, UNCORRECTED_FLUX, UNCORRECTED_STDDEV, LAMBDA, XS, YS, RA, DEC, ATRAN, UNSMOOTHED_ ATRAN
<b>Flux Calibrate</b>	<i>flux_calibrated</i>	LEVEL_3	CAL	Yes	12 image extensions: FLUX, STDDEV, UNCORRECTED_FLUX, UNCORRECTED_STDDEV, LAMBDA, XS, YS, RA, DEC, ATRAN, RESPONSE, UNSMOOTHED_ ATRAN
<b>Correct Wave Shift</b>	<i>wavelength_shifted</i>	LEVEL_3	WSH	No	13 image extensions: FLUX, STDDEV, UNCORRECTED_



Step	Product Type	Process Status	File Code	Saved	Extensions
					FLUX, UNCORRECTED_STDDDEV, LAMBDA, UNCORRECTED_LAMBDA, XS, YS, RA, DEC, ATRAN, RESPONSE, UNSMOOTHED_ATRAN
<b>Spatial Resample</b>	<i>resampled</i>	LEVEL_4	WXY	Yes	13 image extensions: FLUX, ERROR, UNCORRECTED_FLUX, UNCORRECTED_ERROR, WAVELENGTH, X, Y, RA-TAN, DEC-TAN, TRANSMISSION, RESPONSE, EXPOSURE_MAP, UNSMOOTHED_TRANSMISSION

#### 4.8 TELLURIC CORRECTIONS

As an airborne observatory, SOFIA observations were carried out through a residual atmosphere with a transmission between 0% and ~98%, depending on the wavelength and the water vapor overburden. The wavelength dependence is due to the numerous absorption features in the atmosphere, primarily from water, CO<sub>2</sub>, and O<sub>3</sub> but also from other atmospheric constituents. The water vapor overburden is measured in terms of the precipitable water vapor (PWV), which is the integrated amount of water along the line of sight towards the target. This is typically expressed in units of height if all the water vapor along the line of sight were converted into liquid. At high altitudes where ground-based submillimeter observations are possible (~15 kft) the PWV is typically measured in millimeters, but at stratospheric altitudes where SOFIA flies (~41 kft) the PWV is typically measured in microns. From models of atmospheric transmission (e.g., [Lord 1992](#)), it has been shown that the characteristic shape and strength of these absorption lines depends strongly on the PWV.

Since FIFI-LS was an imaging spectrometer, accurate knowledge of the atmospheric transmission during observations was essential to achieving a good calibration. A typical atmospheric transmission spectrum as modeled with ATRAN ([Lord et al., 1992](#)) is shown in [Figure 51](#). The altitude was set to 39,000 ft (representing the lowest typical observing altitude for SOFIA) and the telescope elevation to 40°, the center of the 22°–58° range. The transmission curves correspond to

the highest (15.75  $\mu\text{m}$ ) and the lowest (3.5  $\mu\text{m}$ ) PWV values ever measured in our data sample at 39 Kft (usually the lowest altitude at which observations are taken). The relative offset between the curves clearly demonstrates the challenge for a quality atmospheric calibration. Note that certain wavelengths are more sensitive to changes in PWV, such as around the 135–140  $\mu\text{m}$  region. The rest-wavelength of the [CII] 157  $\mu\text{m}$  line, a particularly important line for studying ISM conditions, is also marked. Similarly, the uncertainty in the correction for atmospheric absorption around the [OI] fine structure line at  $\sim 63$   $\mu\text{m}$  can easily reach a factor of 2. To complicate the issue, some spectral features may be Doppler-shifted to be near a telluric feature whose depth and width is highly dependent on the PWV.

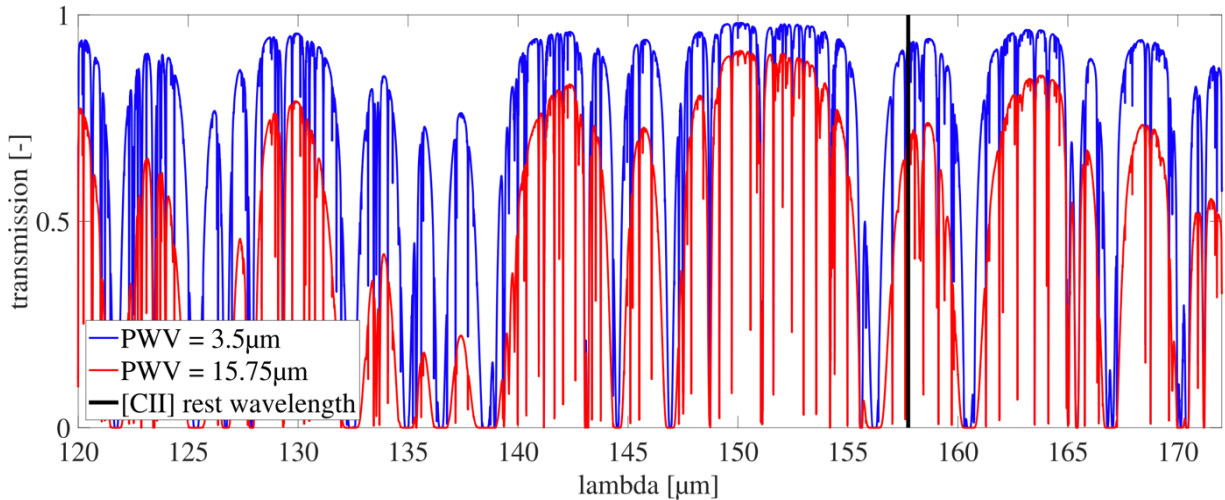


**Figure 51** *Atmospheric transmission between 120  $\mu\text{m}$  and 172  $\mu\text{m}$  modeled with ATRAN for a pressure altitude of 39,000 ft (about 11.89 km) and a telescope elevation of 40°. The two curves show the transmission for the highest (15.75  $\mu\text{m}$ ) and lowest (3.5  $\mu\text{m}$ ) PWV values measured by FIFI-LS at this altitude. The black line marks the rest wavelength of [CII].*

To determine the PWV during flight, the instrument took five exposures (per channel) of multiple telluric water lines in emission without any background subtraction (i.e., no chopping or nodding). A model of the atmospheric emission spectrum was then fitted to the observed spectrum to determine the PWV without the need to calibrate the data. [Figure 52](#) shows a typical telluric observation and best fit. Both channels of the instrument were configured to observe telluric water lines simultaneously to provide two independent measurements. About 10 measurements were carried out during each flight, usually while the telescope acquired the target. The observation wavelengths were chosen to coincide with telluric water lines that are sensitive in their relative amplitudes and widths to changes in PWV. The uncertainties from the fitting procedure are around 7%. More information on how these telluric observations were taken can be found in [Fischer et al. \(2021\)](#).

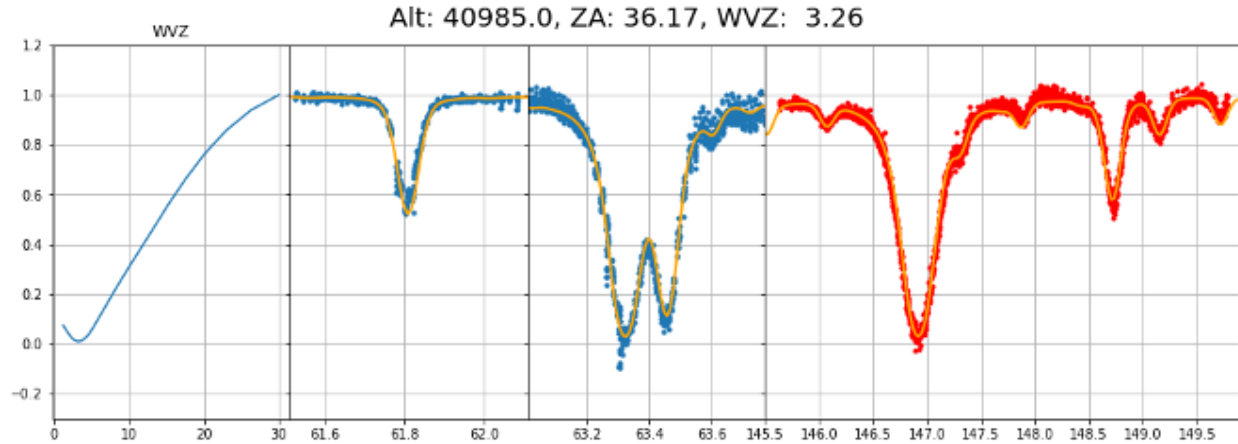


**Figure 52** An example fit to the atmospheric transmission for the blue and red arrays using ATRAN (right three plots), at an aircraft altitude of 41 kft and zenith angle 36 deg. The left plot shows the fit residuals as a function of the PWV, with a clear minimum at a PWV of 3.26  $\mu\text{m}$ .

Although these direct measurements of telluric features inform the general trends in data quality throughout a given flight (usually at the start and end of an observation leg), telluric correction during data reduction requires knowledge of any changes in the PWV throughout the observation leg. To do this, satellite based vertical PWV values are retrieved from the [European Climate Data Store](#) based on SOFIA’s geographical location, altitude, and time (all of which are present in the FITS headers). These PWV values are then corrected for their zenith angle and rescaled to the PWV as measured by FIFI-LS, using a scaling factor averaged over the whole flight. An example of this is shown in [Figure 53](#). This method was implemented since Flight 524, which corresponds to the beginning of the OC6M flight series. Prior to this, PWV values were not measured directly by FIFI-LS, so a scaling factor of 0.59 was used for OC2C through OC5I. This value was derived from the average of all scaling factors available at the time, from 43 flights between Flight 524 and Flight 723 (OC6M through OC8J) and is generally consistent to within  $\pm 0.04$  (1-sigma). Finally, to check the robustness of this scaling factor, the average of all 79 flights for which PWV was measured (OC6M through OC9T) was computed, and an average of 0.60 was found. [Figure 54](#) shows a histogram plot of all 43 scaling factors used to tie the satellite-derived PWV to the water vapor observed by FIFI-LS.

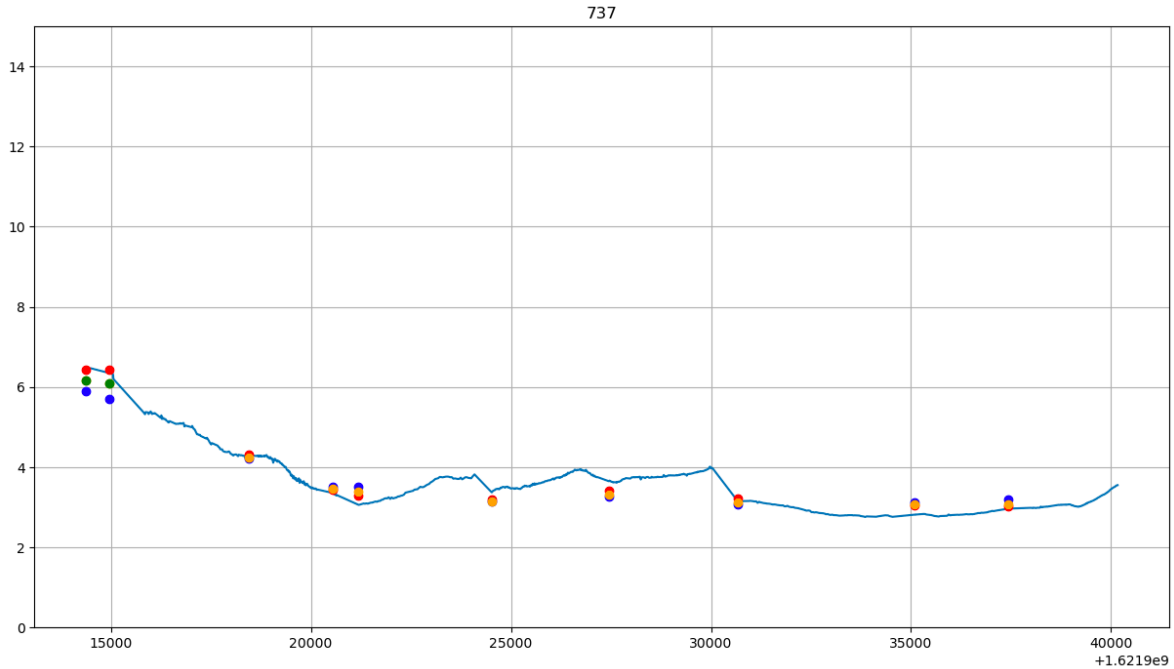


**Figure 53** The satellite derived PWV values (blue line) for Flight 737 scaled to match the PWV as measured by FIFI-LS (data points). The red and blue points correspond to the red and blue arrays respectively, the green and yellow points are the PWV values derived from the combined fit. For this flight, the scaling factor used was 0.56.

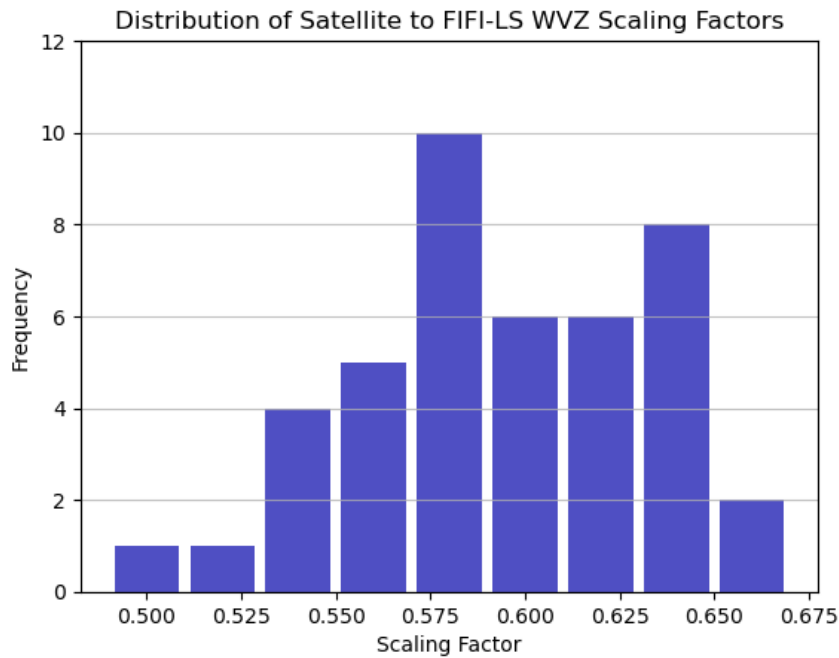


**Figure 54** Histogram plot of all the scaling factors for 43 flights between Flight 524 and Flight 723. The bins range from 0.49 to 0.67 with a bin size of 0.02.

Each raw FITS file generated by FIFI-LS contains the calculated water vapor values in the WVZ\_OBS keyword. To access the WVZ\_OBS value, in the directory of the FITS file enter the following command:

```
$ fitsheader NAME_OF_FITS_FILE.fits | grep WVZ_OBS
```

Note in the header there are two other keywords WVZ\_STA and WVZ\_END, which are water vapor values from the “Water Vapor Monitor” installed on SOFIA. Unfortunately, this monitor never worked and sometimes gave nonsensical values, so these two keywords should be ignored.

[Table 14](#) lists the satellite to FIFI-LS scaling factor used for each flight and are provided to reduce data assuming a different atmospheric model for converting the satellite water vapor into the FIFI-LS water vapor (see for example, Iserlohe et al. 2021, 2022). To determine which flight a FITS file was taken, enter the following command:

```
$ fitsheader NAME_OF_FITS_FILE.fits | grep MISSN-ID
```

To reobtain the satellite PWV values, divide the WVZ\_OBS value by corresponding factor in [Table 14](#).

**Table 13: The Multiplicative Scaling Factors Used to Convert the Satellite PWV into the FIFI-LS PWV (in the FITS Header) for Each Flight.**

Series	Flight	Factor	Series	Flight	Factor
<OC6M	<524	0.5905	OC8B	682	0.6114
OC6M	524	0.5605	OC8J	716	0.6108
OC6M	525	0.6507	OC8J	717	0.5846
OC6M	526	0.6567	OC8J	718	0.5753
OC6M	527	0.6439	OC8J	719	0.5660
OC6U	548	0.5671	OC8J	720	0.5773
OC6U	549	0.5791	OC8J	721	0.5420
OC6U	551	0.5811	OC8J	722	0.6301
OC7A	562	0.5983	OC8J	723	0.5847
OC7A	563	0.6429	OC8M	737	0.5555
OC7A	564	0.5085	OC8M	738	0.6420
OC7A	565	0.5967	OC8M	739	0.5519
OC7A	566	0.5940	OC8M	740	0.5839
OC7A	567	0.5740	OC8M	741	0.5708
OC7A	568	0.5905	OC8M	742	0.6026
OC7A	569	0.5178	OC9I	803	0.6357
OC7A	570	0.5451	OC9I	804	0.6717
OC7A	571	0.5761	OC9I	805	0.6400
OC7A	572	0.5703	OC9I	806	0.6633

Series	Flight	Factor	Series	Flight	Factor
OC7A	573	0.6191	OC9I	807	0.6579
OC7H	631	0.5357	OC9I	808	0.6546
OC7H	632	0.5983	OC9I	809	0.6570
OC7H	633	0.5795	OC9I	810	0.6128
OC7H	634	0.6101	OC9I	811	0.6992
OC7H	635	0.6398	OC9I	812	0.6917
OC7H	636	0.6425	OC9I	813	0.6267
OC7H	637	0.5632	OC9L	839	0.5294
OC7H	638	0.6182	OC9L	840	0.5795
OC7H	639	0.6287	OC9M	842	0.5617
OC7H	640	0.6172	OC9M	843	0.5679
OC7L	662	0.6304	OC9M	844	0.6143
OC7L	663	0.6199	OC9M	845	0.6033
OC7L	664	0.5903	OC9M	846	0.6508
OC7L	665	0.5481	OC9M	847	0.6279
OC8B	676	0.5657	OC9M	848	0.5688
OC8B	677	0.6219	OC9T	905	0.5919
OC8B	678	0.6432	OC9T	906	0.6079
OC8B	679	0.6072	OC9T	907	0.5054
OC8B	680	0.6481	OC9T	908	0.5226
OC8B	681	0.6039	OC9T	909	0.5782

Figure 55 shows the relative frequency of the PWV as a function of both altitude and season, based on FIFI-LS flights out of Palmdale between 2018-2022. In general, the higher the altitude is, the lower the PWV becomes. Moreover, summertime tends to exhibit the largest variation in the measured PWV compared to winter.



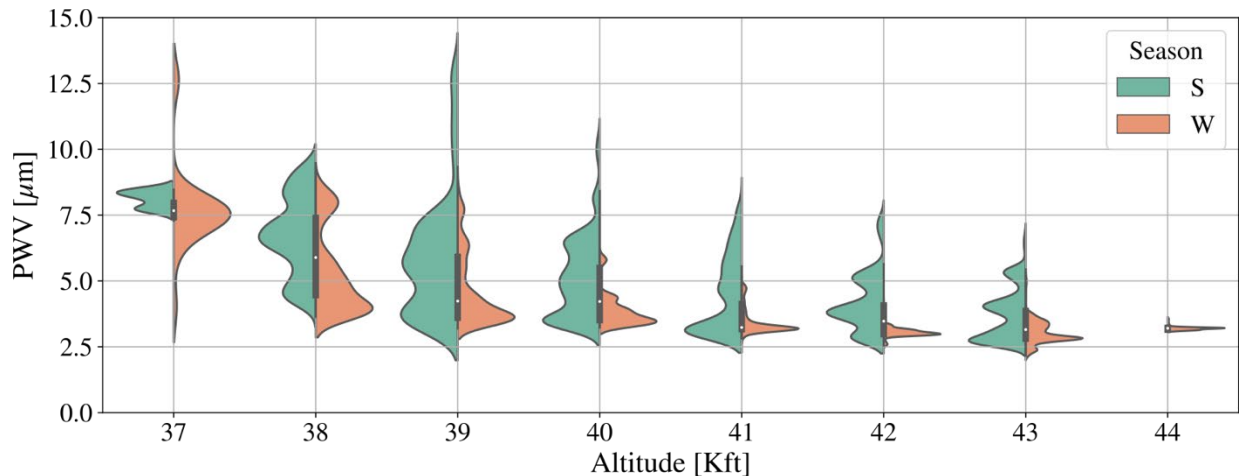


**Figure 55** The variation in PWV as a function of altitude and season (summer vs. winter) in the northern hemisphere. The data here represents flights out of Palmdale, CA between 2018-2022.

In `sospec` it is possible to change the water vapor correction applied to the data and is applied to the final image. However, it is preferable to run the data through the pipeline, especially if the data come from different flights with different observing conditions. This is because the pipeline will correct each frame separately with the correct water vapor and then recombine all the corrected data in the final cube.

## 4.9 ARTIFACTS

### 4.9.1 Vignetting

*Occurrence:* With elevation angles larger than  $67^\circ$  and smaller than  $32^\circ$  the illumination pattern of the array changes.

*Explanation:* The window's edge enters the telescope's field of view.

*Fix:* Reject files which are affected by vignetting.

### 4.9.2 Telluric Line Residuals

*Occurrence:* Close to deep telluric lines.

*Explanation:* The atmospheric model used to correct for the effects of the atmosphere can make a decent correction for atmospheric transmissions greater than 0.6.

*Fix:* Reject pixels with atmospheric transmission lower than 0.6.

### 4.9.3 Optical Ghosts

*Occurrence:* Very bright objects.

*Explanation:* Bright objects ( $>100$  Jy approximately) will produce negative flux (on the  $\sim 10\%$  level) in the sky immediately around the object.

*Fix:* Unfortunately, there is no fix, but most of this issue occurs on flux calibrators like Mars or the Jovian moons.

### 4.9.4 Corrupted Scan Files

*Occurrence:* Could happen during any observation.

*Explanation:* On occasion the FIFI-LS pattern generator routine would crash during observation and require restarting several processes that ran during the mission, resulting in corrupted scan files being saved.

*Fix:* The FIFI-LS instrument scientists have already removed these files from the archive, however if any more are found, the files should be removed from the reduction, in addition to any nod they were paired to.

### 4.10 SPECIAL CASES

In case of lines close to broad water vapor lines (i.e., for the [OI] 63  $\mu\text{m}$  line), the standard atmospheric correction will modify the shape of the line by overcorrecting the side of the line closer to the wing of the telluric line.

In this case, as a correction use the atmospheric transmission at the observed wavelength of the line. This is easy when using the “sospex” tool (see Appendix 101B) which has an option dedicated to this specific case. <https://github.com/darioflute/sospex>

### 5. SCIENTIFIC RESULTS

FIFI-LS on SOFIA played a significant role in investigations of star formation (primarily massive) and the interstellar medium in both our own galaxy and external galaxies. With its sensitivity, the latter topic was the prime capability of FIFI-LS on SOFIA. The spatial resolution of FIFI-LS was a huge improvement over available data from ISO ([Kessler et al. 1996](#)) and allowed better spatially resolved studies of extragalactic sources, such as M82. The key features that FIFI-LS observed are the bright far-infrared fine structure lines, e.g. [OI] 63  $\mu\text{m}$  and 146  $\mu\text{m}$ , [OIII] 52  $\mu\text{m}$  and 88  $\mu\text{m}$ , [NII] 122  $\mu\text{m}$ , [NIII] 57  $\mu\text{m}$ , [CII] 158  $\mu\text{m}$ , and molecular lines like CO lines between J=13–12 and J=38–37.

One typical application of FIFI-LS was obtaining maps of [CII] emission in nearby galaxies. Large maps of [CII] emission in nearby galaxies like M51 and NGC 6946 have been obtained in 10–15h of observing time. An area of 60 arcmin<sup>2</sup> could be integrated to reach a noise level of 10<sup>-17</sup> W/m<sup>2</sup> per spaxel (12 × 12 arcsec<sup>2</sup>) in about 15 hours of wall clock time. For smaller sources that fit into 1 × 1 arcmin<sup>2</sup> FOV of the red channel, deep integrations were easily possible. [CII] has been detected in sources with red shifts of up to 0.04 in wall clock times below two hours.

The oxygen lines [OI] at 63  $\mu\text{m}$  and 146  $\mu\text{m}$  were also frequently observed simultaneously with FIFI-LS as they play a major role in the analysis of photo-dissociation regions (PDRs). The line flux ratio provides constraints on the density and the UV flux in the region of interest. In addition, FIFI-LS observations of the relatively weak [OI] line at 146  $\mu\text{m}$  (typically a few times weaker than the [OI] 63  $\mu\text{m}$  line) were essentially a diagnostic of the conditions within the PDR, since the often-used line at 63  $\mu\text{m}$  can be optically thick for many sources. When mapping extended sources with multiple FOVs in the blue channel (30 × 30 arcsec<sup>2</sup>), the red channel got four times the integration time due to the overlap created by its larger size (1 × 1 arcmin<sup>2</sup>). This helped to detect the fainter line in the red channel. Thus, mapping both [OI] lines simultaneously with FIFI-LS was frequently carried out.

The line pair of [OIII] at 52  $\mu\text{m}$  and 88  $\mu\text{m}$  is very valuable for the analysis of HII regions since the ratio probes the electron density of both galactic and extragalactic sources. With the addition of the [NIII] line at 57  $\mu\text{m}$ , which FIFI-LS was also able access, it was also possible to probe the metallicity ([Nagao et al. 2011](#)). Furthermore, FIFI-LS observations of [OIII] 52  $\mu\text{m}$  and [NIII] 57  $\mu\text{m}$  were frequently obtained to augment existing data sets of other spectral lines obtained with PACS at similar spatial resolution.

#### 5.1 THE STRUCTURE OF A PDR: M17-SW

- Principle Investigator: *R. Klein (SOFIA Science Center, USRA)*
- Plan ID: 04\_0049

Publications:

- The Photodissociation and Ionization Fronts in M17-SW Localized with FIFI-LS on Board SOFIA, R. Klein et al. (2023), *ApJ* 945, 29  
DOI: [10.3847/1538-4357/acb823](https://doi.org/10.3847/1538-4357/acb823)

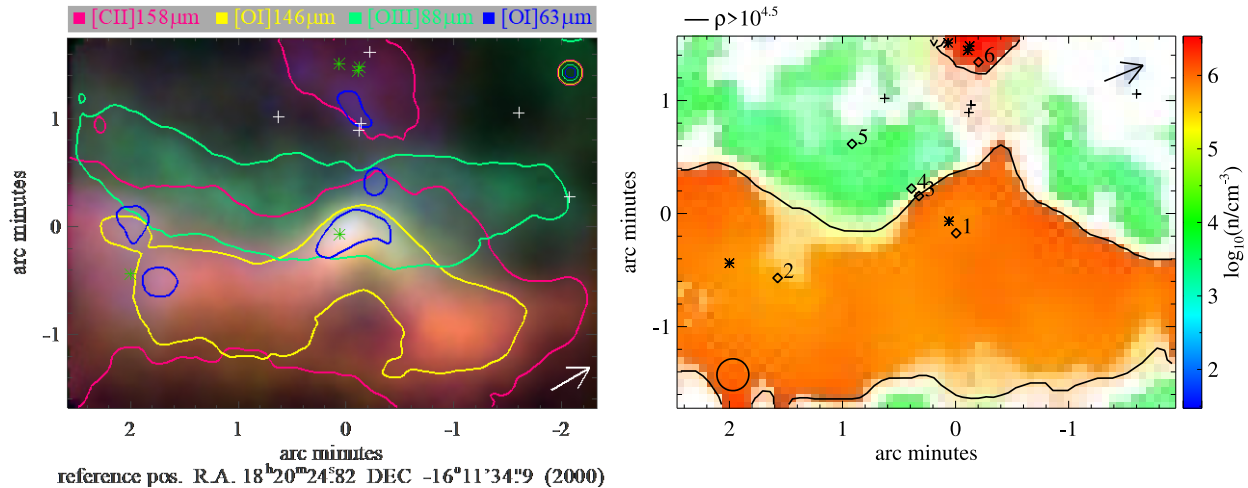


**Figure 56** From [Klein et al. \(2023\)](#). (Left) FIFI-LS line intensity maps showing the ionized and photodissociation region (PDR) layers traced by [OI]63  $\mu\text{m}$  (blue), [OIII]88  $\mu\text{m}$  (green), [OI]146  $\mu\text{m}$  (yellow), and [CII]158  $\mu\text{m}$  (magenta); the colored contours are at 50% of the peak intensity of the respective line. The circles in the upper right show the respective beam sizes. The blue symbols indicate the locations of the O-stars: stars for spectral types earlier than O9, crosses for types O9 and O9.5. The arrow points north. (Right) H-density derived by the PDR model. The color bars show the color scale used for values with an uncertainty less than 0.2 dex. The color fades with increasing uncertainties, becoming white for uncertainties larger than 1.25 dex. The contour traces the density jump.

The study of M17-SW is an example of FIFI-LS studying feedback in a Galactic region using the ability of FIFI-LS to map many different transitions efficiently. Tracing different species (ionized, neutral, and molecular) allows determining the physical conditions in the various parts of the PDR, the HII-region on one side, the molecular cloud on the other side, and the PDR in between.

Line intensity maps of the different species trace the PDR boundary with high spatial resolution. The diagnostic line pairs will allow analysis of the changing conditions along and across the PDR. Additionally, to the line intensities, FIFI-LS measured the continuum at these wavelengths allowing the study of spectral energy distribution and its changes with location in the PDR.

So far, the PDR has been analyzed with a one-dimensional PDR model ([Klein et al. 2023](#)), but the dataset is far from fully explored. [Figure 56](#) shows four line intensity maps created from the FIFI-LS data cubes obtained for program 04\_0049. The paper details how the line intensity maps were derived from the data cubes, which are available in the archive. The paper continues to analyze the line intensities of the PDR tracers with a one-dimensional PDR model to create a hydrogen density ([Figure 56](#), right) and a UV intensity map of the region. In M17-SW, the density map shows a clear jump in density. This jump lines up with other tracers of the transition from the HII region into the molecular cloud and indicates the location of the ionization and photodissociation front.

The density and UV intensity map of M17-SW is one of the first larger maps of the physical conditions of a PDR. Typically, in the past, only selected points in PDRs were modeled. With SOFIA and especially FIFI-LS, large areas of PDRs could be mapped in many transitions making such a large-scale analysis possible.

5.2 A COMPLETE VELOCITY RESOLVED 3-D [CII] MAP OF THE M51 GRAND-DESIGN SPIRAL GALAXY

- Principle Investigators: *J. Pineda (JPL) and J. Stutzki (Uni. Cologne)*
- Plan ID: 04\_0116

Publications:

- A SOFIA Survey of [C II] in the Galaxy M51: I. [C II] as a Tracer of Star Formation, Pineda et al. (2018), *ApJL*, 869, L30  
DOI: [10.3847/2041-8213/aaf1ad](https://doi.org/10.3847/2041-8213/aaf1ad)
- A SOFIA Survey of [C II] in the Galaxy M51: II. [C II] and CO Kinematics across the Spiral Arms, Pineda et al. (2020), *ApJ*, 900, 132  
DOI: [10.3847/1538-4357/abab0a](https://doi.org/10.3847/1538-4357/abab0a)

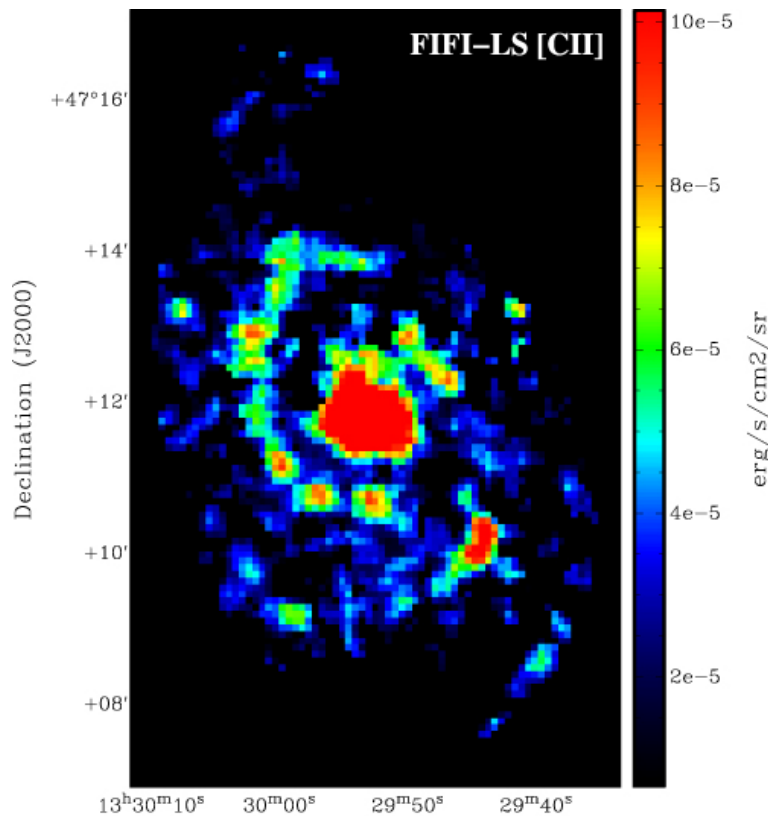


**Figure 57** From Pineda et al. (2018), the [CII] line intensity map created from the FIFI-LS data cube.

[Pineda et al. \(2018\)](#) used the fast-mapping capabilities of FIFI-LS to map the entire M51 and M51b galaxies in [CII] 156 $\mu$ m (Figure 57). The goal of the observations was to understand the impact of spiral density waves on the lifecycle of the interstellar medium and on star formation in galaxies. The [CII] line (in combination with the low-J CO lines and HI 21 cm) is a valuable tool to diagnose the physical state of the ISM.

In their paper, Pineda et al. compare the [CII] emission with the total far-infrared intensity (TIR) and star formation rate (SFR) surface density

maps of M51 within a variety of environments. They found that [CII] and the SFR surface density are well correlated in the central, spiral arm, and inter-arm regions and that the correlation is in good agreement with that found for a larger sample of nearby galaxies at kpc scales. The SFR and [CII] and TIR luminosities in M51 are dominated by the extended emission in M51's disk. The companion galaxy M51b, however, shows a deficit of [CII] emission compared with the TIR emission and inferred SFR surface density. A similar but less pronounced [CII] deficit is seen at the location of the black hole in M51's center. The observed [CII] deficit in M51b suggests that this galaxy represents a valuable laboratory in which to study the origin of the apparent [CII] deficit observed in ULIRGs.



5.3 CHARTING C+ IN A MILKY WAY ANALOG: NGC 7331

- Principle Investigator: *D. Fadda (SOFIA Science Center, USRA)*
- Plan ID: 75\_0045

Publications:

- [C II] Map of the Molecular Ring and Arms of the Spiral Galaxy NGC 7331, J. Sutter and D. Fadda (2022), *ApJ*, 926, 82  
DOI: [10.3847/1538-4357/ac4252](https://doi.org/10.3847/1538-4357/ac4252)

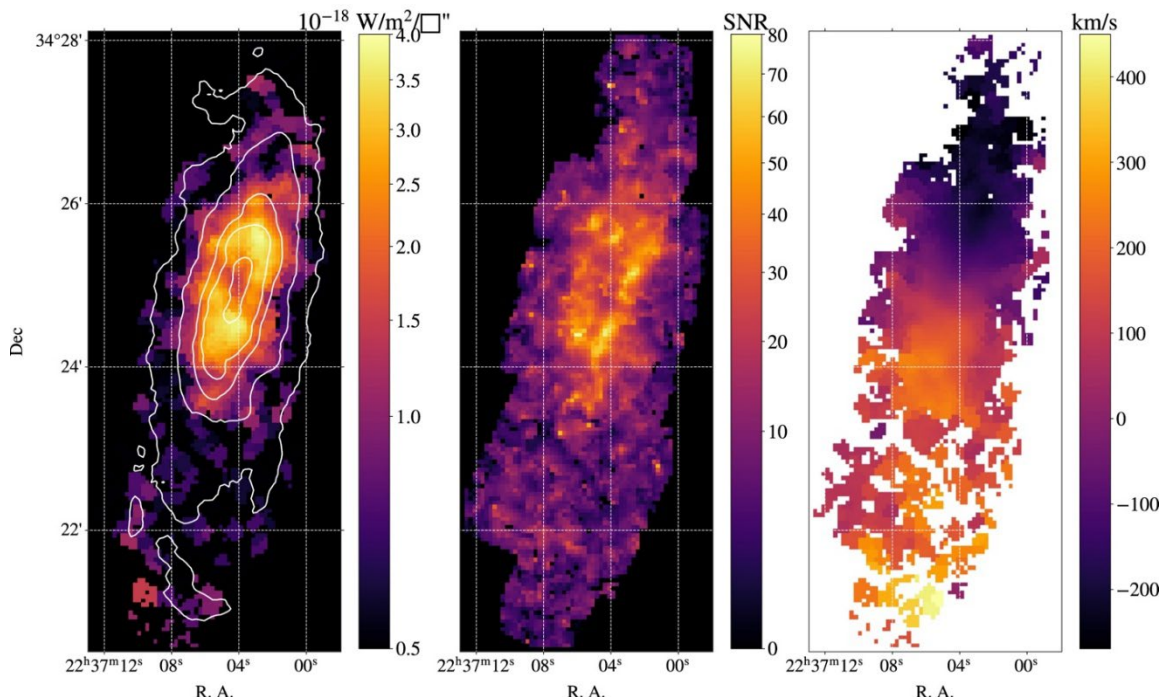


**Figure 58** [CII] map of NGC 7331. (Left) contours (0.4, 1.3, 3.4, and 6.4 MJy sr<sup>-1</sup>) of the PACS 160 μm image overlapped on the [CII] map to show the location of the ring and arms. (Middle) A map showing the S/N for the line fits of each pixel of the spectral cube. (Right) A velocity map assuming a systemic velocity of 800 km s<sup>-1</sup>. Pixels with S/N lower than 5 are left blank.

In this program, the efficient mapping capabilities of FIFI-LS were used to expand a [CII] map covering the central part of NGC 7331 obtained by Herschel/PACS to the whole galaxy (Figure 58).

[Sutter & Fadda \(2022a\)](#) take the map and compare it with archival UV–IR measurements enabling them to trace a variety of conditions of the interstellar medium (ISM) across the nucleus, molecular ring, spiral arms, and disk of NGC 7331. They find that the fraction of [CII] emitted from the neutral ISM rises with the distance from the center. In addition, by tracing the azimuthal variation of the neutral fraction, they can show how the observing perspective affects this measurement. The high inclination of NGC 7331 allows a glimpse into the internal walls of the molecular ring. There, young bright stars emit UV radiation causing more [CII] emission to be produced in the ionized gas. On the outer walls, opaque dust shrouds the rest of the ring, making the neutral medium the



dominant source of [CII] emission. Through spatial analysis comparing the [CII] emission to tracers of gas heating, [Sutter & Fadda \(2022a\)](#) investigate how the photoelectric heating efficiency varies throughout NGC 7331. Since the origin of [CII] emission has typically been studied in face-on galaxies, their results shed a new light on the interpretation of [CII] emission, especially when studying distant galaxies with unknown inclination.

### 6. REFERENCES

- Colditz, S. et al. (2014), Proceedings of the SPIE, Volume 9147, id. 91474S, doi: [10.1117/12.2055335](https://doi.org/10.1117/12.2055335)
- Colditz, S. et al., (2018), JAI, 7, 1840004, doi: [10.1142/S2251171718400044](https://doi.org/10.1142/S2251171718400044)
- Fadda, D. et al., (2016), A&A, 594, A90, doi: [10.1051/0004-6361/201527612](https://doi.org/10.1051/0004-6361/201527612)
- Fadda, D. & Chambers, E. T. (2018), in American Astronomical Society Meeting Abstracts, Vol. 231, American Astronomical Society Meeting Abstracts #231, 150.11, website: <https://ui.adsabs.harvard.edu/abs/2018AAS...23115011F/abstract>
- Fischer, Ch. et al., (2018), JAI, 7, 180003, doi: [10.1142/S2251171718400032](https://doi.org/10.1142/S2251171718400032)
- Fischer, Ch. et al., (2021), PASP, 133, id.055001, doi: [10.1088/1538-3873/abf1ca](https://doi.org/10.1088/1538-3873/abf1ca)
- Klein, R. et al., (2023), ApJ, 945, 29, doi: [10.3847/1538-4357/acb823](https://doi.org/10.3847/1538-4357/acb823)
- Kessler, M.F. et al., (1996), A&A, 315, L27, website: <https://articles.adsabs.harvard.edu/pdf/1996A%26A...315L..27K>
- Looney, L. et al., (2003), ApJ, 597, 628, doi: [10.1086/378225](https://doi.org/10.1086/378225)
- Mueller, T.G. et al. (2016), A&A, 588, A109, doi: [10.1051/0004-6361/201527371](https://doi.org/10.1051/0004-6361/201527371)
- Nagao, T. et al., (2011), A&A, 526, A149, doi: [10.1051/0004-6361/201015471](https://doi.org/10.1051/0004-6361/201015471)
- Orton et al., (2014), Icarus, 243, 494, doi: [10.1016/j.icarus.2014.07.010](https://doi.org/10.1016/j.icarus.2014.07.010)
- Raab et al., (2003), in Society of Photo-Optical Instrumentation Engineers (SPIE) Conference Series, Vol 4857, Airborne Telescope Systems II, ed. R. K. Melugin & H.-P. Roeser, 166, doi: [10.1117/12.458629](https://doi.org/10.1117/12.458629)
- Rebell et al., (2014), Proceedings of the SPIE, Volume 9147, id. 914735, doi: [10.1117/12.2055458](https://doi.org/10.1117/12.2055458)
- Rebell et al., (2016), Proceedings of the SPIE, Volume 9908, id. 99082D, doi: [10.1117/12.2231695](https://doi.org/10.1117/12.2231695)
- Rosenthal, D. et al., (2000), Proceedings of the SPIE, Volume 4014, 156, doi: [10.1117/12.389096](https://doi.org/10.1117/12.389096)
- Schweitzer M. et al., (2008), Proceedings of SPIE, Volume 7014, id. 70140Z, doi: [10.1117/12.787383](https://doi.org/10.1117/12.787383)
- Stankic, A. L., & Brouns, E. B. (2008), Vibrational Spectroscopy, 47, 66, doi: [10.1016/j.vibspec.2008.02.009](https://doi.org/10.1016/j.vibspec.2008.02.009)
- Sutter, J., & Fadda, D. (2022a), ApJ, 926, 82, doi: [10.3847/1538-4357/ac4252](https://doi.org/10.3847/1538-4357/ac4252)
- Sutter, J., & Fadda, D. (2022b), ApJ, 941, 47, doi: [10.3847/1538-4357/ac9d8f](https://doi.org/10.3847/1538-4357/ac9d8f)

APPENDIX

A. FIFI-LS FLIGHTS

Table 14: List of All FIFI-LS Flights

Flight Series	Flight Number	UT Date	FIFI Flight Number	Flight Name	Location
Commissioning	F150	2014-03-08	1		Palmdale, CA
Commissioning	F151	2014-03-10	2		Palmdale, CA
Commissioning	F152	2014-03-12	3		Palmdale, CA
OC2C	F160	2014-04-17	4		Palmdale, CA
OC2C	F161	2014-04-19	5		Palmdale, CA
OC2C	F162	2014-04-22	6		Palmdale, CA
OC2C	F163	2014-04-24	7		Palmdale, CA
OC2C	F164	2014-04-26	8		Palmdale, CA
OC3B	F199	2015-03-12	9		Palmdale, CA
OC3B	F200	2015-03-13	10		Palmdale, CA
OC3B	F201	2015-03-18	11		Palmdale, CA
OC3B	F202	2015-03-19	12		Palmdale, CA
OC3B	F203	2015-03-20	13		Palmdale, CA
OC3B	F204	2015-03-25	14		Palmdale, CA
OC3B	F205	2015-03-26	15		Palmdale, CA
OC3B	F206	2015-03-27	16		Palmdale, CA
OC3K	F246	2015-10-14	17		Palmdale, CA
OC3K	F247	2015-10-15	18		Palmdale, CA
OC3K	F248	2015-10-21	19		Palmdale, CA
OC3K	F249	2015-10-22	20		Palmdale, CA

Flight Series	Flight Number	UT Date	FIFI Flight Number	Flight Name	Location
OC3K	F250	2015-10-23	21		Palmdale, CA
OC3K	F251	2015-10-27	22		Palmdale, CA
OC3K	F252	2015-10-28	23		Palmdale, CA
OC3K	F253	2015-10-29	24		Palmdale, CA
OC4B	F280	2016-02-25	25		Palmdale, CA
OC4B	F281	2016-02-27	26		Palmdale, CA
OC4B	F282	2016-03-01	27		Palmdale, CA
OC4B	F283	2016-03-02	28		Palmdale, CA
OC4B	F284	2016-03-03	29		Palmdale, CA
OC4B	F285	2016-03-04	30		Palmdale, CA
OC4B	F286	2016-03-09	31		Palmdale, CA
OC4B	F287	2016-03-10	32		Palmdale, CA
OC4F	F310	2016-06-28	33		Christchurch, New Zealand
OC4F	F311	2016-06-29	34		Christchurch, New Zealand
OC4F	F312	2016-06-30	35		Christchurch, New Zealand
OC4F	F313	2016-07-01	36		Christchurch, New Zealand
OC4F	F314	2016-07-03	37		Christchurch, New Zealand
OC4F	F315	2016-07-04	38		Christchurch, New Zealand
OC4F	F316	2016-07-05	39		Christchurch, New Zealand
OC4F	F317	2016-07-06	40		Christchurch, New Zealand
OC5B	F378	2017-02-25	41	Bader	Palmdale, CA
OC5B	F379	2017-02-28	42	Benny	Palmdale, CA

Flight Series	Flight Number	UT Date	FIFI Flight Number	Flight Name	Location
OC5B	F380	2017-03-01	43	Barton	Palmdale, CA
OC5B	F381	2017-03-02	44	Betty	Palmdale, CA
OC5B	F382	2017-03-03	45	Bilko	Palmdale, CA
OC5B	F383	2017-03-07	46	Boris	Palmdale, CA
OC5B	F384	2017-03-08	47	Barney	Palmdale, CA
OC5B	F385	2017-03-09	48	Beverly	Palmdale, CA
OC5I	F422	2017-07-26	49	Ira	Christchurch, New Zealand
OC5I	F423	2017-07-27	50	Ingrid	Christchurch, New Zealand
OC5I	F424	2017-07-28	51	Ida	Christchurch, New Zealand
OC6M	F524	2018-11-06	52	Malcom	Palmdale, CA
OC6M	F525	2018-11-07	53	Maynard	Palmdale, CA
OC6M	F526	2018-11-08	54	Matilda	Palmdale, CA
OC6M	F527	2018-11-09	55	Mildred	Palmdale, CA
OC6U	F548	2019-02-27	56	Uhura	Palmdale, CA
OC6U	F549	2019-02-28	57	Uther	Palmdale, CA
OC6U	F550	2019-03-01	58	Ursula	Palmdale, CA
OC6U	F551	2019-03-02	59	Ulysses	Palmdale, CA
OC7A	F562	2019-05-01	60	Aaron	Palmdale, CA
OC7A	F563	2019-05-02	61	Abraham	Palmdale, CA
OC7A	F564	2019-05-03	62	Ackbar	Palmdale, CA
OC7A	F565	2019-05-04	63	Adam	Palmdale, CA
OC7A	F566	2019-05-07	64	Agnes	Palmdale, CA

Flight Series	Flight Number	UT Date	FIFI Flight Number	Flight Name	Location
OC7A	F567	2019-05-08	65	Ajax	Palmdale, CA
OC7A	F568	2019-05-09	66	Albert	Palmdale, CA
OC7A	F569	2019-05-10	67	Ali	Palmdale, CA
OC7A	F570	2019-05-14	68	Anastasia	Palmdale, CA
OC7A	F571	2019-05-15	69	Antonio	Palmdale, CA
OC7A	F572	2019-05-16	70	Audrey	Palmdale, CA
OC7A	F573	2019-05-17	71	Avery	Palmdale, CA
OC7H	F631	2019-10-30	72	Hadrien	Palmdale, CA
OC7H	F632	2019-10-31	73	Hamlet	Palmdale, CA
OC7H	F633	2019-11-01	74	Harold	Palmdale, CA
OC7H	F634	2019-11-02	75	Havey	Palmdale, CA
OC7H	F635	2019-11-05	76	Hector	Palmdale, CA
OC7H	F636	2019-11-06	77	Heidi	Palmdale, CA
OC7H	F637	2019-11-07	78	Helga	Palmdale, CA
OC7H	F638	2019-11-08	79	Hidalgo	Palmdale, CA
OC7H	F639	2019-11-13	80	Hodor	Palmdale, CA
OC7H	F640	2019-11-14	81	Howard	Palmdale, CA
OC7L	F662	2020-02-25	82	Leopold	Palmdale, CA
OC7L	F663	2020-02-26	83	Linus	Palmdale, CA
OC7L	F664	2020-02-27	84	Luther	Palmdale, CA
OC7L	F665	2020-02-28	85	Levi	Palmdale, CA
OC8B	F676	2020-08-18	86	Bertrand	Palmdale, CA



Flight Series	Flight Number	UT Date	FIFI Flight Number	Flight Name	Location
OC8B	F677	2020-08-20	87	Beverly	Palmdale, CA
OC8B	F678	2020-08-28	88	Bluto	Palmdale, CA
OC8B	F679	2020-09-01	89	Barney	Palmdale, CA
OC8B	F680	2020-09-02	90	Bertha	Palmdale, CA
OC8B	F681	2020-09-03	91	Benjamin	Palmdale, CA
OC8B	F682	2020-09-04	92	Barcley	Palmdale, CA
OC8J	F716	2021-04-13	93	Jacob	Palmdale, CA
OC8J	F717	2021-04-14	94	Jadzia	Palmdale, CA
OC8J	F718	2021-04-16	95	Jebediah	Palmdale, CA
OC8J	F719	2021-04-17	96	Janet	Palmdale, CA
OC8J	F720	2021-04-20	97	Jonas	Palmdale, CA
OC8J	F721	2021-04-21	98	Joseph	Palmdale, CA
OC8J	F722	2021-04-22	99	Juanita	Palmdale, CA
OC8J	F723	2021-04-23	100	Julius	Palmdale, CA
OC8M	F737	2021-05-25	101	Maddilyn	Palmdale, CA
OC8M	F738	2021-05-27	102	Matthew	Palmdale, CA
OC8M	F739	2021-05-28	103	Marvin	Palmdale, CA
OC8M	F740	2021-06-03	104	Mildred	Palmdale, CA
OC8M	F741	2021-06-04	105	Mario	Palmdale, CA
OC8M	F742	2021-06-05	106	Maxine	Palmdale, CA
OC9I	F803	2021-12-22	107	Ian	Palmdale, CA
OC9I	F804	2021-12-23	108	Ida	Palmdale, CA

Flight Series	Flight Number	UT Date	FIFI Flight Number	Flight Name	Location
OC9I	F805	2022-01-07	109	Irwin	Palmdale, CA
OC9I	F806	2022-01-08	110	Isaac	Palmdale, CA
OC9I	F807	2022-01-11	111	Ingrid	Palmdale, CA
OC9I	F808	2022-01-12	112	Igor	Palmdale, CA
OC9I	F809	2022-01-13	113	Isadora	Palmdale, CA
OC9I	F810	2022-01-14	114	Isabella	Palmdale, CA
OC9I	F811	2022-01-19	115	Isis	Palmdale, CA
OC9I	F812	2022-01-20	116	Ishmael	Palmdale, CA
OC9I	F813	2022-01-21	117	Ishi	Palmdale, CA
OC9L	F839	2022-03-15	118	Lucy	Palmdale, CA
OC9L	F840	2022-03-16	119	Linus	Palmdale, CA
OC9M	F842	2022-03-22	120	Marsha	Santiago, Chile
OC9M	F843	2022-03-23	121	Mario	Santiago, Chile
OC9M	F844	2022-03-24	122	Mabel	Santiago, Chile
OC9M	F845	2022-03-26	123	Mary	Santiago, Chile
OC9M	F846	2022-03-28	124	Milton	Santiago, Chile
OC9M	F847	2022-03-29	125	Merlin	Santiago, Chile
OC9M	F848	2022-03-30	126	Matilda	Santiago, Chile
OC9T	F905	2022-08-24	127	Tracy	Palmdale, CA
OC9T	F906	2022-08-25	128	Tyler	Palmdale, CA
OC9T	F907	2022-08-30	129	Tenzin	Palmdale, CA
OC9T	F908	2022-08-31	130	Tuvok	Palmdale, CA

Flight Series	Flight Number	UT Date	FIFI Flight Number	Flight Name	Location
OC9T	F909	2022-09-01	131	Tina	Palmdale, CA

### B. ANALYSIS TOOLS IN PYTHON: SOSPEX

Interactive GUI developed by D. Fadda in Python at the SOFIA Science Center.

It is available as an anaconda package (channel darioflute) or, as a repository, on github.

Website: <https://github.com/darioflute/sospex>

### C. ANALYSIS TOOLS IN IDL: FLUXER

Software developed by C. Iserlohe. It is available on request from the author.

Website: <http://www.ciserlohe.de/fluxer/fluxer.html>

### D. FIFI-LS REDUX

Below is a sample FIFI-LS Redux parameter override file in INI format. If present, the parameter value overrides the default defined by the FIFI-LS reduction object. If not present, the default value will be used. The parameters displayed here are the current default values.

```
# Redux parameters for FIFI-LS instrument in IFS mode
# Pipeline: FIFI_LS_REDUX v2_7_0
[1: checkhead]
    abort = True
[2: split_grating_and_chop]
    save = False
[3: fit_ramps]
    save = False
    parallel = True
    s2n = 10.0
    thresh = 5.0
    badpix_file = ""
    remove_first = True
    subtract_bias = True
    indpos_sigma = 3.0
[4: subtract_chops]
    save = False
[5: combine_nods]
```

```
save = False
b_nod_method = nearest
offbeam = False
[6: lambda_calibrate]
save = False
[7: spatial_calibrate]
    save = False
    rotate = True
    flipsign = default
[8: apply_static_flat]
save = False
    skip_flat = False
    skip_err = True
[9: combine_grating_scans]
    save = True
    bias = True
[10: telluric_correct]
save = False
skip_tell = False
atran_dir = ""
cutoff = 0.6
use_wv = False
[11: flux_calibrate]
save = True
skip_cal = False
response_file = ""
[12: correct_wave_shift]
save = False
skip_shift = False
[13: resample]
save = True
parallel = True
max_cores = ""
check_memory = True
skip_coad = False
interpolate = False
error_weighting = True
fitthresh = -1
postthresh = -1
negthresh = -1
append_weights = False
skip_uncorrected = False
scan_reduction = False
```

```

save_scan = False
scan_options = ""
detector_coordinates = False
xy_oversample = 5.0
xy_pixel_size = 1.5
  xy_order = 2
xy_window = 3.0
xy_smoothing = 1.0
xy_edge_threshold = 0.7
adaptive_algorithm = none
w_oversample = 8.0
w_pixel_size = ""
  w_order = 2
w_window = 0.5
w_smoothing = 0.25
w_edge_threshold = 0.5
[14: specmap]
skip_preview = False
extension = FLUX
slice_method = reference
point_method = peak
override_slice = ""
override_point = ""
ignore_outer = 0.2
colormap = plasma
scale = 0.25, 99.9
n_contour = 0
contour_color = gray
fill_contours = False
grid = False
beam = False
atran_plot = True
error_plot = True
spec_scale = 0, 100
watermark = ""

```

Sample FIFI-LS configuration file, located in *fifi-ls/data/header\_info/headerdef.dat*. Values marked with a Y in the *reqd?* column are keywords required to be present in input data. They must meet the type and range requirements listed for grouping and data reduction to be successful.

```

#
# This table lists keywords, allowed values, and defaults for
# all keywords to be written to output files. Keywords
# required to be present in input files for correct data
# processing are marked with a 'Y'. A '.' in min, max, or enum
# means no requirement. The combine column designates the
# algorithm to be used to calculate the value for the

```

```

# header of a product made from multiple input files.
#
# keyword reqd? default type combine min max enum
#-----
AIRSPEED N -9999. float first . . .
ALTI_END Y -9999. float last 0. 60000. .
ALTI_STA Y -9999. float first 0. 60000. .
AOR_ID N UNKNOWN string first . . .
AOT_ID N UNKNOWN string first . . .
ASSC_AOR N UNKNOWN string concatenate . . .
ASSC_MSN N UNKNOWN string concatenate . . .
ASSC_OBS N UNKNOWN string concatenate . . .
ATRNFIL N UNKNOWN string concatenate . . .
BDPXFIL N UNKNOWN string concatenate . . .
BGLEVL_A N -9999. float mean . . .
BGLEVL_B N -9999. float mean . . .
C_CHOPLN Y -9999 int first 7 256 .
C_SCHEM Y UNKNOWN string first . . 2POINT
CHOPPING Y T bool first . . .
CHPAMP1 N -9999. float first -1125 1125 .
CHPAMP2 N -9999. float first -1125 1125 .
CHPANG N -9999. float first -360. 360. .
CHPCRSYS N UNKNOWN string first . . TARF|ERF|SIRF
CHPFREQ Y -9999. float first 0.25 25. .
CHPPHASE N -9999 int first 0 1000 .
CHPPROF N UNKNOWN string first . . 2-POINT|3-POINT
CHPSYM N UNKNOWN string first . . .
CHPTIP N -9999. float first -301. 301. .
CHPTILT N -9999. float first -301. 301. .
CREATOR N UNKNOWN string first . . .
DATAQUAL N UNKNOWN string first . . NOMINAL|USABLE|TEST|PROBLEM|FAIL
DATASRC Y UNKNOWN string first . . .
ASTRO|CALIBRATION|LAB|TEST|OTHER|FIRSTPOINT
DATATYPE N UNKNOWN string first . . IMAGE|SPECTRAL|OTHER
DATE N UNKNOWN string first . . .
DATE-BEG N UNKNOWN string first . . .
DATE-END N UNKNOWN string last . . .
DATE-OBS Y UNKNOWN string first . . .
DBET_MAP Y -9999. float first -36000 36000 .
DEPLOY N UNKNOWN string first . . .
DETCAN Y UNKNOWN string first . . BLUE|RED
DETECTOR N UNKNOWN string first . . .
DETSIZE N UNKNOWN string first . . .
DICHROIC Y -9999 int first . . 105|130
DITHER N F bool first . . .
DLAM_MAP Y -9999. float first -36000 36000 .
DTHCRSYS N UNKNOWN string first . . TARF|ERF|SIRF
DTHINDEX N -9999 int default . . .
DTHNPOS N -9999 int first . . .
DTHOFFS N -9999. float first . . .
DTHPATT N UNKNOWN string first . . NONE|3-POINT|5-POINT|9-
POINT|CUSTOM
DTHXOFF N -9999. float first . . .
DTHYOFF N -9999. float first . . .
EQUINOX N -9999. float first . . .
EXPTIME Y -9999. float sum 0.02 1000 .
FBC-STAT N UNKNOWN string last . . FBC_OFF|FBC_QS|FBC_DY|FBC_ON
FILENAME Y UNKNOWN string first . . .
FILENUM N UNKNOWN string first . . .
FILEREV N UNKNOWN string first . . .
FLATFILE N UNKNOWN string concatenate . . .
FLIGHTLG N UNKNOWN string first . . .

```



FOCUS_EN	N	-9999.	float	last	-5000	5000	.			
FOCUS_ST	N	-9999.	float	first	-5000	5000	.			
G_CYC_B	Y	-9999	int	first	0	100	.			
G_CYC_R	Y	-9999	int	first	0	100	.			
G_ORD_B	Y	-9999	int	first	1	2	.			
G_PSDN_B	Y	-9999	int	first	0	100	.			
G_PSDN_R	Y	-9999	int	first	0	100	.			
G_PSUP_B	Y	-9999	int	first	0	100	.			
G_PSUP_R	Y	-9999	int	first	0	100	.			
G_STRT_B	Y	-9999	int	first	0	2098176	.			
G_STRT_R	Y	-9999	int	first	0	2098176	.			
G_SZDN_B	Y	-9999	int	first	0	20000	.			
G_SZDN_R	Y	-9999	int	first	0	20000	.			
G_SZUP_B	Y	-9999	int	first	-20000	20000	.			
G_SZUP_R	Y	-9999	int	first	-20000	20000	.			
GRDSPEED	N	-9999.	float	first	.	.	.			
HEADING	N	-9999.	float	first	.	.	.			
HEADSTAT	N	UNKNOWN	string	first	.	.	.			
ORIGINAL	UNKNOWN	CORRECTED	ERROR	MODIFIED	.	.	.			
IMAGEID	N	-9999	int	default	0	.	.			
INSTCFG	N	UNKNOWN	string	first	.	.	DUAL_CHANNEL			
INSTMODE	N	UNKNOWN	string	first	.	.	.			
SYMMETRIC_CHOP	ASYMMETRIC_CHOP	BRIGHT_OBJECT	SPECTRAL_SCAN	TOTAL_POWER	OTF_TP	.	.			
INSTRUME	Y	FIFI-LS	string	first	.	.	FIFI-LS			
KWDICT	N	UNKNOWN	string	first	.	.	.			
LASTREW	N	UNKNOWN	string	first	.	.	.			
LAT_END	N	-9999.	float	last	.	.	.			
LAT_STA	N	-9999.	float	first	.	.	.			
LON_END	N	-9999.	float	last	.	.	.			
LON_STA	N	-9999.	float	first	.	.	.			
MAPCRSYS	N	UNKNOWN	string	first	.	.	.			
EQUATORIAL	GALACTIC	ECLIPTIC	USER	.	.	.	.			
MAPINTX	N	-9999.	float	first	.	.	.			
MAPINTY	N	-9999.	float	first	.	.	.			
MAPXPOS	N	-9999	int	first	.	.	.			
MAPYPOS	N	-9999	int	first	.	.	.			
MAPPING	N	F	bool	first	.	.	.			
MCCSMODE	N	UNKNOWN	string	first	.	.	.			
MISSN-ID	Y	UNKNOWN	string	first	.	.	.			
NEXP	N	1	int	sum	0	.	.			
NODAMP	N	-9999.	float	first	.	.	.			
NODANGLE	N	-9999.	float	first	-360	360	.			
NODBEAM	Y	UNKNOWN	string	default	.	.	A B			
NODCRSYS	N	UNKNOWN	string	first	.	.	.			
ERF	ECRF	GALRF	TARF	FPIRF	FFIRF	WFIRF	SIRF	USER		
NODDING	Y	T	bool	first	.	.	.			
NODN	N	-9999	int	first	.	.	.			
NODPATT	Y	UNKNOWN	string	first	.	.	.			
NODSETL	N	-9999.	float	first	.	.	.			
NODSTYLE	Y	UNKNOWN	string	first	.	.	NMC C2NC2			
NODTIME	N	-9999.	float	first	.	.	.			
OBJECT	Y	UNKNOWN	string	first	.	.	.			
OBS_ID	Y	UNKNOWN	string	first	.	.	.			
OBSBET	N	-9999.	float	first	-90.	90.	.			
OBSDEC	N	-9999.	float	first	-90.	90.	.			
OBSERVER	N	UNKNOWN	string	first	.	.	.			
OBSLAM	N	-9999.	float	first	0.	360.	.			
OBSRA	N	-9999.	float	first	0.	24.	.			
OBSTYPE	Y	UNKNOWN	string	first	.	.	.			
OBJECT	STANDARD_FLUX	STANDARD_TELLURIC	STANDARD_WAVECAL	LAMP	FLAT	DARK	BIAS	SKY	BB	GAS
CELL	LASER	FOCUS_LOOP	.	.	.	.	.	.	.	.
OPERATOR	N	UNKNOWN	string	first	.	.	.			

ORIGIN	N	UNKNOWN	string	first	.	.	.
PIPELINE	N	UNKNOWN	string	first	.	.	.
PIPEVERS	N	UNKNOWN	string	first	.	.	.
PIXSCAL	N	-9999.	float	first	.	.	.
PLANID	N	UNKNOWN	string	first	.	.	.
PLATSCAL	Y	-9999	float	first	.	.	.
PROCSTAT	Y	UNKNOWN	string	first	.	.	.
PRODTYPE	N	UNKNOWN	string	first	.	.	.
RAMPLN_B	Y	-9999	int	first	0	256	.
RAMPLN_R	Y	-9999	int	first	0	256	.
RAWUNITS	N	ADU/s	string	first	.	.	.
RESFILE	N	UNKNOWN	string	concatenate	.	.	.
RESOLUN	N	-9999.	float	first	.	.	.
RSPNFILE	N	UNKNOWN	string	concatenate	.	.	.
SCANNING	N	F	bool	first	.	.	.
SCNDECO	N	-9999.	float	first	-90.	90.	.
SCNDECF	N	-9999.	float	last	-90.	90.	.
SCNDIR	N	-9999.	float	last	.	.	.
SCNRA0	N	-9999.	float	first	0.	24.	.
SCNRAF	N	-9999.	float	last	0.	24.	.
SCNRATE	N	-9999.	float	last	.	.	.
SIBS_X	N	-9999	int	default	.	.	.
SIBS_Y	N	-9999	int	default	.	.	.
SLIT	N	UNKNOWN	string	first	.	.	.
SPATFILE	N	UNKNOWN	string	concatenate	.	.	.
SPECTEL1	Y	UNKNOWN	string	first	.	.	NONE FIF_BLUE
SPECTEL2	Y	UNKNOWN	string	first	.	.	NONE FIF_RED
SRCTYPE	N	UNKNOWN	string	first	.	.	.
POINT_SOURCE EXTENDED_SOURCE OTHER UNKNOWN							
SUBARRNO	N	-9999	int	first	.	.	.
TELAPSE	N	-9999.	float	sum	0.	.	.
TELCNF	N	UNKNOWN	string	first	.	.	.
TELEL	N	-9999.	float	first	0.	90.	.
TELEQUI	N	UNKNOWN	string	first	.	.	.
TELESCOP	N	UNKNOWN	string	first	.	.	.
TELDEC	N	-9999.	float	first	-90.	90.	.
TELLOS	N	-9999.	float	first	-180	180	.
TELRA	N	-9999.	float	first	0.	24.	.
TELVPA	N	-9999.	float	first	0.	360.	.
TELXEL	N	-9999.	float	first	-90.	90.	.
TEMP_OUT	N	-9999.	float	first	.	.	.
TEMPPRI1	N	-9999.	float	first	-273.	.	.
TEMPPRI2	N	-9999.	float	first	-273.	.	.
TEMPPRI3	N	-9999.	float	first	-273.	.	.
TEMPSEC1	N	-9999.	float	first	.	.	.
TRACERR	N	F	bool	or	.	.	.
TRACKANG	N	-9999.	float	first	.	.	.
TRACMODE	N	UNKNOWN	string	first	.	.	OFF CENTROID ROF LIMB
OFFSET ROF+OFFSET CENTROID+INERTIAL ROF+INERTIAL OFFSET+INERTIAL ROF+OFFSET+INERTIAL							
TSC-STAT	N	UNKNOWN	string	last	.	.	.
UTCEND	N	UNKNOWN	string	last	.	.	.
UTCSTART	N	UNKNOWN	string	first	.	.	.
WAVECENT	N	-9999.	float	first	0.	.	.
WAVEFILE	N	UNKNOWN	string	concatenate	.	.	.
WVSCALE	N	-9999.	float	mean	0.	.	.
WVZ_END	N	-9999.	float	last	0.	.	.
WVZ_STA	N	-9999.	float	first	0.	.	.
XPOSURE	N	-9999.	float	sum	0.	.	.
ZA_END	Y	-9999.	float	last	0.	90.	.
ZA_START	Y	-9999.	float	first	0.	90.	.